DISSERTATION

CHARACTERIZATION OF LASER-PRODUCED PLASMAS AS LIGHT SOURCES FOR EXTREME ULTRAVIOLET LITHOGRAPHY AND BEYOND

Submitted by

Liang Yin

Department of Electrical and Computer Engineering

In partial fulfillment of the requirements

For the Degree of Doctor of Philosophy

Colorado State University

Fort Collins, Colorado

Fall 2019

Doctoral Committee:

Advisor: Jorge J. Rocca

Carmen S. Menoni
Mario C. Marconi
Azer Yalin

Copyright by Liang Yin 2019

All Rights Reserved

ABSTRACT

CHARACTERIZATION OF LASER-PRODUCED PLASMAS AS LIGHT SOURCES FOR EXTREME ULTRAVIOLET LITHOGRAPHY AND BEYOND

Lithography is a critical process in the fabrication of integrated circuits. The continuous increase in computing power for more than half a century has depended in the ability to print smaller and smaller features, which has required the use of light sources operating at increasingly shorter wavelengths. There is keen interest in the development of high-power light sources for extreme ultraviolet (EUV) lithography at λ=13.5 nm and future beyond extreme ultraviolet (BEUV) lithography near λ=6.7 nm. The work conducted in this dissertation has characterized aspects of laser-produced plasmas (LPPs) that serve as light sources for EUV / BEUV lithography.

The laser pulse shape dependence of the conversion efficiency of λ=1.03 µm laser into in-band 13.5 nm EUV emission in a Sn LPP was studied as a function of laser pulse shape and durations. Laser pulses of arbitrary temporal shape with variable energy and pulse widths were generated using a programmable pulse synthesizer based on a diode-pumped chirped pulse amplification Yb: YAG laser. The pulse synthesizer is based on wave front splitting and pulse stacking for the generation of arbitrary shape laser pulses of Joule-level energy.

Pulses ranging from hundreds of ps to several ns were generated with a single laser. The measurements showed the CE favors the use of nearly square pulses of duration longer than 2 ns, in agreement with hydrodynamic/atomic physics simulations. A significant increase in CE was observed when Q-switched pulses were substituted by square pulses of similar duration.

Conditions were observed at which the EUV pulse duration significantly outlasts the laser pulse in the direction normal to the target surface, in contrast at grazing angles the measured EUV pulse duration is shorter and similar to the laser pulse duration. The physics leading to this angular anisotropy is discussed, along with the spectroscopic characterization of EUV emission and at-wavelength images that characterize the source size.

Another aspect of this dissertation includes a comprehensive study of the emission from Gd and Tb LPPs in the λ=6.5 - 6.7 nm region. BEUV emission spectra were measured as a function of laser pulse duration (120 ps - 4 ns), emission angle, and spatial location within the plasma. At-wavelength images of the BEUV emitting plasma region were obtained as a function of irradiation parameters. The peak of the emission spectrum was observed to broaden and to shift to longer wavelengths as the laser pulses are shortened from ns to hundreds of ps. Transient self-consistent hydrodynamic/atomic physics simulations show that the picosecond irradiation creates significantly hotter plasmas in which the dominant emission originates from more highly ionized species. Gd LPP emission driven by nanosecond laser pulses best matched the reflectivity band of our La/B_4C mirrors. Spatially resolved spectra of the Gd LPP were acquired for different laser parameters and were compared to simulations. The CE into in-band BEUV emission was determined by integrating angularly resolved measurements obtained using an array of calibrated energy monitors. A maximum CE of 0.47% / 0.45% for the Gd / Tb LPPs was obtained within a 0.6% bandwidth. The results are of potential interest BEUV lithography.

TABLE OF CONTENTS

ABSTRACT ii

Chapter 1 Introduction 1

1.1 Overview of photolithography 6

1.2 Overview of EUV lithography 11

1.3 Laser produced plasmas 17

1.4 The absorption of irradiation energy 21

1.5 Hydrodynamic expansion 27

1.6 The EUV radiation from a Sn LPP 33

1.7 Opacity 38

1.8 Materials emitting near λ =13.5nm 50

1.9 The dependence of CE on the laser pulse temporal profile 53

1.10 Lithography beyond EUV 57

References 61

Chapter 2 Pulse Shape Dependence of the EUV Emission from a Sn Laser-Produced-Plasma Using Temporally-Synthesized Irradiation Pulses 76

2.1 Introduction 76

2.2 Experimental setup 78

2.3 Experimental results 83

2.4 Summary 96

References 100

Chapter 3 A Programmable Pulse Synthesizer for the Generation of Joule-Level Picosecond Laser Pulses of Arbitrary Shape 105

3.1 Introduction 105

3.2 Experimental setup 108

3.3 Results and discussion 116

References 120

Chapter 4 Comprehensive Characterization of BEUV Emission from Gd/Tb LPP 124

4.1 Introduction 124

4.2 Experimental Setup 127

4.3 Spectral Characterization ... 130

4.4 Angular Distribution of the BEUV Emission ... 140

4.5 Conversion Efficiency Measurements ... 142

4.6 Plasma Imaging ... 144

4.7 Summary ... 145

References ... 150

Chapter 5 Conclusions ... 155

Chapter 1 Introduction

Electromagnetic radiation has been a potent tool for detection, transmission, heating, and many more applications throughout human history. Among the spectrum of electromagnetic radiation, Extreme Ultraviolet (EUV) radiation is usually identified as extending from photon energies of about 30 eV to about 250 eV, with corresponding to electromagnetic wavelengths ranging from 5 nm to 40 nm compared to soft x-ray region that extends from about 250 eV to several keV, as shown in Figure 1-1 [1]. EUV remained relatively unexplored because the radiation in this spectral region is strongly absorbed by almost any material due to that EUV light can photo-ionize all materials. However, the development of optical components, such as multilayer mirrors [2,3] and diffractive optics [4,5], has facilitated research on EUV radiation. Over the past few decades, the development of sources that emit EUV radiation has also helped to facilitate the exploration of applications. These EUV sources are based on two types of generation methods: synchrotron radiation and plasma radiation. Synchrotron radiation is based on the angular acceleration of charged particles by a magnetic field which can be produced by three types of magnetic structures: bending magnets, undulators, and wigglers. Synchrotron radiation is generally incoherent but can become partially coherent when undulators are used under certain circumstance [1][6]. Plasma radiation can be generated by intense laser field or discharge and can be coherent or incoherent depending on the specific way of plasma generation. For example, capillary discharge soft x-ray laser [7], laser-plasma-based soft x-ray laser [8], high-harmonic generation [9] are coherent sources. Laser-produced-plasma (LPP) [10,11], discharge-produced-plasma (DPP) [12,13], Z-pinch [14] are incoherent. Be noted that here, LPP and DPP specifically

refers to the incoherent sources for lithography. The short wavelength of EUV radiation makes it useful in many applications. Some applications such as diffractive imaging [15], interference lithography [16], atomic and molecular imaging [17], and interferometry [18], and more require coherent EUV sources. Some applications such as EUV lithography, incoherent EUV emission is preferred. The introduction of EUV into lithography comes from the fact that the smallest feature that can be printed on the wafer is proportional to the wavelength of the light source used. For this reason, the semiconductor industry has been investing heavily to develop EUV lithography to make the next generation of integrated circuits.

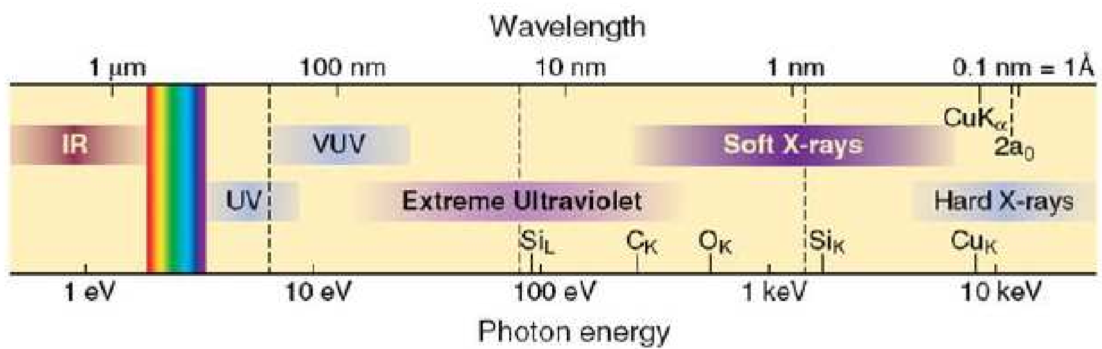

Figure 1-1 The spectrum of electromagnetic wave [1].

At the early stage of the development of EUV lithography, the semiconductor industry suffered from insufficient power of the EUV source. Proof of principle experiments were conducted with low average powers, but high wafer throughput requires high average power because of a narrow spectral bandwidth of 2% near λ=13.5 nm of the EUV radiation, and a low total transmission can be used for wafer exposure due to the combination of the mirrors used in the illumination and imaging system. Laser produced plasmas were identified as the leading way to achieve the required EUV power [19]. Much research was conducted on possible target materials including

xenon, lithium, and tin for the generation of LPP. Li LPP has intense and narrowband emission near λ=13.5 nm, but the CE of Li LPP is as low as 1.2% [20]. Moreover, lithium is a metal which is difficult to handle. Xenon was an attractive option for that xenon is a noble gas and mitigates the challenge of debris mitigation. However, Xe LPP also suffers from a low CE of Xe LPP (<1%) [21,22][23] near 13.5 nm. Theoretically estimated CE of Sn LPP as high as 7% have been reported[24], which makes tin the leading material for EUV sources for large volume manufacturing along with other factors such as manageable debris and feasible fuel delivery.

In the last decade, the output power of the EUV source has been increased by more than 20 times after tremendous effort being put in the improvement of the EUV source, as shown in Figure 1-2. The Sn LPP as a EUV source started with EUV power ~10 W and conversion efficiency less than 1%. In order to obtain higher EUV power, the architecture of the driving laser has evolved from NOMO (No Master Oscillator) to MOPA (Master Oscillator Power amplifier) with pre-pulse. The transition from NOMO to MOPA increased the laser power significantly, and the introduction of pre-pulse resulted in a great improvement of conversion efficiency (CE) of the Sn LPP. The pre-pulse modifies the initial droplet into a larger target, resulting in increased surface area and more favorable density. Even higher CE of 3.5% and EUV power of 100 W was achieved by suppressing the pedestal energy of the main pulse. These concepts were extended by the introduction of a higher power seed-system (HPSS) that enabled further optimization of the main-pulse temporal profile, explicitly allowing for a significant increase in the peak power of the main-pulse laser and further reduction of laser pedestal energy. The technology has been shown to produce mean CE above 5% and EUV power at ~200 W [25]. Modeling has been conducted to provide a better understanding and guide the experiments for improved CE [26–29]. Finally, 250 W EUV power

and CE higher than 6% on a product system was reached, a token power level the industry had set as a requirement for EUV readiness [30], as shown in the bottom plots in Figure 1-2.

However, additional increases in average power are still desired to increase wafer throughput. Further increases in the EUV power, besides employing more powerful driver lasers, depend on the optimization of the conversion efficiency (CE) of laser energy into EUV radiation. This thesis is focused on the characterization of the EUV sources and the improvement of the CE.

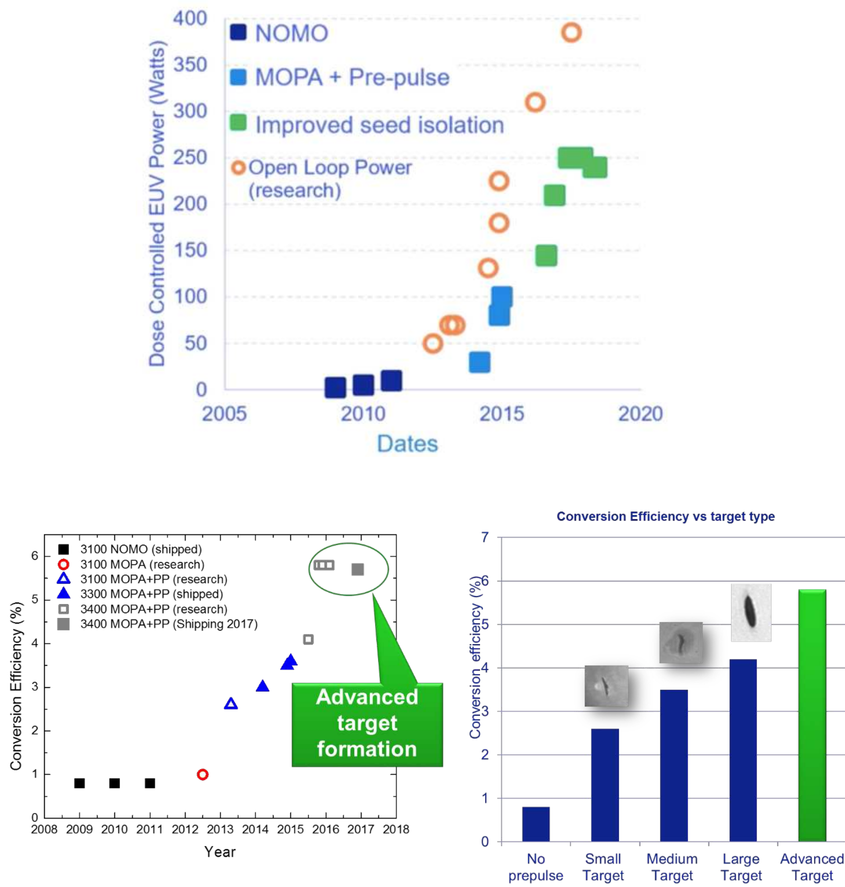

Figure 1-2 EUV power (top) and conversion efficiency (bottom) scaling history at ASML [31].

In Chapter 1, the photolithography and EUV lithography are first reviewed in terms of principles and critical components. Following that, the laser-produced plasma (LPP) is reviewed

comprehensively. An LPP is created focusing a laser beam on target. The intensity in the focal spot produces rapid local heating and intense evaporation followed by plasma formation. Free electrons are generated via multi-photon ionization at the very beginning. The ionization and excitation of atoms are taken over by electron-collision impact when enough number of fast electrons are generated. The fast electrons gain their kinetic energy from photons by inverse Bremsstrahlung when the laser propagates in the LPP. However, the laser can only propagate in the LPP when the frequency of the laser is larger than the plasma frequency. The plasma frequency $\omega_p = \left(\frac{e^2 n_e}{\epsilon_0 m}\right)^{1/2}$ is a natural frequency at which the electrons tend to oscillate and depends on the electron density. The plasma expands into the vacuum with a thermal expansion velocity, resulting in an exponential decay of electron density from the target surface. Consequently, as the laser propagates in the plasma towards the target surface, it experiences increasing electron density and increasing plasma frequency until the plasma frequency equal to the laser frequency. The electron density at which the plasma frequency equal to the laser frequency is known as critical density. Most of the laser energy is deposited in a region with electron density slightly below the critical density, generating a hot and dense region of the plasma. In the plasma, numerous n=4-4 resonance transitions exist in the EUV spectral region and such transitions are generally poorly resolved due to physical broadening phenomena (Doppler broadening, collisional broadening, etc.) and limited instrumental resolution, forming an intense Unresolved Transition Array (UTA). However, there are also many ground-state ions in the plasma which absorbs the EUV emission, and this absorption is known as opacity. Luckily, the broadening of resonance lines gives the EUV photons better chance to escape the plasma. Among the three broadening mechanisms, Doppler broadening is anisotropic because the ions

which travel in the angles close to the laser axis have higher kinetic energy thus more significant Doppler shift. The Doppler broadening, combined with the two-dimensional expansion effect as well as the secondary plasma formed in the periphery of laser focus, causes an anisotropic angular profile of EUV emission. Opacity is one of the significant obstacles to obtaining high conversion efficiency. Methods to reduce the opacity include using a laser with a long wavelength, low initial density target, dual pulse irradiation scheme, and more. Moreover, the choice of material of the target for the EUV source plays an essential role in order to have optimal CE. Lithium, xenon, and tin have been investigated, and tin won due to that Sn LPP has the highest CE along with manageable debris and feasible fuel delivery. When EUV lithography based on Sn LPP has started to be used in high volume manufacturing (HVM) of integrated circuits (ICs), keen interest has risen in beyond EUV lithography for that it uses intense emission near $\lambda = 6.7$ nm and consequently can shrink the feature size of ICs further.

1.1 Overview of photolithography

Since 1959 when Jack Kilby invented the first integrated circuit [32], the semiconductor has been dominating the electronic world. Over the past few decades, the semiconductor functional unit has progressively shrunk in order to increase the density of semiconductor functional units on the wafer. This poses challenges on the semiconductor industry's capability of fabricating smaller features for integrated circuits. The method of fabricating integrated circuit is called lithography. Lithography is a technique which transfers the pre-designed pattern to a surface. In modern times, besides photolithography which prevails in semiconductor manufacturing, there are

several competing technologies of lithography: electron beam lithography, nanoimprint lithography, scanning probe lithography.

Electron beam lithography (EBL) uses accelerated electron beams to interact with resist. The solubility of resist area exposed to the electron beam is changed and will be removed or stay in the subsequent 'developing' stage. There are two types of EBL: direct writing [33] and project printing [34,35].EBL can achieve very high resolution. For instance, around 2 nm feature size and 5 nm half-pitch were demonstrated in reference [36]. However, a critical drawback of EBL is that writing speed, aka throughput, is too low although tremendous effort [37–40] aiming to improve the writing speed has been made in electron beam project printing. Another candidate is nanoimprint lithography (NIL) in which a mold is directly pressed into resist to form a pattern. The resolution of NIL has been demonstrated down to 2.4 nm [41], and it offers high throughput. However, the direct contact between mold and resist makes overlay alignment, template fabrication, defect control, difficult challenges for commercialization [42]. Scanning probe lithography (SPL) evolves from Atomic Force Microscopy (AFM). It produces a pattern by using a probe with a sharp tip to locally modify the surface of a sample[43–45]. The key benefit of SPL is that SPL can produce patterns with a resolution of sub-10-nm [46], which makes SPL very attractive. However, because SPL is a serial process, slow writing speed ~ 10^4-10^5 $\mu m^2 h^{-1}$ is its main drawback. Photolithography uses a formerly visible and now Extreme Ultraviolet light beam to project a pattern from a photomask, through a reducing imaging system, onto a wafer. The wafer is coated with a layer of photoresist, and the photoresist area that is exposed to light will be removed or stay later depending on the type of the photoresist.

In the semiconductor industry, photolithography is the only proven method for high volume manufacturing of IC chips so far because photolithography has a high resolution as well as high speed of printing. The history of photolithography is a continuous effort to improve the resolution of lithography systems (commonly known as scanners). This can be achieved using optical and processing tricks to increase the numerical aperture of the projection lens in the system, or by reducing the wavelength of the light used. Since the 1980s, cutting- edge lithography has shifted from the 365 nm 'i-line' of mercury vapor lamps to deep-ultraviolet light from excimer lasers at 248 nm (krypton fluoride lasers) and 193 nm (argon fluoride lasers). Extreme ultraviolet (EUV) lithography is the next step in this trend [47]. The main components of a Photolithography stepper are the light source, illuminator, photomask, objective lens, and photoresist-coated wafer, as shown in Figure 1-3 [48].

1.1.1 The light source

At the beginning of employment of photolithography, the light at wavelengths of 436nm (g-line), 405nm (h-line) and 365nm (i-line) produced by Hg lamp was used. As time went by, the demand for higher speeds of printing and smaller features motivated the development of shorter wavelength, higher power sources. These requirements were met by the invention of the excimer laser [49]. The KrF excimer laser at λ=248nm and the ArF excimer laser at λ=193nm are the most commonly used excimer lasers in photolithography. With the assistance of immersion techniques to increase the NA and multiple patterning, photolithography using deep ultraviolet emission (DUV lithography), is able to support the 7 nm node [50]. DUV lithography has continued the evolution of semiconductor which is defined by Moore's law. However, it has become more

and more challenging to continue the advancement using DUV lithography. Even though multiple patterning has helped to shrink the feature size, DUV lithography becomes prohibitively expensive because the multiple exposures reduce throughput and also increase complexity due to the alignment requirements.

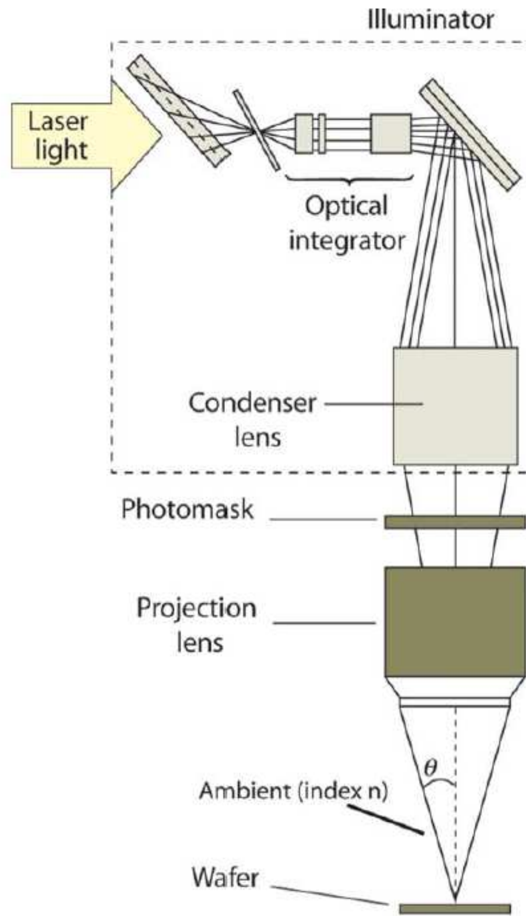

Figure 1-3 Schematic of the optical projection system. The main components are the laser, illuminator, photomask, projection lens, and photoresist-coated wafer [48].

1.1.2 The illuminator

In an exposure tool, the illuminator consists of optical elements in a complex arrangement. The illuminator is used to expand and homogenize the light from the source so that the photomask

is illuminated uniformly, and the objective lens has optimum performance. An illuminator usually consists of a sequence of lenses/mirrors that guide the light from the source. Next, a zoom diffuser expands the beam to either a hexagonal-shaped quartz rod that uses multiple internal reflections to integrate the light or a ‘fly-eye’ array of lenses that projects multiple images to perform the same function. After that, the light is collimated and projected onto the mask by the condenser lens.

1.1.3 The photomask

The photomask contains the pattern to be transferred to the wafer surface. In DUV lithography, the mask consists of a quartz substrate on top of which a chromium absorber layer defines the pattern. Quartz becomes the material of choice because glass is too opaque at the Deep-Ultraviolet wavelengths. The mask is placed in the optical path after the illuminator so that the pattern is captured by the beam.

1.1.4 The objective lens

The objective lens is the most critical and complex optical assembly in an exposure tool. The pattern on the mask is projected by the objective lens to the wafer with a specific reduction factor. Before EUV lithography, most lenses are refractive in the objective lens, which consists of several dozens of optical elements that are aligned to each other within microns. For DUV systems, most of the optical elements are made of fused silica, while newer systems also use CaF_2. The parameter most often discussed is the size of the entrance pupil in the objective lens, or the numerical aperture (NA) because the NA determines the resolution of the objective lens

with wavelength and other factors. The NA is defined as $NA = nsin(\theta)$, where n is refractive index and θ is the maximum half-angle of the illumination cone that can enter the entrance pupil.

1.1.5 The photoresist

Photoresists are light-sensitive polymeric resins formulated for use in photolithography where they serve as masking materials for the transferal of images into an underlying substrate via etching processes. A patterned mask is projected by the objective lens to the surface. A developer is then applied to the photoresist to remove the material that is exposed to the light in the case of a positive photoresist or remove the material that is not exposed to the light in the case of a negative photoresist.

1.2 Overview of EUV lithography

As Moore's law predicts, the number of transistors in a unit area increases with time, which requires a smaller feature size of the printed pattern. The critical dimension (CD) of a printed pattern is determined by the formula CD= $\kappa\frac{\lambda}{\mathrm{NA}}$, in which λ is the wavelength of the light source, NA is the numerical aperture of the projection system, and κ is known as the resolution factor and accounts for all other process variables. The formula above straightforwardly points out three ways to meet the requirement of printing patterns with smaller feature size: using a light source with a shorter wavelength, increasing the numerical aperture of the projection system and decrease the κ factor. Lots of effort has been made to increase NA and decrease κ such as

immersion lithography and double patterning. In this thesis, we focus on shrinking the wavelength of the light source.

While the DUV lithography is reaching its limit, it is pressing to investigate technologies for next-generation lithography, which enables the continuous shrinking of feature size at a reasonable cost of ownership. Decades ago, EUV lithography emerged as a promising candidate for next-generation lithography. EUV lithography obtains its name from the fact that the wavelength (λ=13.5 nm) near which the light source radiates falls in the Extreme Ultraviolet spectrum region. It is a large decrease in wavelength from λ=193nm to λ=13.5nm. Illustrated in Figure 1-4 is a schematic of a EUV lithography scanner. EUV lithography is also a type of photolithography but departs from the conventional photolithography in several ways. All matter absorbs EUV radiation, which results in two major consequences for EUV lithography scanner manufacturers. Firstly, the entire optical path from the light source to the wafer must be in near-vacuum. Secondly, all the optical elements used must be reflective instead of refractive. Mirrors for this wavelength consist of surface coatings of up to 100 alternating layers of silicon and molybdenum, which reflect light through interlayer interference as discussed in the following section.

1.2.1 Mo/Si multi-layer mirror

One of the reasons why the wavelength λ=13.5 nm is chosen is because that near this wavelength, high-reflectivity Mo/Si multilayer mirror is available. Mo/Si multilayer mirror can reach a theoretical maximum reflectivity of 72.3%, as shown in Figure 1-5. The broad reflectivity band near 13.5 nm (~5.2% FWHM) makes it less difficult to match wavelength among mirrors. In order to make the multilayer coating to function efficiently, it required stable interfaces and

sufficient contrast in the refractive index between the material layers. The highest reflectivity, 70% at 13.5 nm, was achieved using interface-engineered multilayer coating, such as the Mo/B_4C/Si/B_4C made by magnetron sputtering [51], shown in Figure 1-6 (b). These new coatings consist of alternating Mo and Si layers divided by thin boron carbide layers. The molybdenum silicide formation on the Mo-Si interfaces is reduced by depositing boron carbide between the layers, leading to a reduction of bilayer contraction by 30%. Consequently, the Mo-Si interfaces are sharper compared to standard Mo-Si multilayers, as shown in Figure 1-6 (a).

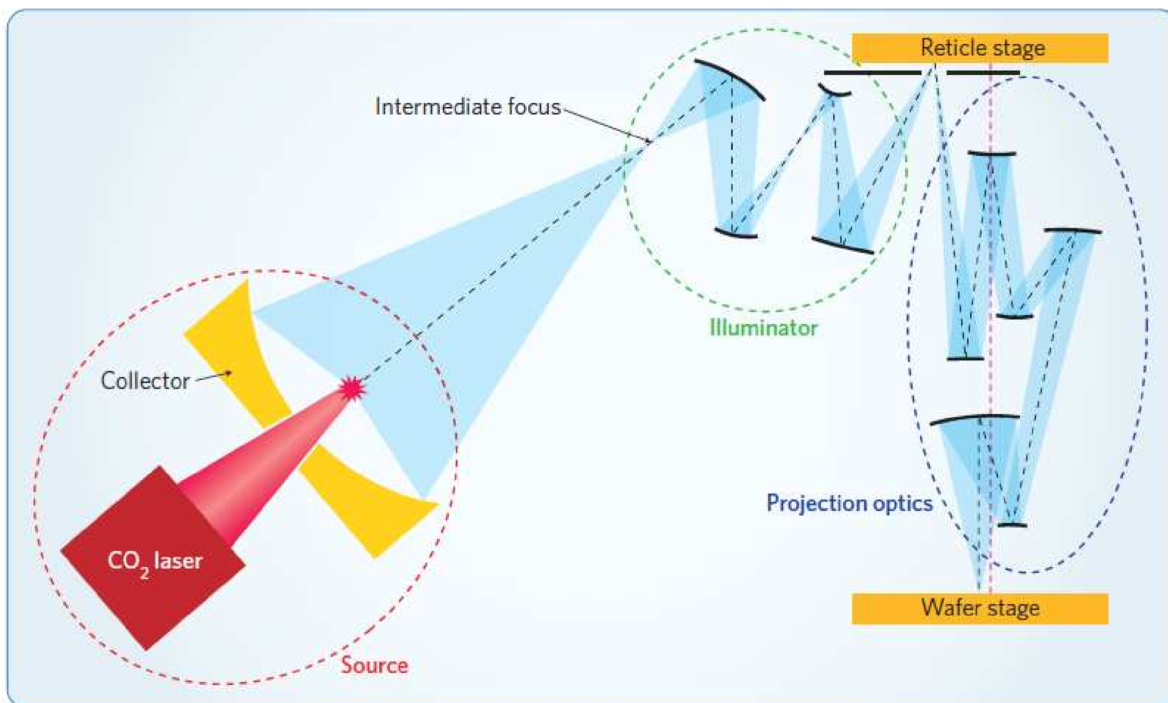

Figure 1-4 Because all matter absorbs EUV radiation, the optics for collecting the light (collector), conditioning the beam (illuminator) and pattern transfer (projection optics) must use high-performance molybdenum–silicon multilayer mirrors, and the entire optical path must be housed in a near-vacuum environment [47].

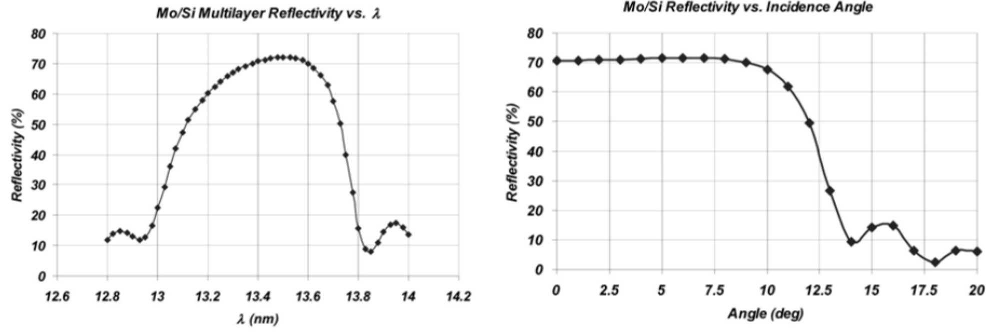

Figure 1-5 Normal-incidence reflectivity vs. wavelength and reflectivity vs. angle for an ideal Mo/Si ML with 40 bilayer pairs. The period of a single bilayer is 7.0 nm and the thickness of individual Mo and Si layers is 2.76 nm and 4.14 nm, respectively [52].

1.2.2 The photomask for EUV lithography

In Figure 1-4, on the reticle stage, a photomask is placed. Since EUV light is strongly absorbed by all materials, all the optical components are reflective instead of refractive, including the mask. Consequently, the EUV mask structure is drastically different from that of conventional optical lithography. When a EUV beam is reflected by the photomask, the pattern that the photomask carries will be projected onto the wafer. In order to produce optical contrast for imaging, the patterns with high EUV absorbance is coated on the top of the Mo / Si multilayer mirror. Defects in the multilayer mirror or the patterned absorber can introduce distortion of the aerial image. Besides the mask defect, a shadowing effect imposes unique restrictions for the EUV mask structure due to that oblique incident angles are inherent when the EUV beam is reflected by the mask [53]. Although the reflectivity of Mo/Si mirror almost reaches the theoretically optimal value, a typical projection system of a EUV lithography machine is consisted of six or more mirrors [47], ending up a low total transmission of the projection system and a narrower transmission spectral band. Hence the light source of a EUV lithography system is expected to have very high

power to compensate for the low transmission of the projection system. Next, a brief discussion will be made about the EUV source candidates for lithography.

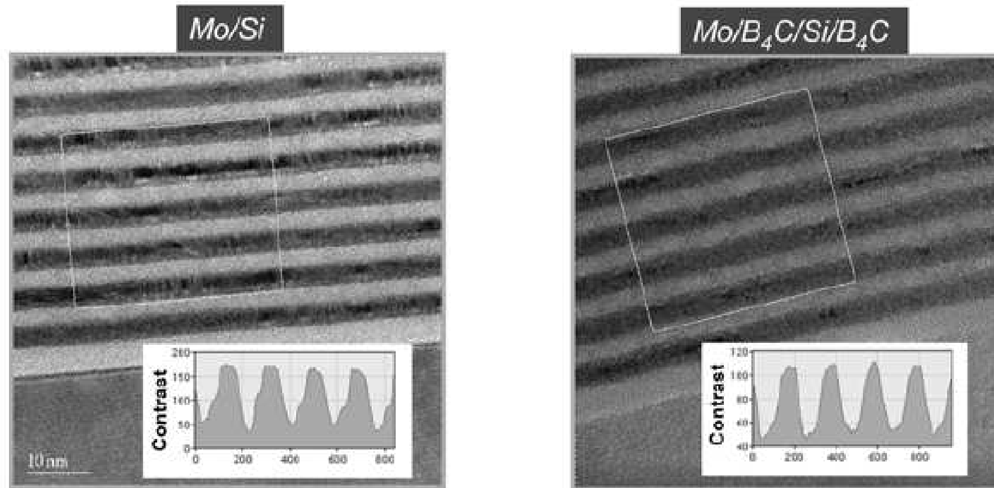

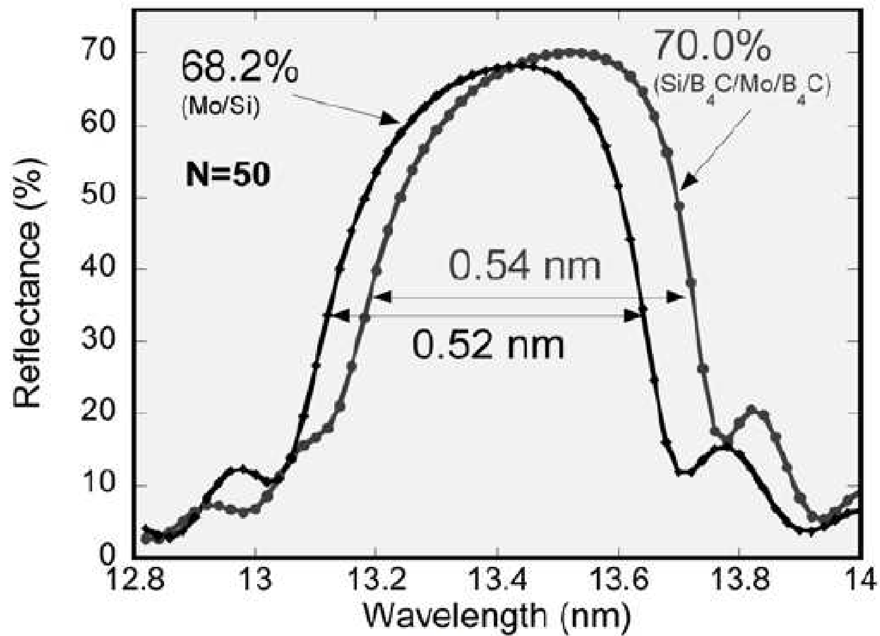

Figure 1-6 (a) Cross-sectional transmission electron microscopy (TEM) images of a Mo-Si ML (top left) and a $Mo/B_4C/Si/B_4C$ ML with improved interface contrast due to the B_4C barrier layers (top right). (b) EUV reflectance curves of the two MLs shown in the TEM images, illustrating the improvement in reflectance due to the B_4C barrier layers [52].

1.2.3 EUV source candidates

Based on the HVM requirements of 100 wafers per hour (WPH) throughput and other system requirements for optics, resist sensitivity, and overhead, a power requirement of 115 to 180 W at the intermediate focus and etendue of $\leq 3\ mm^2sr^2$ has been specified for HVM EUVL [54]. If a collection efficiency of 30% is assumed, the EUV power is required to be higher than 600 W in a solid angle of 2πsr. The candidates of EUV source have been considered for lithography are synchrotron and plasma-based sources. Due to power limitations, high cost and use of one source for multiple lithography machines, the development of synchrotron as EUV source for lithography has been discontinued. So far, all feasible candidates of EUV source for lithography are plasma-based. However, the way of generating such plasma went through a long time of investigation and debate. In the beginning, discharge-produce-plasma (DPP) was a candidate but reached fundamental limits such as power scalability, electrode lifetime, and thermal management very soon [19] even after being upgraded to laser-assisted discharge plasma (LDP). On the other hand, the availability of high-average power pulsed lasers enabled LPP to move forward. LPP is widely used in a variety of applications, including light sources for EUVL, microscopy, micromachining, pulsed laser deposition, nanoparticles and cluster production, laser propulsion, simulation of astrophysical objects, laser-induced breakdown spectroscopy and laser-ablation inductively coupled plasma mass spectrometry, etc. A fundamental understanding of LPP is absolutely necessary for optimizing it for many applications.

EUV lithography based on tin laser-produced plasmas (LPP) emitting at wavelengths near 13.5 nm has recently started to be used in high volume manufacturing (HVM) of integrated circuits

after decades of development[55–59]. However, the optimization of conversion efficiency (CE) is still a pressing task for semiconductor industry because EUV scanner is costly and the cost of ownership of EUV scanner can be reduced significantly with higher conversion efficiency. The conversion efficiency is defined as the energy yield of EUV emission in 2% bandwidth centered at 13.5nm within 2π sr solid angle over the pulse energy of the driving laser. Optimization of the conversion efficiency (CE) of LPP for EUVL is the focus of this thesis, and the optimization involves target material, target geometry, and irradiation parameter.

1.3 Laser produced plasmas

1.3.1 The generation of laser produced plasmas

The high intensity of laser produces rapid local heating and intense evaporation followed by plasma formation when a high-power laser pulse is focused onto a target. The laser-matter interaction is a complicated process which heavily depends on characteristics of the laser as well as the material. A variety of factors, including the laser intensity, the laser pulse width, the spatial and temporal profile of laser pulse and more, affect the laser-induced ablation of material. The properties of the target, for example, geometry and chemical composition, also play critical roles in the laser-induced ablation. During the plasma ablation process, the mechanisms and plasma properties strongly depend on the laser irradiance and pulse duration. For a nanosecond laser pulse with intensities less than 10^8 W/cm^2, the dominant mechanism is thermal vaporization: the temperature of the solid surface increases, leading to a well-defined phase transition from solid to plasma. For a picosecond laser pulse with irradiance between 10^{10}–10^{13} W/cm^2, both thermal

and non-thermal mechanisms such as Coulomb explosion exist [60]. For irradiances higher than 10^{13} W/cm^{2} with femtosecond laser pulse, Coulomb explosion is the main bond breaking mechanism [61].

As shown in Figure 1-7 a) - c) is the process of plasma formation. a) High power lasers when focused onto matter lead to extremely rapid ionization by direct photon-ionization or by multiphoton processes, depending on the wavelength and the type of material. When a sufficient number of free electrons is created, and the free electrons are heated up via inverse bremsstrahlung, the formation of plasma is more efficiently continued by electron - impact ionization. b) when the material is hot enough, it melts and evaporates. The plasma expansion starts, and at this stage, it mainly expands to the normal direction of the target surface. c) after time $t > r_f/u$, the plasma starts expanding spherically.

During the expansion, the transition of bound electrons from the lower level to the upper level and vice versa is driven by inelastic collisions of electrons with ions, while the electron-impact ionization and the three-body recombination determine the concentration of charged particles. Radiative processes, such as spontaneous emission, stimulated emission, and reabsorption, are essential in determining the concentration of excited ions as well. The generation of a high density and hot plasma with low density gradient is desired in a variety of applications. Unfortunately, high-power lasers usually operate in the near-infrared domain at present. As a result, direct interaction of the laser beam with matter only occurs below a specific density which is known as critical density which is typically hundreds of times lower than solid density and quadratically depends on the wavelength of irradiation laser at non-relativistic intensities. Direct

interaction with higher densities occurs only when the oscillatory velocity of the electrons becomes relativistic at laser intensities above 10^{18} W/cm^2. The absorption of laser energy mainly happens in the pink region in Figure 1-7 c), which has a density slightly below the critical density.

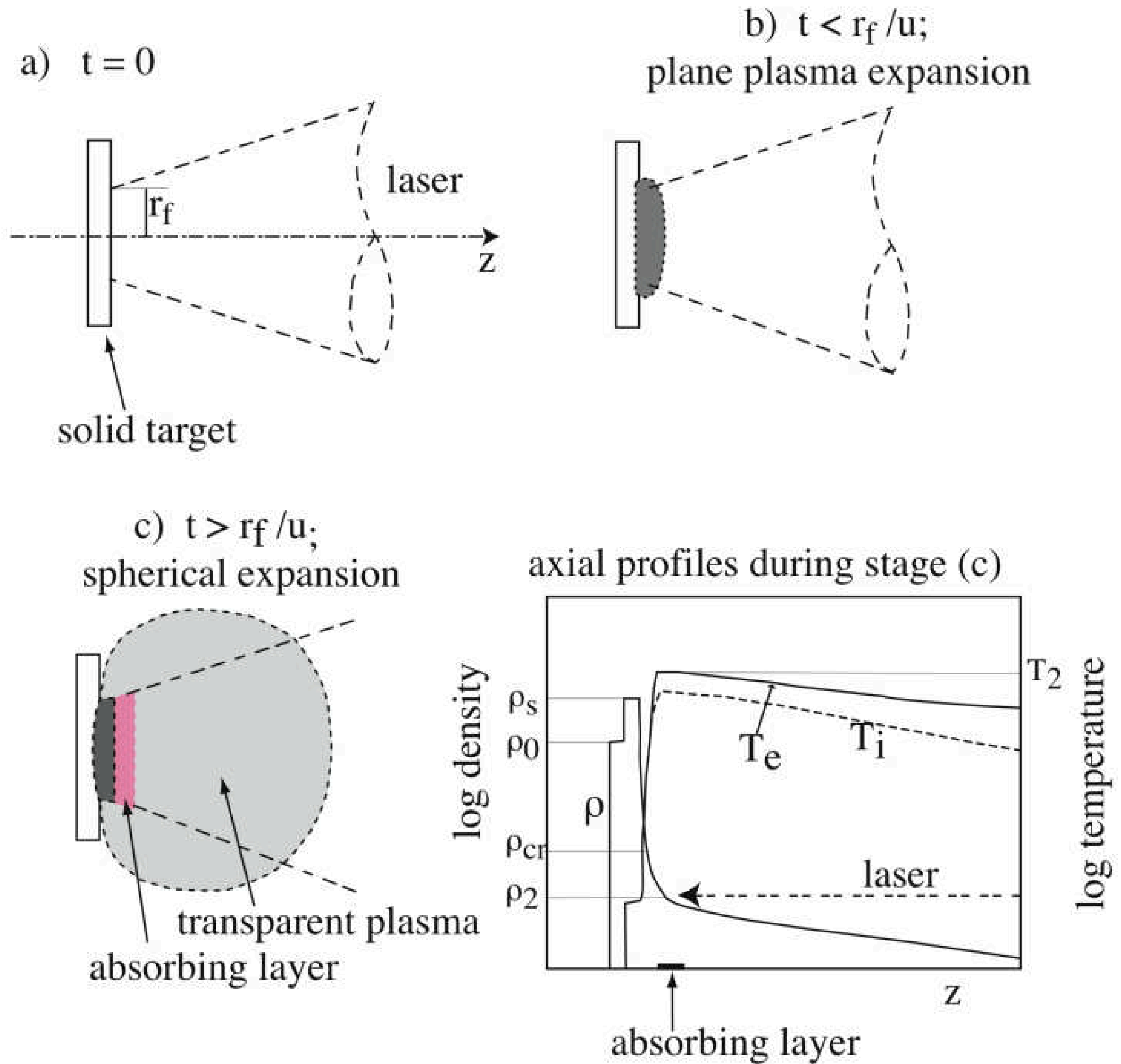

Figure 1-7 Irradiation of a solid target by a moderate intensity, nanosecond laser pulse. a)-c) axial cross-section at different times. d) axial profiles of density and temperature (in logarithmic scale) during the quasi-stationary ablation stage [60]. r_f is the radius of the laser focus and u is the speed of plasma expansion.

1.3.2 Plasma temperature and density

Typically, a laser-produced plasma is characterized by two basic parameters: density and temperature. Most of the other properties of a plasma, including EUV emission, laser energy absorption, opacity, and expansion dynamics, are closely influenced by these two parameters. The peak photon energy of the emission from a plasma is related to the plasma temperature, and EUV emission requires the plasma to be extremely hot, for example, ~10 - 100 eV for EUV generation. Additionally, for the EUV emission to be bright, it must come from a dense plasma. Figure 1-7 includes a diagram which demonstrates the typical profiles of electron temperature, ion temperature, and electron density. The electron and ion temperatures characterize the velocity distribution of the electrons and ions in the plasma. In one direction, the average kinetic energy of particles (electron or ion) $E_{ave} = \frac{1}{2}kT$, where $k = 1.38 \times 10^{-23} J/K$ is Boltzmann constant and T is the temperature. Since the temperature is so closely related to kinetic energy, in plasma physics, it is common to give the temperature of the unit of energy: eV. Here, 1eV = 11600 K. Temperature is an equilibrium concept and to reach equilibrium particles need to be allowed to undergo a sufficient number of collisions in which they will interchange energies. In a plasma, the electrons and ions can have different temperatures because of the two following reasons. First, the interchange of energy in collisions between particles of equal mass is large (for example, collisions between electrons and electrons, ions and ions). Second, the rate of collision between electrons is much higher than that between ions. Therefore, electrons tend to be in 'thermal equilibrium' with other electrons and ions with other ions, but often they are not in equilibrium with each other. Because of plasma expansion, the electron density decreases

exponentially from the target surface. The profile of electron density and expansion velocity will be derived later. To have an ideal CE, a Sn LPP for lithography would be a gaseous sphere which has a plasma density of ~10^{18} cm^{-3}, low-density gradient and a plasma temperature of multiple 10 eV. The reasons will be shown below.

1.4 The absorption of irradiation energy

1.4.1 Propagation of radiation in a plasma

The irradiation laser propagates in a plasma in the form of transverse electromagnetic waves with a cutoff which occurs at the plasma frequency $\omega \cong \omega_p$, which has critical consequences for energy deposit in laser-produced plasmas. The Maxwell-Euler fluid equations, which can be found on page 207 of ref. [1], give a satisfactory description for these waves. It is assumed that the ions are immobile at high frequencies. As a result, we only need to consider the electrons in the Maxwell-Euler fluid equations. For transverse electromagnetic waves of relatively weak intensity, these equations simplify considerably. The current term, which is generally non-linear, simplifies in this case to $\mathbf{J} = -\mathrm{e}n_0\boldsymbol{v}$, where the n_0 is the background electron density, assumed in this weak field limit to be unmodulated by the passing electromagnetic wave. In this case, Maxwell's equation (Equation 6.44-6.49 in Ref. [1]) can be written as

$$\nabla \times \mathbf{H} = \epsilon_0 \frac{\partial \boldsymbol{E}}{\partial t} - en_0\boldsymbol{v} \tag{1.1}$$

$$\nabla \times \mathbf{E} = -\mu_0 \frac{\partial \boldsymbol{H}}{\partial t} \tag{1.2}$$

In Equations 6.50 and 6.51 in Ref. [1], which are respectively the continuity equation and conservation of momentum equation describing particle motion, all non-linear terms can be neglected in the weak field limit. Consequently, these become

$$\frac{\partial n_e}{\partial t} + n_0 \nabla \cdot \boldsymbol{v} = 0 \tag{1.3}$$

$$\mathrm{m}\frac{\partial v}{\partial t} = \frac{\gamma \kappa T_e}{n_0} \nabla n_0 - e\boldsymbol{E} \tag{1.4}$$

because ions are immobile. For transverse electromagnetic waves, the $\nabla \rightarrow i\mathbf{k}$ terms are longitudinal and thus do not contribute to the transverse motion. The remaining terms in Equation (1.4) yield a simplified version of Newton's law, **F**=m**a**, for the electrons:

$$\mathrm{m}\frac{\partial v}{\partial t} = -e\boldsymbol{E} \tag{1.5}$$

We can now develop a wave equation by differentiating Equation (1.1) with respect to time,

$$\nabla \times \frac{\mathbf{H}}{\partial t} = \epsilon_{\mathbf{0}} \frac{\partial^{\mathbf{2}} \boldsymbol{E}}{\partial t^2} - e n_0 \frac{\partial \boldsymbol{v}}{\partial t} \tag{1.6}$$

Also taking the curl of Equation 1.2

$$\nabla \times (\nabla \times \mathbf{E}) = -\mu_0 \nabla \times \frac{\partial \boldsymbol{H}}{\partial t} \tag{1.7}$$

We combine Equation 1.6 and Equation 1.7 by eliminating $\nabla \times \frac{\partial \boldsymbol{H}}{\partial t}$, and use the vector relation $\nabla \times (\nabla \times \mathbf{E}) = \nabla(\nabla \cdot \mathbf{E}) - \nabla^2 \mathbf{E}$, to obtain

$$\nabla(\nabla \cdot \mathbf{E}) - \nabla^2 \mathbf{E} = -\mu_0 \in_{\mathbf{0}} \frac{\partial^2 \boldsymbol{E}}{\partial t^2} + \mu_0 e n_0 \frac{\partial \boldsymbol{v}}{\partial t} \tag{1.8}$$

For transverse waves $\nabla \cdot \mathbf{E} = 0$. Furthermore, we can replace $\frac{\partial v}{\partial t}$ with an expression involving $\boldsymbol{E}$ by use of Equation 1.5, so that

$$\frac{\partial^2 \boldsymbol{E}}{\partial t^2} + \frac{e n_0}{\in_{\mathbf{0}}}\left(\frac{e\boldsymbol{E}}{m}\right) - \frac{1}{\mu_0 \in_{\mathbf{0}}} \nabla^2 \mathbf{E} = \mathbf{0} \tag{1.9}$$

Recognizing $c^2 = \frac{1}{\mu_0 \in_{\mathbf{0}}}$ and $\omega_p^2 = \frac{e^2 n_0}{\in_0 m}$, we have wave equation for a transverse wave in a plasma

$$\left(\frac{\partial^2}{\partial t^2} + \omega_p^2 - c^2 \nabla^2\right) \mathbf{E}(\mathbf{r}, \mathrm{t}) = 0 \tag{1.10}$$

For a plane wave of the form $\mathbf{E}(\mathbf{r}, \mathrm{t}) = E_0 e^{-i(\omega t - \boldsymbol{k} \cdot \mathbf{r})}$ Equation 1.10 yields a dispersion relation

$$\omega^2 = \omega_p^2 + k^2 c^2 \tag{1.11}$$

The dispersion relation for waves propagating in plasma differs from that in vacuum by the appearance of the ω_p^2 term. There is a cutoff frequency in the plasma at $\omega = \omega_p$. For $\omega < \omega_p$, the solution for k is imaginary, indicating that the wave cannot propagate in this overdense plasma. The frequency for which $\omega = \omega_p$ is known as the *critical frequency*. And the corresponding electron density is defined as the *critical electron density*, n_c, where

$$n_c = \frac{\in_0 m \omega^2}{e^2} \tag{1.12}$$

Alternatively, in terms of the wavelength

$$n_c = \frac{1.11 \times \frac{10^{21} e}{cm^3}}{\lambda^2 \mu m} \tag{1.13}$$

Thus, for an Nd laser of wavelength 1.06 μm, the critical density is $n_c = 1 \times 10^{21} e/cm^3$. The derivation of the propagation of radiation in a plasma can be found in reference [1].

1.4.2 The processes of absorption

The radiation absorption of plasma is usually caused by one of or a combination of the following physical processes: 1) Bound-bound absorption. An electron at a lower energy level can jump to an upper energy level by absorbing a photon. The energy of the photon needs to be the energy difference between the upper and lower energy level to be absorbed. As a result, bound-bound transitions cause absorption lines at discrete wavelengths. 2) Bound-free absorption. An electron can jump from a bound state to the free state and become a free electron with kinetic energy equal to the difference between the energy of the absorbed photon and the ionization potential of the electron, If the energy of the absorbed photon is higher than the ionization potential of a given atomic energy level. 3) Free-free absorption. This is also known as inverse bremsstrahlung. An electron absorbs a photon and gains more kinetic energy when it passes through the field of an ion. The free-free absorption contributes to the continuum opacity. 4) Multi-photon ionization. Multi-photon ionization is the mechanism of how free electrons are created when the laser starts to interact with the material.

Assuming that the inverse bremsstrahlung process (collisional absorption) dominates the absorption of irradiation energy, the coefficient of absorption of irradiation energy is given as

$$\alpha = (13.49/\lambda_L^2)Z(n_e/n_c)^2\left(\frac{ln\Lambda}{\sqrt{1-n_e/n_c}}\right)T_e^{-\frac{3}{2}} \tag{1.14}$$

Where $ln\Lambda$ and n_c are the Coulomb logarithm and the critical density for the irradiation laser wavelength, and $\alpha, \lambda_L, n_e\ and\ T_e$ are in $cm^{-1}, \mu m, cm^{-3}\ and\ eV$ respectively [61]. If the laser absorption length (1/α) in the EUV emitting region is longer than the density scale length, a portion of irradiation energy will pass through the EUV emitting region instead of being directly absorbed in EUV emitting region. This portion of irradiation energy is absorbed in the high-density region and is not efficiently converted into EUV emission due to the high opacity of the high-density region. Consequently, the density scale length needs to be equal or longer than the laser absorption length so that the irradiation energy can be absorbed in the EUV emitting region. The EUV emitting region is found to locate in the low-density corona with an electron density ranging from 10^{19} to $10^{20}\ cm^{-3}$, as shown in Figure 1-16. For an isothermal expansion plasma, the density profile in the corona region can be described as $n_i = n_{io}e^{-\frac{x}{v_{exp}t}}$, where $v_{exp} = \left(\frac{Z\gamma\kappa T_e}{M_i}\right)^{\frac{1}{2}}$ is the electron-ion thermal velocity, Z, T_e, and M_i are the average charge state, electron temperature, and ion mass, respectively. $\gamma = 1 + \frac{2}{N} = \frac{5}{3}$, where N is degree of freedom. The density scale length of the corona plasma is estimated as $L_s = v_{exp}t_L$, where t_L is the laser pulse duration. Hence in order to increase the plasma density scale length of the corona, a longer pulse duration is preferred.

Moreover, it is found that the density scale length is not only decided by pulse duration but also by focal spot size, which leads to a second method to improve the irradiation energy absorption: changing the focal spot size of the irradiation laser. Practically, for a Sn LPP created on flat target,

small laser focus causes significant lateral expansion, which wastes laser energy and less EUV emission is produced [62]. At the same time, small laser focus also results in a shorter density scale length, thus lower irradiation energy absorption. Contrarily, for larger spot size, more EUV emission can be produced due to high hydrodynamic coupling efficiency/low lateral expansion and the longer plasma scale length increases the absorption of the irradiation energy. An example of the comparison of density scale length for small and larger spot size is illustrated in Figure 1-8. However, almost constant CE values were observed for a wide range of laser focal spot sizes [63]. It may be because that small plasma volume of Sn LPP created using smaller focal spot reduces the reabsorption of the EUV emission.

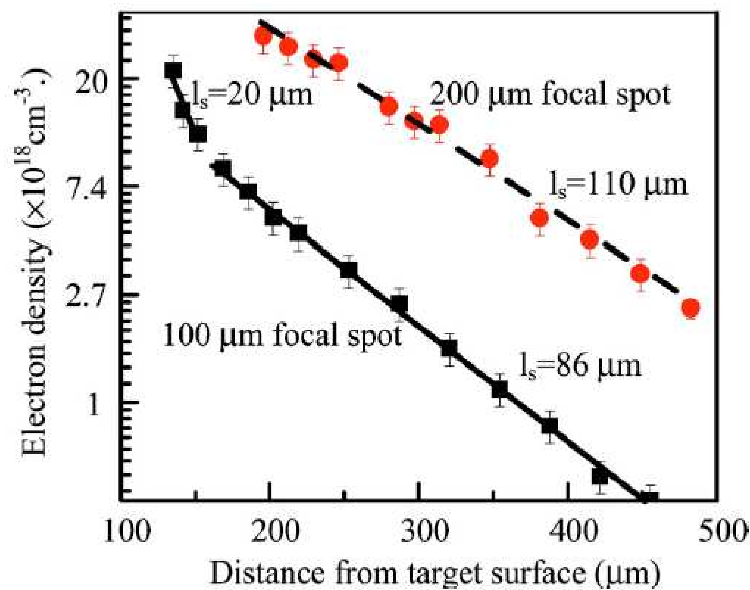

Figure 1-8 Density profiles of laser-produced Sn LPPs with focal spot sizes of 100 μm (circles) and 200 μm (squares) obtained at 2x10^{11} W/cm^2. The two solid curves represent the exponential decay fit of 100 μm spot data with scale lengths of 20 μm and 86 μm, and the dashed line represents the fit of 200 μm spot data with a scale length of 110 μm [63].

1.5 Hydrodynamic expansion

1.5.1 One-dimensional expansion

An important characteristic of laser-produced-plasmas is the fact that they expand into the vacuum with speed determined by the temperature of the electrons and the mass of the ions. The expansion rate of a plasma may be described in terms of the one-dimensional isothermal expansion of a hot fluid with two species: electrons and ions. This can be seen by examination of the conservation of mass and momentum equations:

$$\frac{\partial n_e}{\partial t} + \nabla \cdot (n_e \overline{\boldsymbol{v}}) = 0 \tag{1.15}$$

$$\mathrm{m}\left(\frac{\partial}{\partial t} + \overline{\boldsymbol{v}} \cdot \nabla\right)\overline{\boldsymbol{v}} = \frac{1}{n_e}\nabla P_e - e(\boldsymbol{E} + \overline{\boldsymbol{v}} \times \boldsymbol{B}) \tag{1.16}$$

Assuming a one-dimensional expansion and resultant velocity of expansion is small due to large ion mass, the electron momentum equation is dominated by non-velocity terms, so momentum equation 1.16 becomes

$$n_e e E = -\frac{\partial}{\partial x} P_e \tag{1.17}$$

For ion, the one-dimensional continuity and momentum equations are

$$\frac{\partial n_i}{\partial t} + \frac{\partial}{\partial x}(n_i v) = 0 \tag{1.18}$$

$$\mathrm{M}n_i\left[\frac{\partial}{\partial t}+v\frac{\partial}{\partial x}\right]v=n_iZeE-\frac{\partial}{\partial x}P_i \tag{1.19}$$

The attraction of the electrons to the ions maintains overall neutrality in the plasma, so that

$$n_e=Zn_i \tag{1.20}$$

Moreover, in the momentum equation for ion, the velocity term is kept because the ion mass is large. Using adiabatic condition between pressure and density for process involving no heat transfer:

$$\mathrm{dP}=\frac{\gamma P}{n}dn \tag{1.21}$$

and perfect gas relation:

$$P_j=n_j\kappa T_j \tag{1.22}$$

The pressure gradient terms in the continuity equation becomes:

$$\frac{\partial P_e}{\partial x}=\gamma\kappa T_e\frac{\partial n_e}{\partial x} \tag{1.23}$$

And

$$\frac{\partial P_i}{\partial x}=\gamma\kappa T_i\frac{\partial n_i}{\partial x} \tag{1.24}$$

Where $\gamma=1+\frac{2}{N}=\frac{5}{3}$, where N is the degree of freedom. The momentum equation for ions then becomes

$$\mathrm{M}n_i\left[\frac{\partial}{\partial t}+v\frac{\partial}{\partial x}\right]v=n_iZeE-\gamma\kappa T_i\frac{\partial n_i}{\partial x} \quad (1.25)$$

Substituting for the electric field from the Equation (1.17) and (1.22), which couples electron and ion motion,

$$\mathrm{E}=-\frac{1}{en_e}\frac{\partial P_e}{\partial x}=-\frac{\gamma\kappa T_e}{en_e}\frac{\partial n_e}{\partial x} \quad (1.26)$$

The ion momentum equation (1.25) becomes

$$\mathrm{M}n_i\left[\frac{\partial}{\partial t}+v\frac{\partial}{\partial x}\right]v=-(Z\gamma\kappa T_e+\gamma\kappa T_i)\frac{\partial n_i}{\partial x} \quad (1.27)$$

Or for $T_e \gg T_i$

$$\left[\frac{\partial}{\partial t}+v\frac{\partial}{\partial x}\right]v=-v_{exp}^2\frac{1}{n_i}\frac{\partial n_i}{\partial x} \quad (1.28)$$

Where define an electron-ion thermal expansion velocity

$$v_{exp}=\left(\frac{Z\gamma\kappa T_e}{M}\right)^{\frac{1}{2}} \quad (1.29)$$

The continuity equation for ions can be written as

$$\left[\frac{\partial}{\partial t}+v\frac{\partial}{\partial x}\right]n_i+n_i\frac{\partial v}{\partial x}=0 \quad (1.30)$$

A self-similar solution describing the plasma expansion can be readily found for the fluid Equations 1.28 and 1.30 by letting $n_i=f(x/t)\ and\ v=g(x/t)$, where $f(x/t)\ and\ g(x/t)$ are to be determined. These functions then give

$$f'\left(g-\frac{x}{t}\right)+fg'=0 \tag{1.31}$$

$$g'\left(g-\frac{x}{t}\right)+c_s^2\frac{f'}{f}=0 \tag{1.32}$$

As can be seen by substitution, a solution to the Equations 1.28 and 1.30 is

$$\mathrm{v}=v_{exp}+\frac{x}{t} \tag{1.33}$$

and

$$n_i=n_{io}e^{-\frac{x}{v_{exp}t}} \tag{1.34}$$

Thus, the plasma expands from an initial ion density n_{io}, at a surface x=0, with the electron-ion thermal velocity, v_{exp}. Examining the density function $n_i(x,t)$ we see that the density gradient length l_{exp}, due to the expansion, is given by

$$l_{exp}=\frac{-n_i}{\frac{\partial n_i}{\partial x}}=v_{exp}t \tag{1.35}$$

And increases with time at a rate set by the expansion velocity v_{exp}. The derivation of plasma expanding to the vacuum can be found in reference [1].

1.5.2 Three-dimensional expansion

It has been discussed above that the electron/ion density decays exponentially with distance from a surface x=0 where the initial ion density is n_{io}, assuming a one-dimensional isothermal expansion. However, one-dimension expansion is only an assumption for the convenience of

computation. For an LPP created on a flat solid target, it expands not only to the normal direction of the target surface but also parallel to the target surface, which is known as three-dimensional (3D) expansion. The portion of the LPP that expands parallel to the target surface becomes a peripheral region of cold and dense plasma because this portion of the LPP loses kinetic energy due to adiabatic expansion and thermal conduction to the target surface. Moreover, J. Filevich et al confirms the existence of the peripheral region of cold and dense plasma using a soft-x-ray interferometer which has the capability of probing plasma of density up to $10^{21} cm^{-3}$, as shown in Figure 1-9. It is also found that the ablation of the target surface around the laser focus by the plasma emission substantially contributes to the formation of the peripheral region [64]. The lowly charged ions including neutral atoms in this peripheral portion of plasma have strong absorption of the EUV emission over a wide spectral range causing an anisotropic angular profile of the EUV emission and a decreased CE [65]. In order to eliminate the 2D expansion effects, spherical plastic target coated with a thin tin layer with a thickness of the order of ~1 μm is irradiated uniformly with multiple laser beams. Higher CE was achieved by using the spherical plastic target coated with tin [66][67]. However, spherical plastic target coated with tin is not feasible for industrial application because of the difficulty of feeding target at high speed. In order to feed spherical tin targets at high speed, tin droplets are used as targets. The tin droplet could be water droplet containing tin nano-particles or droplet of melt tin with a diameter of about 30 μm. Usually, the focal spot of the laser is larger than the tin droplet for uniform irradiation on the tin droplet. By getting rid of the lateral expansion and the peripheric region of cold and dense plasma, the EUV emission from a tin droplet target is almost isotropic from 0 degree and 90 degrees from the laser axis. Without the constraint from the flat target, the EUV emission extends

up to 150 degrees from the laser axis, and the amount of EUV energy emitted behind the target (>90 degrees) is about 30% of the total emission, as shown in Figure 1-10 [65].

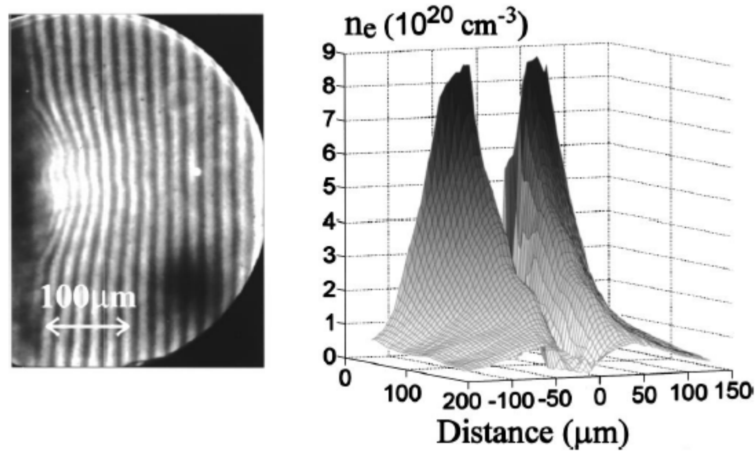

Figure 1-9 Measured soft-x-ray interferogram and corresponding electron density profile for a spot focus plasma. The plasma was generated focusing a 13-ns-FWHM pulse of 0.63 J energy into a 30-µm-diameter spot. The interferometer was acquired at a time near the peak intensity of the heating laser pulse [64].

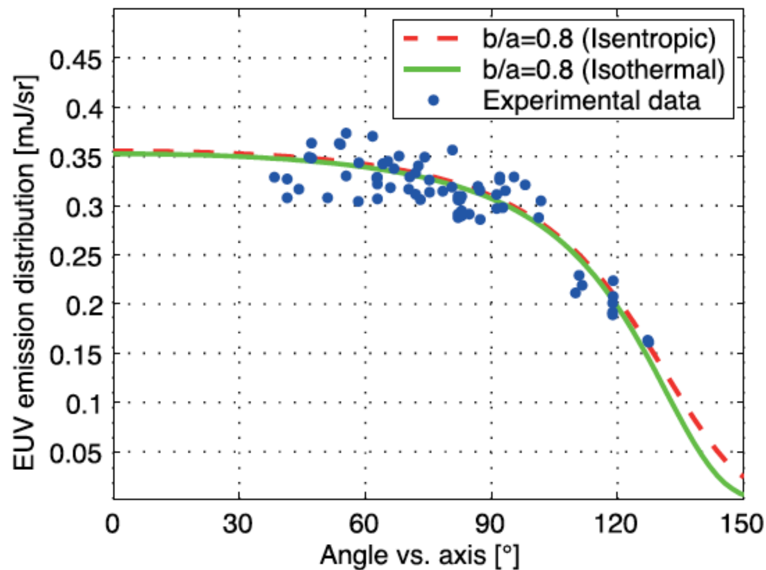

Figure 1-10 EUV emission as a function of the angle from the laser axis. The measurements and the results from the models of the EUV transmission are plotted [65].

1.6 The EUV radiation from a Sn LPP

1.6.1 The processes of plasma radiation

The Sn LPP emits intensely in spectral region λ =13 – 14 nm due to a numerous number of the $4d^m - (4d^{m-1}5p + 4d^{m-1}4f + 4p^5 4d^{m+1})$ transitions in several spectra of the multiply charged tin ions, from Sn^{8+} (m = 6) through Sn^{14+}(m = 1) [28]. Since there are many resonance lines existing in a relatively narrow spectral region, a quasicontinuum of spectral structure is formed, which is known as Unresolved Transition Array (UTA), as shown in Figure 1-11.

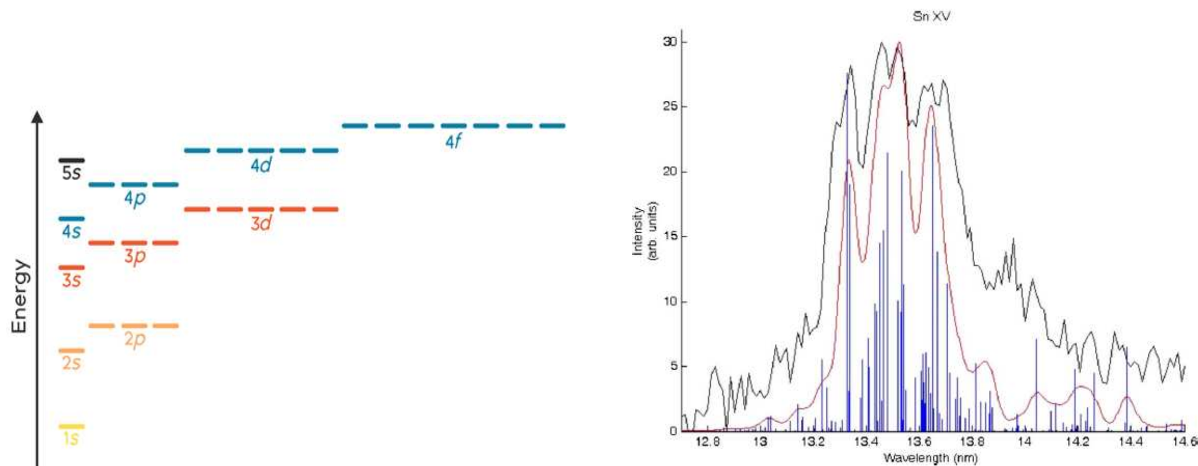

Figure 1-11 (Left) The energy level diagram of an atom [68]. (right) Comparison between a theoretical spectrum for Sn XV convolved with a Gaussian instrumental function and the obtained experimental spectrum of Sn XV. The Theoretical data are also presented in the form of stick plots of height equal to the gf value. [69]

Resonance line (bound-bound emission) is radiated when an electron decays from an excited state to a lower energy level, emitting a photon with energy equal to the potential difference between the two levels. The power density of a certain resonance line can be calculated using the equation below [70]:

$$P_{b-b} = N_{Z,m'}\hbar\omega_{Z,m'\to Z,m}A(Z,m' \to Z,m)\mathcal{L}\left(\hbar\omega_{Z,m'\to Z,m}\right) \quad (1.36)$$

Where Z is the ion charge, m and m' are the lower and upper states respectively, $\hbar\omega_{Z,m'\to Z,m}$ is the energy of the transition and the corresponding photon energy, $N_{Z,m'}$ is the density of ions with the charge and state (Z,m'), $A(Z,m' \to Z,m)$ is the Einstein A coefficient for the decay from state m' to m and $\mathcal{L}\left(\hbar\omega_{Z,m'\to Z,m}\right)$ is the normalized line shape. Line emission can be used to characterize element and the conditions of the plasma from which it is generated.

Besides the resonance line, the emission of Sn LPP can also be generated through another two processes. 1) Bremsstrahlung (free-free emission). The bremsstrahlung process occurs when an electron passes an ion and becomes accelerated, causing the electron to radiate. Because the range of incident electron velocities and the range of distances of the closest approach to the ions are both wide, a broad continuum of radiation is generated in plasma, with a spectrum closely related to the electron velocity distribution, or its characteristic temperature. 2) radiative recombination (free-bound emission). Recombination radiation occurs when a free electron recombines with an ion, emitting a photon and contributing to the continuum emission spectrum. Free-bound emission contains an 'edge' structure corresponding to the binding energies of the various ionization states. However, Bremsstrahlung and radiative recombination in Sn LPP do not contribute much to the EUV region. The three types of emission mentioned above are illustrated in Figure 1-12.

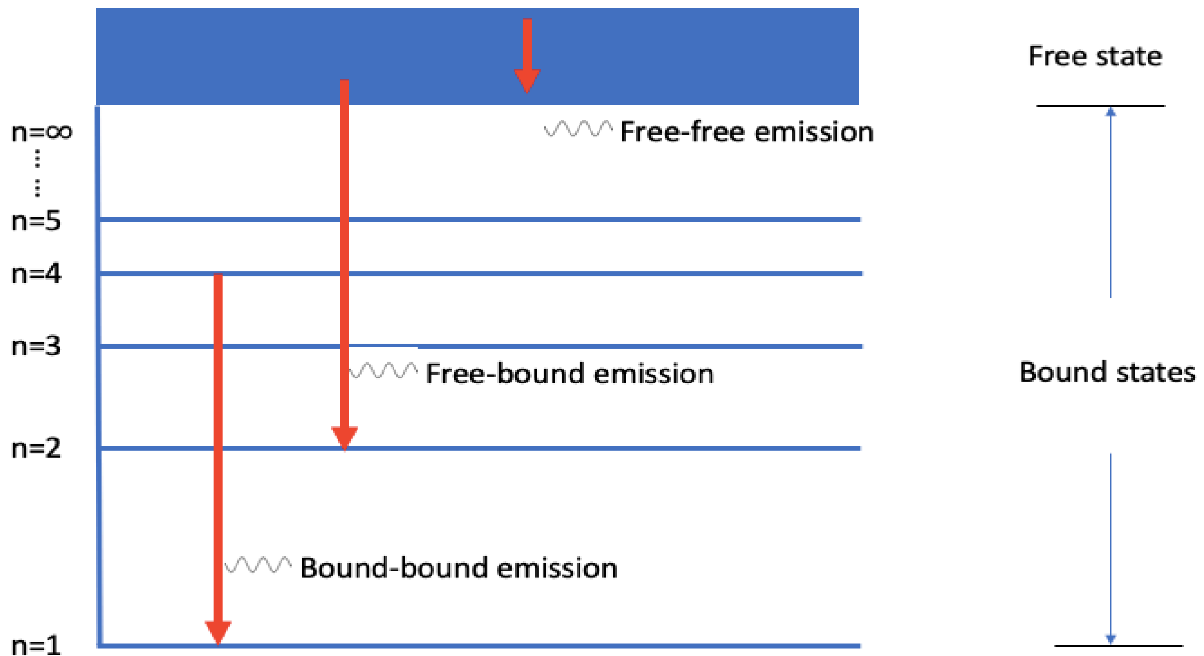

Figure 1-12 Illustration of bound-bound emission, free-bound emission and free-free emission.

1.6.2 The distribution of ionization states

Since the EUV emission near λ=13.5 nm from Sn LPP is emitted in the form of unresolved n=4-4 transition array, the power density of the EUV emission is thus governed by the Equation (1.36). Basically, in order to improve the power density of EUV emission, the density of tin ion species which emits near λ=13.5 nm needs to be increased. This requires a high density of a Sn LPP. Moreover, in a tin plasma, there is an ion state distribution covering ion species from neutral to highly ionized tin ion, and the ionization level distribution is primarily determined by plasma temperature.

The plasma or electron temperature of an LPP is not a parameter which can be directly measured. However, the electron temperature can be inferred by measuring the relative line intensities from successive ionization stages of the same element assuming the LPP is in local thermal equilibrium (LTE) [71][72]. Be noted that an LPP is not always in LTE. A necessary (but not sufficient) criterion for LTE is that the electron density $n_e \geq 1.4 \times 10^{14} T_e^{\frac{1}{2}} (\Delta E_{mn})^3\ cm^{-3}$, where T_e is in eV, ΔE_{mn} is the energy difference between upper and lower energy levels (in eV). For a Sn LPP which has an electron temperature T_e ranging from 1 to 100 eV and an electron density n_e from 10^{17} to 10^{22} cm^{-3}, the ion stage distribution may be determined with collisional-radiative equilibrium (CRE), as shown in Figure 1-13. In order to have abundant tin ion species (Sn^{8+}-Sn^{14+}) which emits intensely in the spectral range of EUV, a plasma temperature of multiple 10 eV is preferred. Additionally, the peak wavelength and the bandwidth of the EUV emission from a tin ion depends on the ionization state of the ion, as Figure 1-14 illustrates. Consequently, the electron temperature of a Sn LPP needs to be carefully dialed in to have the spectral emission of the EUV from the Sn LPP overlap with the spectral band of the projection system in a EUV lithography stepper. Due to the strong dependence of electron temperature on irradiation intensity, the irradiation intensity impacts the spectral behavior of the Sn LPP.

Ideally, a Sn LPP that has an optimal temperature and high density would have intense EUV emission. However, practically as Sn LPP has intense EUV emission near λ=13.5 nm, it also has strong absorption in the same spectral range.

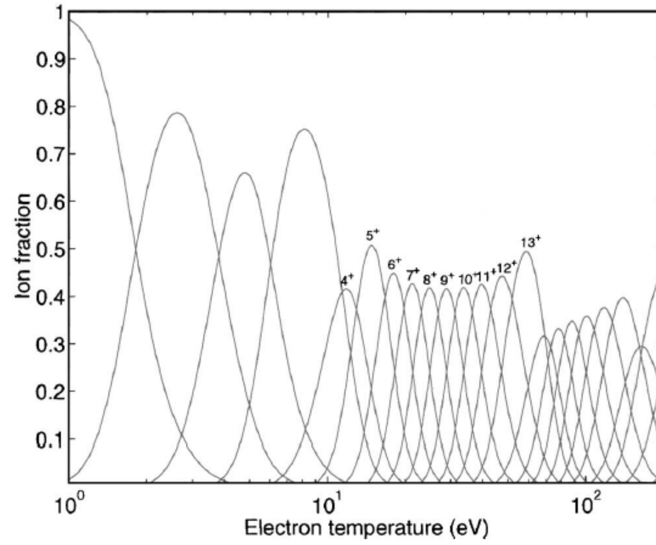

Figure 1-13 Tin ion fraction as a function of electron temperature ($n_e = 10^{21} cm^{-3}$) in a Sn LPP, assuming collisional-radiative equilibrium [27].

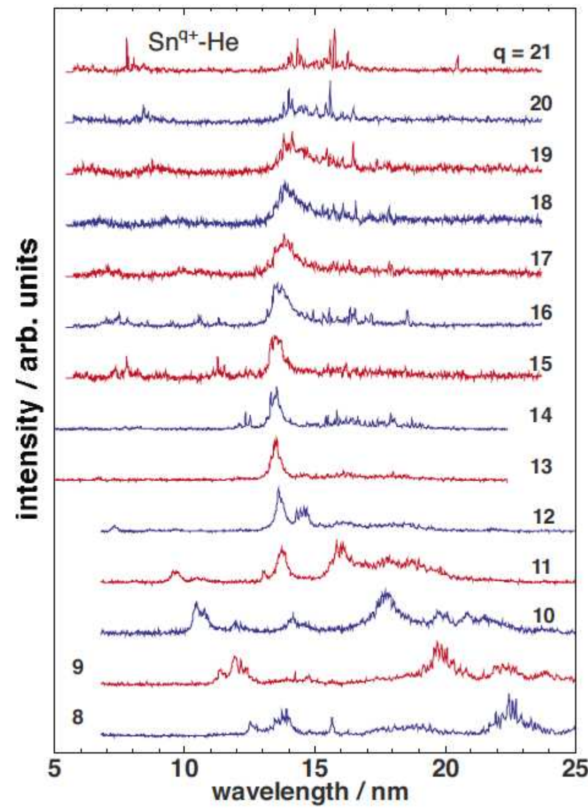

Figure 1-14 Observed emission spectra normalized at peak value of Sn^{q+} (q=8-21) [24].

1.7 Opacity

1.7.1 The definition of opacity

The overall attenuation of EUV emission due to opacity can be described mathematically as below.

When a beam of light of intensity $I(\lambda)$ travels in a plasma, it will be attenuated because the photons can be scattered and absorbed by electrons, ions, and atoms in several different processes, which is described in 1.4.2 (The processes of absorption). This attenuation can be expressed as:

$$dI(\lambda) = -\kappa(\lambda)\rho I(\lambda)ds \tag{1.37}$$

Where $\kappa(\lambda)$ is the absorption coefficient, which is also called opacity (units: cm^2g^{-1}). ρ is the density of the plasma (units: gcm^{-3}), and ds is the travel distance. The photon mean free path can be defined as:

$$\mu = \frac{1}{\kappa(\lambda)\rho} = \frac{1}{\sigma(\lambda)n} \tag{1.38}$$

Where $\sigma(\lambda)$ is the cross-section of the interaction (units: cm^2). and n is the number density of particles (units: cm^{-3}). And the optical depth of plasma is defined as:

$$\tau(\lambda) = \int_0^l \chi(\lambda)ds = \int_0^l \kappa(\lambda)\rho\, ds \tag{1.39}$$

Where $\chi(\lambda) = \kappa(\lambda)\rho$ is the attenuation coefficient. In the case of a photon travelling from the inside of a plasma to the surface, l=0 is at the starting point and at the surface of the plasma, $\tau(\lambda)$ =0. Combining Equation (1.37) with Equation 1.39, we have

$$I(\lambda) = I_0(\lambda)e^{-\tau(\lambda)} \tag{1.40}$$

Where I_0 is the initial intensity of the light without attenuation. A plasma with $\tau(\lambda) \gg 1$ is considered as being optically thick. Otherwise, a plasma is optically thin if $\tau(\lambda) \ll 1$.

1.7.2 Radiation trapping and resonance line broadening

The main process of the absorption of laser energy is inverse bremsstrahlung, while the re-absorption of EUV emission occurs in the forms of both resonance absorption and inverse bremsstrahlung. Here the resonance absorption will be first discussed.

It was mentioned above that Sn LPP radiates EUV in the form of n=4-4 UTA. This emitted radiation is called resonance radiation. Since the resonance photons have energies that correspond to the energies of the transitions, they can easily be re-absorbed by other atoms/ions in the lower levels. An atom/ion is excited to the upper level for some time after absorbing a resonance photon and will eventually emit a photon again. This re-absorption/re-emission process, which can be repeated many times until the photon finally escapes from the plasma, is called 'radiation trapping.' Ideally, the energy of a photon emitted is strictly equal to the energy difference between the upper level and lower level, resulting in a sharp resonance line. So that there is a certain chance of absorption when the photon's energy exactly matches the energy difference between the upper level and the lower level, but no absorption otherwise. However, the

resonance line is broadened to have a certain profile, especially in a dense plasma. This profile is a distribution of probability as a function of resonance frequency. It has a peak frequency corresponding to the 'nominal' energy difference between the energy levels. This means that the probability of absorption is most significant when the photon energy matches the 'nominal' energy difference between the energy levels. And the absorption probability decays when the resonance frequency departs from the peak frequency by a frequency displacement $\Delta\nu$. This distribution of probability of emission/absorption as a function of resonance frequency is called the line shape. The line shape has a significant consequence for the radiation trapping. Due to the spectral line broadening, there is a certain probability for an excited atom/ion to reemit the photon at some slightly different frequency. Consequently, the frequency of a photon may change at each absorption/reemission process. This effect is called 'frequency redistribution'. Due to the dependence of the absorption probability on the frequency, the behavior of the photons with frequencies near the peak frequency is different from the photons with large frequency displacement $\Delta\nu$. Thus, a photon with frequency near the peak frequency has a short mean free path and can only cover a small distance before being absorbed. In contrast, a photon in the wings of the line shape can cover a larger distance and perhaps even escape from the plasma. Since the photons with frequencies near the peak frequency can be absorbed by the plasma more easily than the photons in the wings, radiation trapping also leads to a distortion of the line shape. In the most extreme case, no photons near the peak frequency can escape the plasma and contribute the plasma emission. The plasma emission thus has a 'dip' at the peak frequency[73].

There are several mechanisms that broaden the resonance lines: natural broadening, electron collision broadening, and Doppler broadening. Both natural broadening and electron collisional broadening are lifetime broadening and are considered as homogeneous broadening. They have the same line shape. But they can be considered to be statistically independent. Thus, the linewidth of homogeneous broadening is the sum of those of natural broadening and electron collisional broadening[74].

1) Natural broadening

The natural broadening is caused by the finite lifetime of the atomic levels. The Heisenberg uncertainty principle states that energy and time can be determined simultaneously only with an uncertainty of $\Delta E \cdot \Delta t = \hbar$. In our case, this relation applied to the energy and lifetime of an atomic level. An atomic level has an energy uncertainty due to its natural lifetime, $\Delta t = \tau$. Photons are emitted or absorbed in a range of energies, ΔE. The shorter the lifetime, the larger the broadening. The radiated field from an atom radiating between states j and i can be expressed by:

$$E(t) = \exp\left[\left(-\frac{\gamma}{2} + i\omega_0\right) t\right] \tag{1.41}$$

Where $\gamma = A_j + A_i$ and $\omega_0 = 2\pi \frac{E_j - E_i}{h}$. $A_j = \sum A_{jk}$ is the sum of the spontaneous emission rates out of the excited state, and $A_i = \sum A_{ik}$ is the sum of the spontaneous emission rates out of the ground state. The line profile of natural broadening then can be obtained by

$$L(\omega) = \left| \int_0^\infty E(t) e^{-i\omega t} dt \right|^2 = \frac{2}{\pi \Delta\omega} \frac{1}{1 + \frac{4(\omega - \omega_{ij})^2}{(\Delta\omega)^2}} \tag{1.42}$$

Where $\Delta\omega = A_j + A_i = \sum A_{jk} + \sum A_{ik}$ is linewidth caused by natural broadening. The line profile caused by natural broadening has a Lorentzian line profile.

2) Electron collision broadening

Electron collisional excitation and deexcitation cause spectral broadening in a manner similar to spontaneous emission by limiting the effective lifetimes of atomic states. Moreover, it also has the Lorentzian line profile. Hence the collision linewidth is given by the sum of all collisional excitation and deexcitation rates out of the excited and ground states.

3) Doppler broadening

When a monochromatic source of light is moving towards or away from an observer, the light appears to be shifted in frequency due to the Doppler effect. The frequency of the radiation from each atom depends on its velocity through the Doppler shift $\omega = \omega_0(1 + \upsilon/c)$

, where ω_0 is the frequency of light source when it is still, and υ is the velocity at which the light source moves, as shown in Figure 1-15.

The radiation field emitted by a moving atom can be expressed as

$$E(t) = \exp[ikr(t) - i\omega_0 t] \tag{1.43}$$

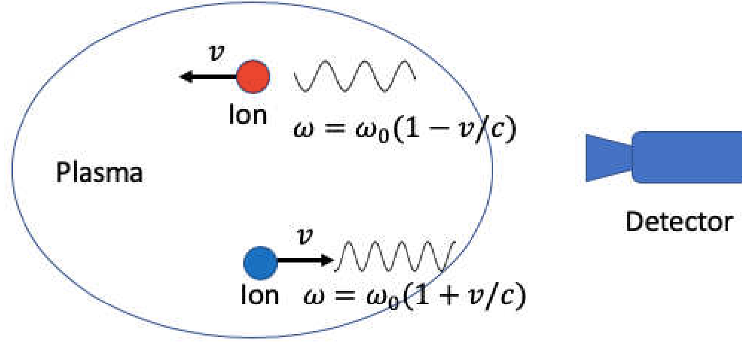

Figure 1-15 The schematic of Doppler effect of ions in a plasma.

In which $r(t) = r_0 + \int_0^t v(t')dt'$ is the position of the moving atom. Then the autocorrelation function is

$$g(\tau) = Re\langle E(t) \cdot E^*(t+\tau)\rangle = Re\langle \exp[ikr(\tau) - i\omega_0\tau]\rangle \tag{1.44}$$

In which, $r(t) = \int_t^{t+\tau} v(t')dt' = v\tau$. Assuming atoms do not collide ever, for a Maxwellian velocity distribution within the plasma

$$f(v) = \left[\frac{m}{2\pi kT}\right]^{\frac{3}{2}} exp\left[\frac{-m|v|^2}{2kT}\right] \tag{1.45}$$

ere m and T are the mass and temperature of the atoms respectively. Then the autocorrelation function is

$$g(\tau) = Re\langle \exp(-i\omega_0\tau) \int_{-\infty}^{\infty} \exp(-ikv\tau)\, f(v) d\,v\rangle = exp\left[\frac{-k_0^2\tau^2}{4\left[\frac{m}{2kT}\right]}\right] cos\omega_0\tau \tag{1.46}$$

according to Wiener-Khintchine theorem, the spectral density $L(\omega)$ of a radiation system and the autocorrelation function $g(\tau)$ of its radiated electric field $E(t)$ are a pair of Fourier transform.

$$L(\omega) = \frac{1}{\pi}\int_0^{\infty} \cos(\omega\tau)\, g(\tau) d\,\tau \tag{1.47}$$

From which the Doppler line profile is obtained as

$$L(\omega) = \frac{c}{\omega_0}\left[\frac{m}{2\pi kT}\right]^{\frac{1}{2}} exp\left[\frac{-4ln2(\omega-\omega_0)^2}{\Delta\omega^2}\right] \tag{1.48}$$

ere $\Delta\omega = \omega_0\left[\frac{8kTln2}{mc^2}\right]^{1/2}$ is the FWHM of the Doppler line profile. Since the atoms in a plasma move into different directions, each atom radiates at a different frequency. For this reason, the Doppler broadening is called inhomogeneous broadening. Thus, the spectrum of the plasma is the superposition of the spectra of the individual atoms.

As seen above, the homogeneous broadenings, including natural broadening and electron collisional broadening, have Lorentzian profiles, while the inhomogeneous broadening, the Doppler broadening, has a Gaussian profile. Voigt profile combines these two profiles together by convolution

$$V(x,\sigma,\gamma) = \int G(x',\sigma)L(x-x',\gamma)dx \tag{1.49}$$

And the linewidth of the Voigt profile would be obtained by associating the width of Gaussian profile $\Delta\nu_G$ and Lorentzian profile $\Delta\nu_L$by

$$\Delta\nu_V = 0.5346\Delta\nu_L + \sqrt{0.2166\Delta{\nu_L}^2 + \Delta{\nu_G}^2} \tag{1.50}$$

The line broadening mechanisms make plasma more transparent to the emission generated from the inner region. Since the natural broadening and electron collision broadening are homogeneous broadening, they can be considered to be isotropic while the Doppler broadening is not because the Doppler shift depends on the velocity of the ions. In a plasma created by

focusing a laser onto a flat target, the plasma expands fast into space. It is known that the average kinetic energy of ions is highest in the normal direction of the flat target and decreases with the angle θ with respect to the normal direction, in a manner of $cos^2\theta$ [75]. Thus, the Doppler shift of ions also has a maximum in the normal direction of the target and decrease with the angle θ. The Doppler shift causes a shift of the resonance line of the absorption of ions in the outer region so that they absorb and emit at slightly shifted wavelengths. Consequently, a photon that is generated in the inner region of a plasma and travels in a direction which has a small angle with respect to the normal has longer mean free path and better chance to escape the plasma. The line broadening mechanism is well covered in reference [74].

1.7.3 Consequences of Opacity

Due to the high opacity of the Sn LPP, the EUV emitted from the inner region of the Sn LPP is re-absorbed when propagating through the surrounding plasma. Most of the EUV emission is found to originate from an under-density plasma region, which has a range of electron density of 10^{19}-10^{20} cm^{-3} [76], as shown in Figure 1-16. The opacity is anisotropic in the Sn LPP, and this anisotropy shapes the angular distribution of EUV emission. One of the two reasons that lead to the anisotropy of opacity is the Doppler effect which is mentioned above. The other reason is discussed next. For a Sn LPP created on a flat solid target, there is a cold dense plasma forming at the periphery of the laser focus due to two mechanisms: three-dimensional expansion and the ablation of the target surface around the laser focus by the plasma emission, which were discussed in section 1.5.2, resulting attenuated intensity over the entire wavelength range of interest, as shown in Figure 1-17. This cold and dense plasma covers the region corresponding to

large angles with respect to the target normal. In contrary, at the angles close to the laser axis the Sn LPP is heated by the incident laser during the whole laser pulse duration so that the temperature of the plasma in this region is relatively higher than that of the peripheral plasma and the tin ions in this region are highly charged. In this region, absorption of Sn LPP is mainly caused by resonance absorption of highly charged tin ions Sn VII to Sn XI. The resonance absorption has a pseudo-discrete feature due to 4p-4d and 4d-4f transitions, causing local dips in the spectral emission of Sn LPP, as shown in Figure 1-18.

The opacity not only causes losses of EUV emission but also causes a broadening of the EUV spectrum. This broadening can be attributed to the increased satellite lines due to the re-absorption of EUV emission and re-emitting of light over a broader spectral range [77]. Due to the narrow reflectivity band of the Mo/Si mirror, the broadening of EUV emission also results in a reduction of the CE. Because in a EUV stepper, six or more Mo/Si mirrors are used to project the pattern on the mask onto the wafer, the total transmission bandwidth of the projection system is much narrower than the bandwidth of a single Mo/Si mirror, which is why the CE is defined as the in-band EUV (~2% bandwidth) energy over the laser energy.

1.7.4 Methods to reduce opacity

There are several methods of reducing the opacity of Sn LPP. One method is using a longer wavelength of laser. Longer laser wavelength leads to lower electron density. This, in turn, leads to lower opacity and narrower spectral emission due to low opacity of the plasma[80]. When a Sn LPP is created, the energy of the laser is primarily deposited near the critical density. For an

Nd: YAG laser of $\lambda = 1.06\ \mu m$, the critical density $n_c = 1.1\ \times 10^{21} cm^{-3}$. For a CO_2 laser of $\lambda =$ $10.6\ \mu m$, the critical density $n_c = 1 \times 10^{19} cm^{-3}$.

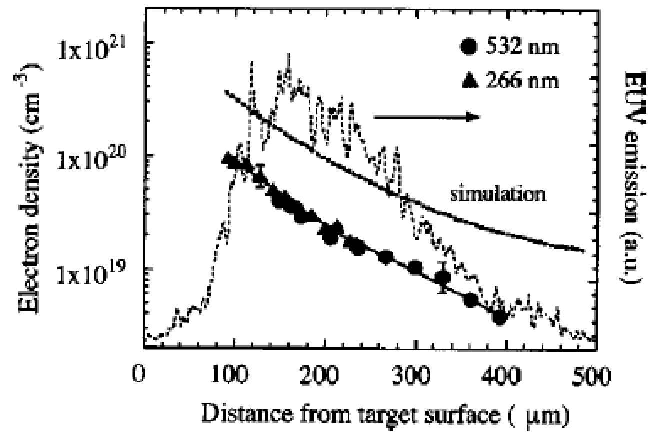

Figure 1-16 Electron density profile from interferometers employing probe laser at wavelength of 532 nm (circle) and 266 nm (square) respectively. 1D radiation hydrodynamic simulation (dashed line) and EUV emission profile (dotted line). The solid lines represent the exponential fits to the experimental data with scale lengths of 70 and 120 μm [76].

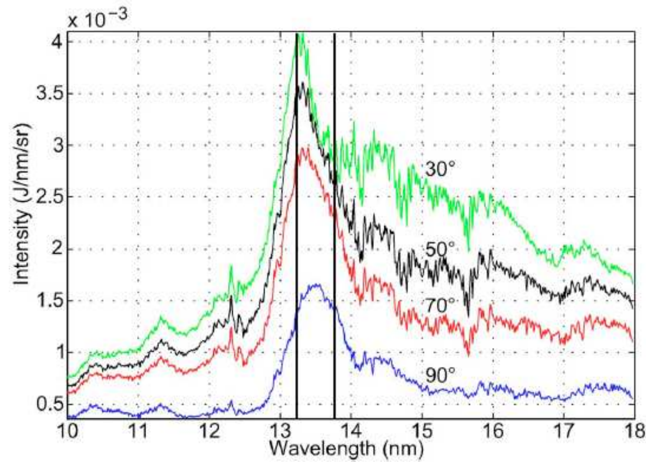

Figure 1-17 Emission spectra from a Sn LPP recorded at 20°, 40°, 60°, and 80° from the target normal [78].

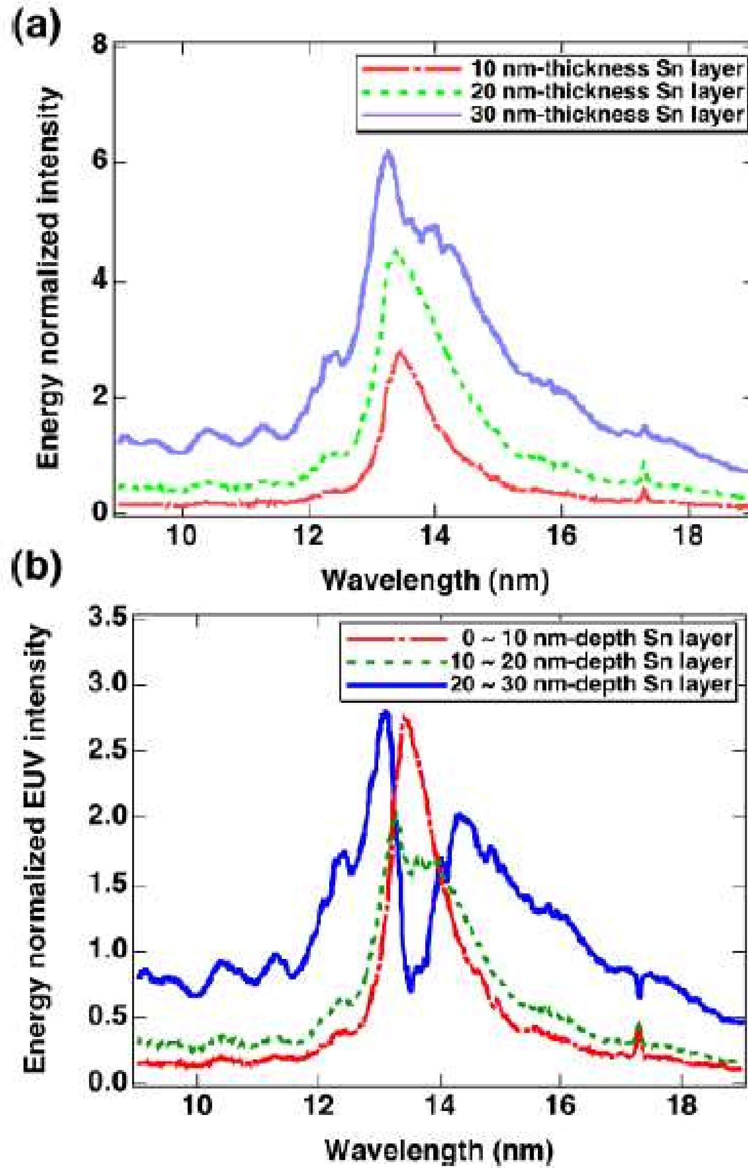

Figure 1-18 (a) EUV spectra emitted from spherical targets coated with 10, 20, 30 nm-thick tin layers. (b) EUV spectra emitted from 0-10, 10-20, and 20-30 nm-depth tin layers. The EUV spectra from 10-20 and 20-30 nm-depth tin layer were obtained by subtracting the 20 nm spectrum by the 10 nm spectrum and subtracting the 30 nm spectrum by the 20 nm spectrum respectively in (a) [79].

Consequently, for Nd: YAG laser the irradiation laser energy is mainly deposited in the high-density region, which is very near the target surface, while for CO_2 laser the irradiation laser energy is deposited in a lower density region of plasma from where most of the EUV emission comes. This leads to efficient heating of the Sn LPP and hence higher CE using CO_2 laser.

Additionally, since the irradiation energy is deposited in the low-density region for a CO_2 LPP, the spectral bandwidth of the EUV emission from the CO_2 LPP is narrower than that of the EUV emission from an Nd: YAG LPP, for that the low opacity of the CO_2 LPP suppresses the out-of-band emission, as Figure 1-19 illustrates.

Another method is using targets of low initial density. The plasma density is governed not only by irradiation laser parameters but also by the target properties. Fujikoa et al. studied opacity effects and suggested that the optical thickness of Sn plasma can be controlled by reducing the initial target density [77]. A way to do this is doping Sn atoms into low-Z material. A typical UTA recorded from a full-density tin target and a Sn-doped foam target with a 0.5% density is shown in Figure 1-20. Significant suppression of out-of-band emission and a narrowed spectrum peaked at 13.5 nm is observed, attributed to a reduction of satellite emission and less opacity broadening during radiation transportation. Although the Sn atomic number density of low-density targets is only 0.5% of that of the full-density target, the low-density target produces a CE that is close to that of the full-density tin target. This again indicates that the opacity of the full-density Sn LPP is very high. However, a drawback is that the relative number of emitting atoms is reduced and the electrons deposit energy in ionizing and exciting species that do not emit in the band of interest, which prohibits the increase of the EUV CE. Consequently, the current commercial EUV lithography sources use liquid tin.

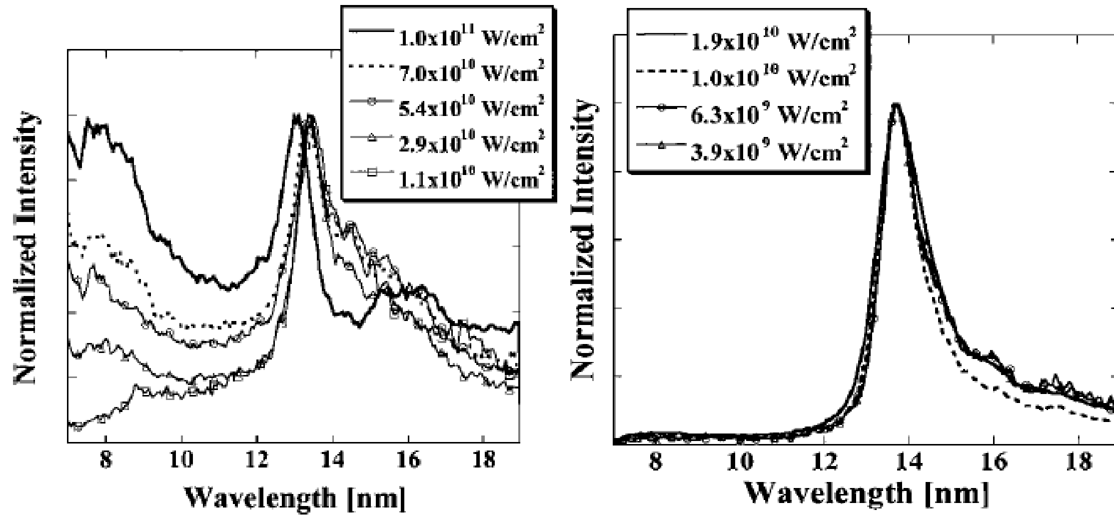

Figure 1-19 (left) the EUV spectra of Nd: YAG LPP as a function of laser intensity. (right) the EUV spectra of CO_2 LPP as a function of laser intensity [21].

1.8 Materials emitting near $\lambda = 13.5$nm

Although the Sn LPP source is now supporting HVM, several other materials were initially considered, including xenon and lithium.

Lithium LPP has intense EUV emission near 13.5 nm, and the spectral bandwidth of its EUV emission is narrow because only a single transition 2p->1s in Li^{2+} (H-like) is relevant. The spectral emission of the lithium LPP has discrete lines due to the low Z of the lithium atom, as shown in Figure 1-21. However, also because a single transition is responsible for the emission, opacity is high and CE of lithium LPP is relatively low. The H-like lithium ion Li^{2+} population is most abundant when plasma temperature is about 20 eV. However, at this temperature, the rate of electron impact excitation is low. Consequently, the CE of lithium LPP is as low as 1.2% [20]. Moreover, lithium is a difficult metal to handle. Consequently, lithium is not considered to be the target material of the light source for HVM EUVL stepper.

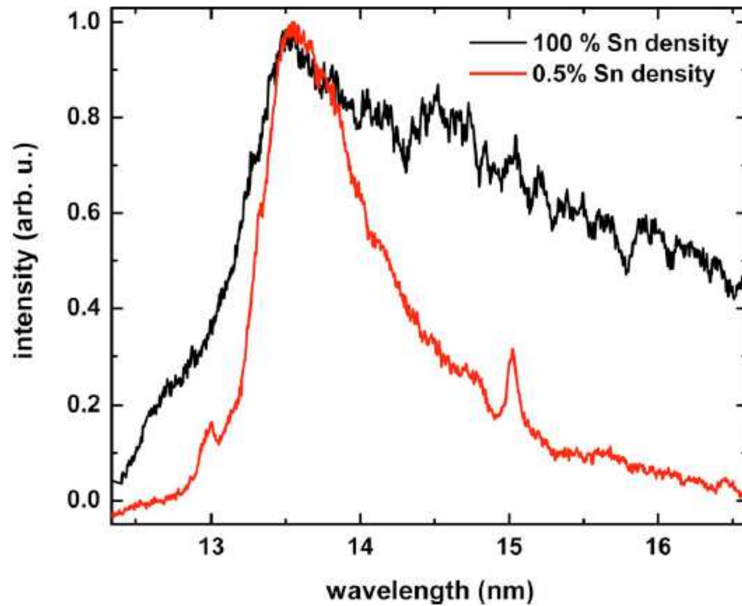

Figure 1-20 UTA obtained from full-density and 0.5% density tin. The UTA spectrum from Sn-doped foam targets showed distinct narrowing. Both spectra were recorded with a laser intensity of $4 \times 10^{11}\ W/cm^2$ [81].

Xenon is a noble gas. Consequently, its stable chemical characteristics and gaseousness at ambient temperature mitigate the challenge of debris mitigation. However, the strongest maximum of the spectral emission of xenon LPP is near 11 nm instead of 13.5 nm[82,83], as shown in Figure 1-22. Only the 4d-5p transitions of Xe^{10+} ion emits near 13.5 nm with a decent intensity [84], resulting in a low CE of xenon LPP (<1%) [21][23] near 13.5 nm which is 5 times lower than the CE of Sn LPP at 13.5 nm. The low CE of xenon LPP requires a high irradiation energy input to meet HVM EUV source power requirements. Due to the low CE of xenon LPP, it is not expected to deliver the power required for EUV source in HVM.

In a Sn LPP, a wide range of Sn ion species (Sn^{8+}-Sn^{14+}) emit near 13.5 nm, forming an n=4-4 unresolved transition array (UTA) and resulting strong in-band EUV emission, as shown in Figure 1-22. Theoretically estimated CE of Sn LPP as high as 7% have been reported[24], which makes Sn LPP the leading material for EUV sources for large volume manufacturing along with other factors such as manageable debris and feasible fuel delivery. A great deal of effort, including

scientific research and engineering, has been put into increasing the CE of Sn LPP from a low level.

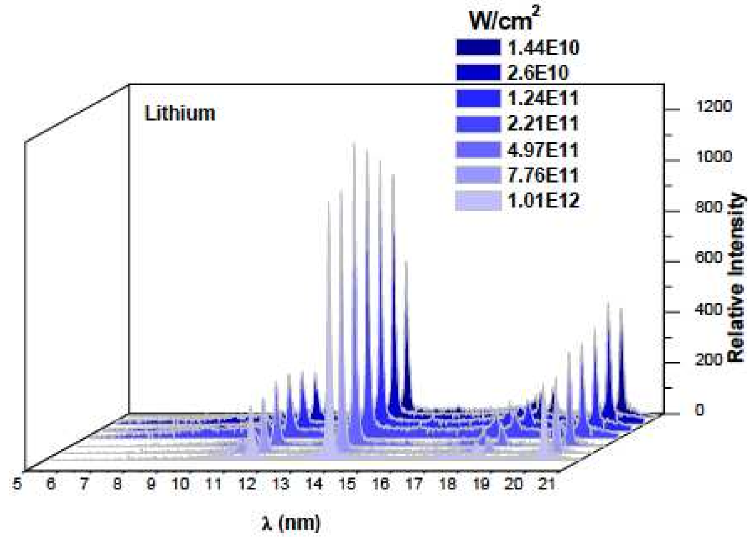

Figure 1-21 the spectral emission of lithium LPP [85].

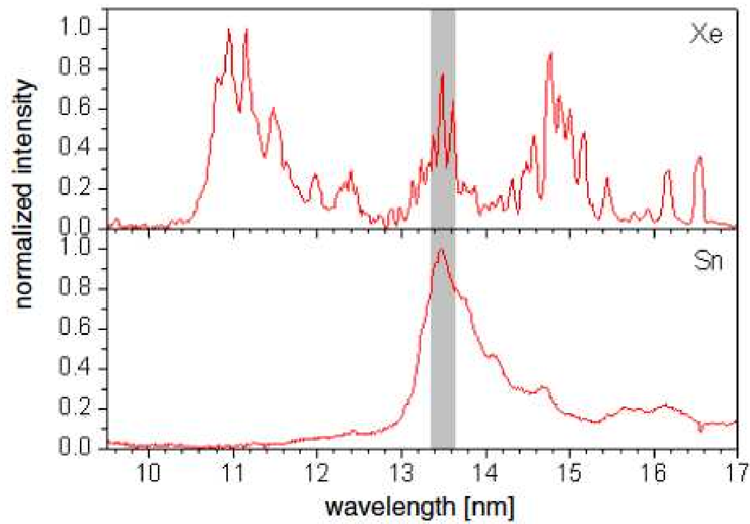

Figure 1-22 Typical spectra obtained from xenon (top) and with tin (bottom) using a gas discharge. The grey band indicates the 2% bandwidth that can be used by an 11-mirror system [86].

1.9 The dependence of CE on the laser pulse temporal profile

1.9.1 The dependence of CE on laser pulse duration

Longer laser pulse creates a plasma with a larger volume. The ablation thickness d_a in centimeters of a solid density tin layer irradiated by a laser with a wavelength λ in μm, an intensity I in W/cm^2, and a pulse duration t_L in seconds, is estimated to be [87]

$$d_a = \frac{2.8 \times 10^3 \left(\frac{I}{10^{11}}\right)^{\frac{5}{9}} \left(\frac{\lambda}{1.064}\right)^{-\frac{4}{3}} t_L}{\rho_0} \tag{1.51}$$

Where ρ_0 is the initial density of the target in $\frac{g}{cm^3}$and equals to 7.265 $\frac{g}{cm^3}$ for tin. A larger emitting volume is resulted from the larger ablation depth. Reference [88] found that the CE of a Cu LPP into keV X-ray increases with pulse duration from 130 ps to 400 ps and then starts to saturate for pulse duration longer than 400 ps, as shown in Figure 1-23.

The saturation may be caused by increased opacity with larger ablation depth and three-dimensional expansion which could be dominant after τ ($C_s\tau \sim$ focal spot size). The mass absorption coefficient of Sn LPP at 13.5 nm is measured to be κ=$0.96 \pm 0.18 \times \frac{10^5 cm^2}{g}$[79]. Consequently, the optical depth can be quantified as:

$$\tau = \kappa d_a \rho_0 = (2.7 \pm 0.5) \times 10^8 \left(\frac{I_L}{10^{11}}\right)^{\frac{5}{9}} \left(\frac{\lambda}{1.064}\right)^{-\frac{4}{3}} t_L \tag{1.52}$$

$$= (2.7 \pm 0.5) \times 10^{8} \left(\frac{E_L}{10^{11}}\right)^{\frac{5}{9}} \left(\frac{\lambda}{1.064}\right)^{-\frac{4}{3}} t_L^{\frac{4}{9}} \tag{1.53}$$

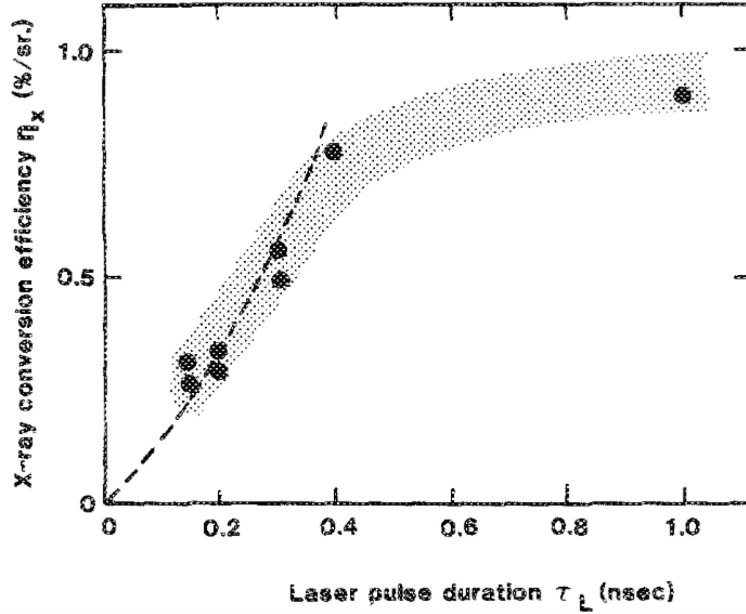

Figure 1-23 X-ray conversion efficiency as a function of a Gaussian laser pulse duration at 1x10^{14} W/cm^{2} [88].

The optical depth is proportional to the $t_L^{\frac{4}{9}}$ of the irradiation laser, as shown in Equation 1-8, indicating that a longer pulse duration leads to a larger optical depth [79]. Additionally, in the EUV region, the trend of CE is that it increases with laser pulse duration at first and then decreases with longer pulse duration after reaching a maximum. Previous work used a Q-switched $\lambda = 1.064\ \mu\mathrm{m}$ laser to create Sn LPP on planar targets. In a pulse duration range from 1.2ns to 8.5ns the CE maximum was found at 2.3 ns, and decreases for both longer and shorter pulse duration[87]. This could be a result of a balance between emitting volume and opacity as well as three-dimensional expansion loss.

1.9.2 Enhancement of CE by using a pre-pulse

Researches have shown that a dual irradiation pulse scheme can help to increase the CE of Sn LPP effectively. A dual irradiation pulse scheme, which was used to irradiate a low SnO_2 concentration (6%) aqueous solution microjet target, yields a CE of Sn LPP which is almost two times higher than the CE that yielded using a single irradiation pulse, as shown in Figure 1-24 [89]. Leading technology of generating EUV for lithography for high volume manufacturing (HVM) uses melted tin droplets as targets. A CE of 4.7% is obtained by combining a target geometry of melted tin droplet and a dual irradiation pulse scheme. The prepulse has a pulse energy of 2mJ and a pulse duration of 10 ps [90]. A prepulse at wavelength of 1.06 μm is used to create a cloud of tin out of a tin droplet with 20 μm diameter and the main pulse at wavelength of 10.6 μm comes in ~100ns later when the cloud of tin expands a disk with a diameter of ~300μm which matches the focal spot size of the CO_2 laser, as shown in Figure 1-25

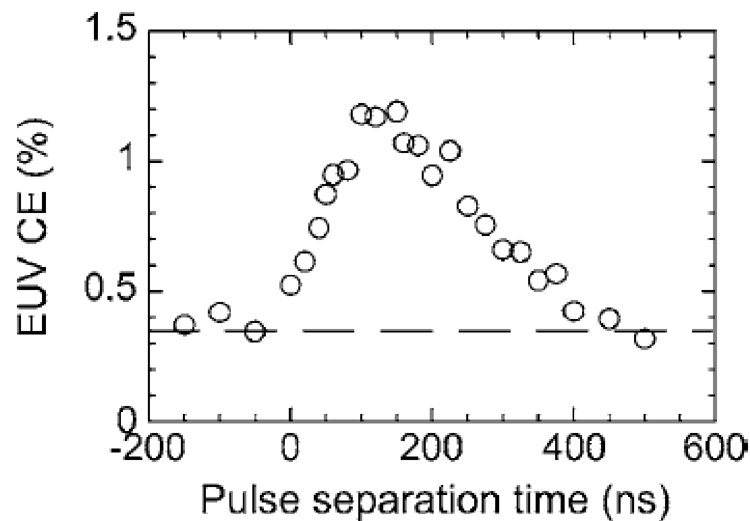

Figure 1-24 The EUV CE as a function of a pulse separation time of dual laser pulses [89].

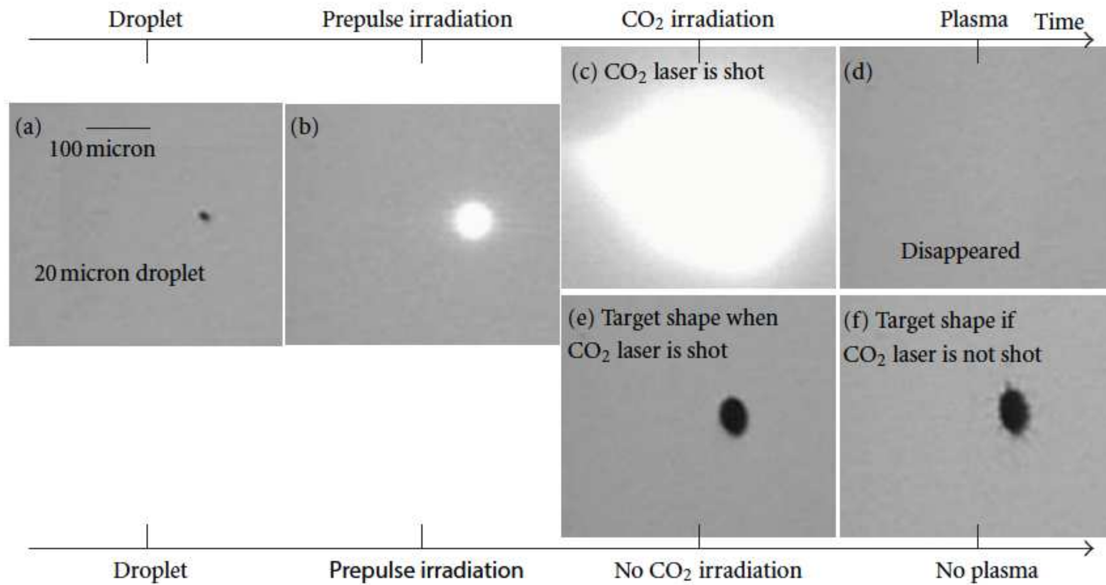

Figure 1-25 Shadowgraph images of tin fragments. (a) the Sn droplet. (b) The Sn droplet is irradiated by a prepulse laser originating from left hand side in the image. During laser irradiation, the Sn droplet is displaced away from the irradiation point while simultaneously expanding in diameter. (c) shows the images with the main CO2 laser irradiation. (d) is captured immediately after the EUV light emission. When irradiation condition is optimized, the fragments have disappeared from the shadowgraph image. (e) and (f) shows the images after the prepulse laser irradiation without the main CO2 laser irradiation [90].

It is found that the CE of Sn LPP increases with higher energy of the prepulse which may be due to a higher expansion speed of the tin cloud [91]. Additionally, a 10 ps prepulse yields a maximum CE of 4.7% while a 10ns prepulse yields a maximum CE of 3.8% because that 10 ps prepulse creates a tin cloud with finer fragments and higher expansion speed [90].

There are three advantages of using double irradiation pulse scheme on the tin droplet. Firstly, the cloud of tin has a low initial density after it expands. A Sn LPP created from a low-density target will have low opacity, as mentioned above. Secondly, the main pulse can penetrate the expanded tin cloud, thus the Sn LPP will have a relatively uniform plasma temperature and the density gradient will be small. Thirdly, the small size of tin droplet reduces the tin debris. Given the success that the dual pulse scheme has achieved, in Chapter 3 of this thesis we introduce a

novel pulse synthesizer which can generate up to 10 sub-pulses which can be either used as pre-pulses or used to construct a main pulse with arbitrary temporal shapes.

1.10 Lithography beyond EUV

While the EUVL using Sn LPP as the light source started to be used in HVM, the semiconductor industry starts to eye the future when the EUVL at 13.5 nm reaches its limit. The wavelength of 6.x nm is attracting much attention to further shrink feature size in the future due to the availability of high-reflectivity mirrors based on La/B multilayer coating in this wavelength range. Theoretically, the multilayer structure La/B provides a reflectivity at normal incidence of R=80%, which is even higher than that of Mo/Si at λ=13.5 nm. And a high reflectivity of La/B mirror, R=64.1%, was achieved experimentally as shown in Figure 1-26. The accurate value of 6.x nm will be determined by the combination of source emission and reflectivity that provides optimum efficiency and in-band EUV yield. BEUV lithography at 6.x nm based on Gd/Tb LPP is under investigation because Gd/Tb LPP emits intensely at this wavelength. Detailed characterization of Gd/Tb LPP is going to be discussed in Chapter 4.

The rare-earth elements Gd and Tb with the partially filled 4d and 4f subshells produce strong narrowband emission near 6.x nm as illustrated in Figure 1-27, which is attributed to an n = 4 - n = 4 (Δn = 0) unresolved transition array (UTA), as shown in Figure 1-28. Typical examples of these transitions are $4p^6 4d^m – (4p^5 4d^{m+1} + 4p^6 4d^{m-1} 4f)$ in 4d-ions and $4d^{10} 4f^m – 4d^9 4f^{m+1}$ in 4f-ions. The anomalously high intensities of these peaks are associated with the following reasons: 1) n=4–4 transitions have much higher transition probabilities than the other transitions in the

corresponding spectra; 2) $\Delta n = 0$ transition wavelengths very weakly depend on the number of electrons in the outer subshells; 3) n=4–4 transitions in 4d-ions and in 4f-ions are localized in the same spectral region for a given element. As a consequence, the n=4–4 transitions are concentrated within the relatively narrow spectral bandwidth for a given element and dominate in the EUV spectra excited in a wide variety of plasma sources [12].

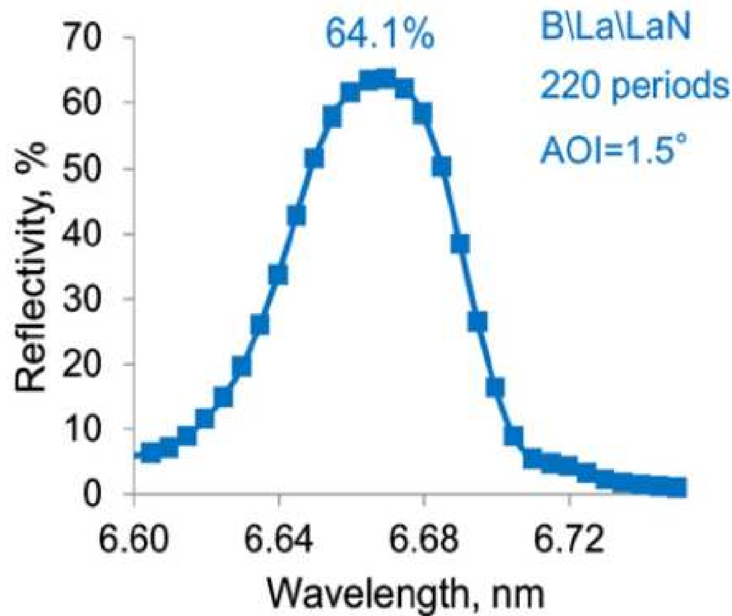

Figure 1-26 Measured reflectivity of La/B based multilayer mirror [92].

The spectral behavior of Gd and Tb LPP is expected to be similar to that of Sn LPP because their emissions are all dominated by 4d open-shell ions. For instance, the spectral emission of Gd (VIII-XXVIII) and Tb (IV-XXIX) ions becomes narrower and is shifted to shorter wavelengths when the ion charge increases. However, once the 4d shell is opened, more ground states become available, resulting in broader spectral bands and longer central wavelength, as shown in Figure 1-29.

In order to have the abundance of Gd^{20+}-Gd^{22+} and Tb^{21+}-Tb^{23+} , species which emit intensely near 6.x nm, a plasma temperature of ~ 144 eV for Gd LPP and ~ 152 eV for Tb LPP and an electron density of $10^{21}\ cm^{-3}$ is required [93]. In order to achieve high conversion efficiency, the opacity of the Gd LPP needs to be reduced by using long irradiation wavelength [94] and low initial density target [95], etc.

ASML has succeeded in scaling the power of 13.5 nm EUV sources to a level that is enough for HVM. A microscopic tin droplet, which is injected into a vacuum chamber at high speed at up to 100 kHz, is vaporized by a pre-pulse first and then turned into tin plasma by a main pulse generated by a high-power CO_2 laser. This approach has produced average powers up to 250W [57]. However, further increases in source power are still desired to increase wafer throughput. The rest of this Dissertation that describes works in support the future of EUV lithography is divided as follows. The possibility of increasing CE using synthesized laser pulses of arbitrary shapes is investigated. We found that synthesized with a square pulse shape can help boost the CE of Sn LPP by 35%, which is discussed in Chapter 2. In Chapter 3 of this thesis, the novel apparatus that is used to generate synthesized laser pulses of arbitrary shapes is described. Our extensive work on the characterization of BEUV emission from Gd/Tb LPP is discussed in Chapter 4.

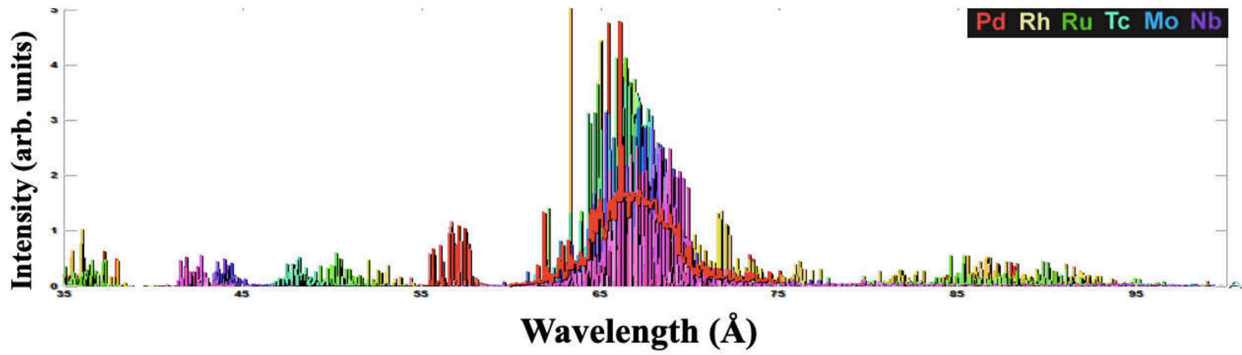

Figure 1-27 Atomic simulation covering broad spectral range shows EUV emission of Gd concentrates near 6.7 nm (Radex code, HULLAC Atomic Data). Plasma conditions: electron temperature (130 eV), electron density (5×10^{20} cm^{-3}), spot size: 100 micrometers.

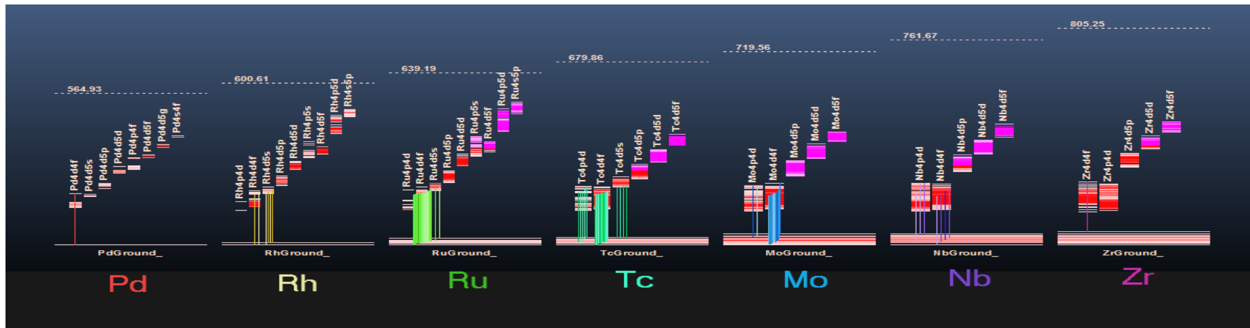

Figure 1-28 Energy level diagram of Gadolinium (Gd).

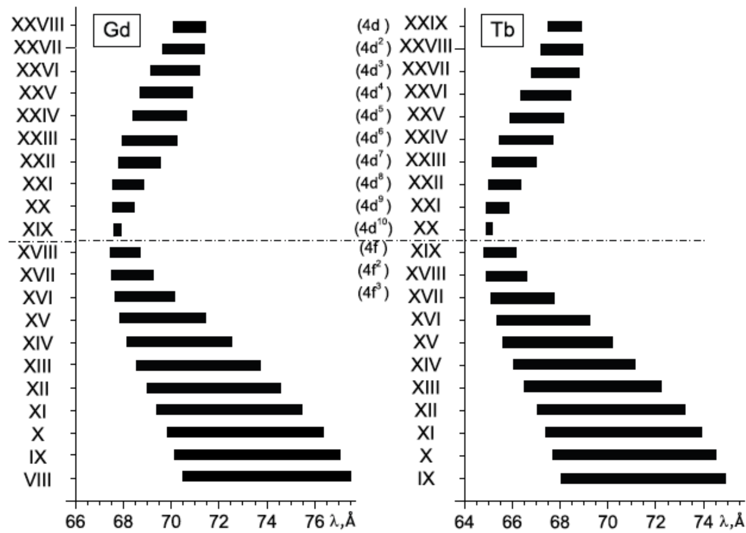

Figure 1-29 The calculated wavelength bands of the most intense 4–4 transition in the spectra of the rare-earth 4d- and 4f-ions [96].

References

1. D. Attwood, *Soft X-Rays and Extreme Ultraviolet Radiation: Principles and Applications* (Cambridge University Press, 1999).

2. E. Spiller, "Reflective multilayer coatings for the far uv region," Appl. Opt. **15**(10), 2333–2338 (1976).

3. J. H. Underwood and T. W. Barbee Jr., "Layered synthetic microstructures as Bragg diffractors for X rays and extreme ultraviolet: theory and predicted performance," Appl. Opt. **20**(17), 3027–3034 (1981).

4. E. H. Anderson and D. Kern, "Nanofabrication of Zone Plates for X-Ray Microscopy," in *X-Ray Microscopy III*, A. G. Michette, G. R. Morrison, and C. J. Buckley, eds. (Springer Berlin Heidelberg, 1992), pp. 75–78.

5. E. H. Anderson, "Specialized electron beam nanolithography for EUV and X-ray diffractive optics," IEEE J. Quantum Electron. **42**(1), 27–35 (2006).

6. D. T. Attwood, P. Naulleau, K. A. Goldberg, E. Tejnil, C. Chang, R. Beguiristain, P. Batson, J. Bokor, E. M. Gullikson, M. Koike, H. Medecki, and J. H. Underwood, "Tunable coherent radiation in the soft X-ray and extreme ultraviolet spectral regions," IEEE J. Quantum Electron. **35**(5), 709–719 (1999).

7. J. J. Rocca, V. Shlyaptsev, F. G. Tomasel, O. D. Cortazar, D. Hartshorn, and J. L. A. Chilla,

"Demonstration of a discharge pumped table-top soft-x-ray laser," Phys. Rev. Lett. **73**(16), 2192 (1994).

8. B. M. Luther, Y. Wang, M. A. Larotonda, D. Alessi, M. Berrill, M. C. Marconi, J. J. Rocca, and V. N. Shlyaptsev, "Saturated high-repetition-rate 189-nm tabletop laser in nickellike molybdenum," Opt. Lett. **30**(2), 165 (2005).

9. A. Rundquist, C. G. Durfee, Z. Chang, C. Herne, S. Backus, M. M. Murnane, and H. C. Kapteyn, "Phase-matched generation of coherent soft x-rays," Science (80-.). **280**(5368), 1412–1415 (1998).

10. D. J. Nagel, C. M. Brown, M. C. Peckerar, M. L. Ginter, J. A. Robinson, T. J. McIlrath, P. K. Carroll, T. J. Mcllrath, and P. K. Carroll, "Repetitively pulsed-plasma soft x-ray source," Appl. Opt. **23**(9), 1428–1433 (1984).

11. D. A. Tichenor, G. D. Kubiak, M. E. Malinowski, R. H. Stulen, S. J. Haney, K. W. Berger, R. P. Nissen, G. A. Wilkerson, P. H. Paul, S. R. Birtola, P. S. Jin, R. W. Arling, A. K. Ray-Chaudhuri, W. C. Sweatt, W. W. Chow, J. E. Bjorkholm, R. R. Freeman, M. D. Himel, A. A. MacDowell, D. M. Tennant, L. A. Fetter, O. R. Wood II, W. K. Waskiewicz, D. L. White, D. L. Windt, and T. E. Jewell, "Development of a laboratory extreme-ultraviolet lithography tool," Electron-Beam, X-Ray, Ion-Beam Submicrom. Lithogr. Manuf. IV **2194**(May 1994), 95 (2005).

12. S. S. Churilov, R. R. Kildiyarova, A. N. Ryabtsev, and S. V. Sadovsky, "EUV spectra of Gd and Tb ions excited in laser-produced and vacuum spark plasmas," Phys. Scr. **80**(4), 2–8 (2009).

13. A. V Prokofiev, V. M. Borisov, A. V Eltsov, V. A. Mishchenko, V. A. Vodchits, A. Y.

Vinokhodov, Y. B. Kiryukhin, O. B. Khristoforov, and A. S. Ivanov, "EUV sources using Xe and Sn discharge plasmas," J. Phys. D. Appl. Phys. **37**(23), 3254–3265 (2004).

14. D. B. Sinars, R. D. McBride, S. A. Pikuz, T. A. Shelkovenko, D. F. Wenger, M. E. Cuneo, E. P. Yu, J. P. Chittenden, E. C. Harding, S. B. Hansen, B. P. Peyton, D. J. Ampleford, and C. A. Jennings, "Investigation of high-temperature bright plasma X-ray sources produced in 5-MA X-pinch experiments," Phys. Rev. Lett. **109**(15), 1–5 (2012).

15. R. L. Sandberg, A. Paul, D. A. Raymondson, S. Hädrich, D. M. Gaudiosi, J. Holtsnider, R. I. Tobey, O. Cohen, M. M. Murnane, H. C. Kapteyn, C. Song, J. Miao, Y. Liu, and F. Salmassi, "Lensless diffractive imaging using tabletop coherent high-harmonic soft-X-ray beams," Phys. Rev. Lett. **99**(9), 1–4 (2007).

16. W. Li and M. C. Marconi, "Extreme ultraviolet Talbot interference lithography," Opt. Express **23**(20), 25532 (2015).

17. I. Kuznetsov, J. Filevich, F. Dong, M. Woolston, W. Chao, E. H. Anderson, E. R. Bernstein, D. C. Crick, J. J. Rocca, and C. S. Menoni, "Three-dimensional nanoscale molecular imaging by extreme ultraviolet laser ablation mass spectrometry," Nat. Commun. **6**, 1–6 (2015).

18. Y. Wang, L. Yin, S. Wang, M. C. Marconi, J. Dunn, E. Gullikson, and J. J. Rocca, "Single-shot soft x-ray laser linewidth measurement using a grating interferometer," Opt. Lett. **38**(23), 5004 (2013).

19. D. Brandit, "Laser - produced plasma presents most viable route to EUV lithography," LaserFocusWorld (2007).

20. R. W. Coons, D. Campos, M. Crank, S. S. Harilal, and A. Hassanein, "Comparison of EUV spectral and ion emission features from laser-produced Sn and Li plasmas," Extrem. Ultrav. Lithogr. **7636**(March 2010), 763636 (2010).

21. H. Tanaka, K. Akinaga, A. Takahashi, and T. Okada, "Emission characteristics of extreme ultraviolet radiation from CO 2 laser-produced xenon plasma," Japanese J. Appl. Physics, Part 2 Lett. **43**(4 B), 2–5 (2004).

22. G. D. Kubiak, L. J. Bernardez II, and K. D. Krenz, "High-power extreme-ultraviolet source based on gas jets," (June 1998), 81 (1998).

23. B. A. M. Hansson, L. Rymell, M. Berglund, O. E. Hemberg, E. Janin, H. M. Hertz, and J. Thoresen, "Liquid-xenon-jet laser-plasma source for EUV lithography," Soft X-Ray EUV Imaging Syst. II **4506**(December 2001), 1–8 (2003).

24. K. Nishihara, A. Sunahara, A. Sasaki, M. Nunami, H. Nishimura, T. Kato, S. Fujioka, F. Koike, M. Murakami, K. Fujima, V. Zhakhovskii, T. Nishikawa, H. Tanuma, N. Miyanaga, A. Takata, R. More, K. Gamata, K. Mima, Y. Shimada, Y. Izawa, H. Ueda, and H. Furukawa, "Plasma physics and radiation hydrodynamics in developing an extreme ultraviolet light source for lithography," Phys. Plasmas **15**(5), 056708 (2008).

25. A. A. Schafgans, D. J. Brown, I. V. Fomenkov, R. Sandstrom, A. Ershov, G. Vaschenko, R. Rafac, M. Purvis, S. Rokitski, Y. Tao, D. J. Riggs, W. J. Dunstan, M. Graham, N. R. Farrar, D. C. Brandt, N. Böwering, A. Pirati, N. Harned, C. Wagner, H. Meiling, and R. Kool, "Performance optimization of MOPA pre-pulse LPP light source," Extrem. Ultrav. Lithogr.

VI **9422**, 94220B (2015).

26. M. A. Purvis, A. Schafgans, D. J. W. Brown, I. Fomenkov, R. Rafac, J. Brown, Y. Tao, S. Rokitski, M. Abraham, M. Vargas, S. Rich, T. Taylor, D. Brandt, A. Pirati, A. Fisher, H. Scott, A. Koniges, D. Eder, S. Wilks, A. Link, and S. Langer, "Advancements in predictive plasma formation modeling," in *Extreme Ultraviolet (EUV) Lithography VII* (International Society for Optics and Photonics, 2016), **9776**(March 2016), p. 97760K.

27. J. White, P. Hayden, P. Dunne, A. Cummings, N. Murphy, P. Sheridan, and G. O'Sullivan, "Simplified modeling of 13.5 nm unresolved transition array emission of a Sn plasma and comparison with experiment," J. Appl. Phys. **98**(11), (2005).

28. S. S. Churilov and A. N. Ryabtsev, "Analyses of the Sn IX-Sn XII spectra in the EUV region," Phys. Scr. **73**(6), 614–619 (2006).

29. K. Nishihara, A. Sunahara, A. Sasaki, M. Nunami, H. Tanuma, S. Fujioka, Y. Shimada, K. Fujima, H. Furukawa, T. Kato, F. Koike, R. More, M. Murakami, T. Nishikawa, V. Zhakhovskii, K. Gamata, A. Takata, H. Ueda, H. Nishimura, Y. Izawa, N. Miyanaga, and K. Mima, "Plasma physics and radiation hydrodynamics in developing an extreme ultraviolet light source for lithography," Phys. Plasmas **15**(5), (2008).

30. M. Purvis, I. V Fomenkov, A. A. Schafgans, M. Vargas, S. Rich, Y. Tao, S. I. Rokitski, M. Mulder, E. Buurman, and M. Kats, "Industrialization of a robust EUV source for high-volume manufacturing and power scaling beyond 250W," in *Extreme Ultraviolet (EUV) Lithography IX* (International Society for Optics and Photonics, 2018), **10583**(May 2018),

p. 1058327.

31. I. V Fomenkov, "Laser produced plasma EUV sources for HVM 7nm node lithography: progress in availability and prospects of power scaling," in *Extreme Ultraviolet (EUV) Lithography X* (International Society for Optics and Photonics, 2019), **10957**, p. 1095719.

32. J. S. Kilby and U. S. Kileby, "Miniaturized electronic circuits," (1964).

33. H. C. Pfeiffer, "Recent Advances in Electron-Beam Lithography for the High-Volume Production of VLSI Devices," IEEE Trans. Electron Devices **26**(4), 663–674 (1979).

34. L. Harriott, "Scattering with angular limitation projection electron beam lithography for suboptical lithography," J. Vac. Sci. Technol. B … **2130**(June), 2130–2135 (1997).

35. H. C. Pfeiffer, R. S. Dhaliwal, S. D. Golladay, S. K. Doran, M. S. Gordon, T. R. Groves, J. D. Rockrohr, J. J. Senesi, W. Stickel, and E. V Tressler, "Projection reduction exposure with variable axis immersion lenses : Next generation lithography," **2353**(2001), 2840–2846 (1999).

36. R. G. Hobbs, D. Su, V. R. Manfrinato, E. A. Stach, K. K. Berggren, H. Duan, and L. Zhang, "Resolution Limits of Electron-Beam Lithography toward the Atomic Scale," Nano Lett. **13**(4), 1555–1558 (2013).

37. V. Kuiper, B. J. Kampherbeek, M. J. Wieland, G. d. Boer, G. F. t. Berge, J. Boers, R. Jager, T. v. d. Peut, J. J. M. Peijster, E. Slot, S. W. H. K. Steenbrink, T. F. Teepen, and A. H. V v. Veen, "MAPPER: High Throughput Maskless Lithography," in *25th European Mask and*

Lithography Conference (2009), pp. 1–5.

38. K. Reimer, S. Eder-Kapl, M. Witt, C. Brandstaetter, H. Langfischer, H.-J. Doering, J. Heinitz, J. Eichholz, and E. Haugeneder, "Projection mask-less lithography (PML2): First results from the multi beam blanking demonstrator," Microelectron. Eng. **83**(4–9), 968–971 (2006).

39. R. Freed, T. Gubiotti, J. Sun, A. Cheung, J. Yang, M. Mccord, A. Carroll, U. Ummethala, L. Hale, J. Hench, S. Kojima, and C. F. Bevis, "Reflective electron-beam lithography performance for the 10 nm logic node," in *SPIE Photomask Technology* (International Society for Optics and Photonics, 2012), **8522**, pp. 1–9.

40. F. Kidwingira, A. Brodie, W.-C. Wang, J. F. Sun, B. Vereecke, W. M. Tong, J. Yang, A. Carroll, T. Gubiotti, C. Bevis, L. Haspeslagh, S.-J. Lin, and R. Freed, "Reflective electron beam lithography: lithography results using CMOS controlled digital pattern generator chip," Altern. Lithogr. Technol. V **8680**(August 2015), 86800H (2013).

41. F. Hua, Y. Sun, A. Gaur, M. A. Meitl, L. Bilhaut, L. Rotkina, J. Wang, P. Geil, M. Shim, J. A. Rogers, and A. Shim, "Polymer imprint lithography with molecular-scale resolution," Nano Lett. **4**(12), 2467–2471 (2004).

42. H. Lan and Y. H. Ding, "Nanoimprint Lithography," in *Lithography Rijeka: InTech* (2010).

43. H. J. Mamin and D. Rugar, "Thermomechanical writing with an atomic force microscope tip," Appl. Phys. Lett. **61**(8), 1003–1005 (1992).

44. J. A. Dagata, J. Schneir, H. H. Harary, C. J. Evans, M. T. Postek, and J. Bennett, "Modification

of hydrogen-passivated silicon by a scanning tunneling microscope operating in air," Appl. Phys. Lett. **56**(20), 2001–2003 (1990).

45. R. Garcia, R. V. Martinez, and J. Martinez, "Nano-chemistry and scanning probe nanolithographies," Chem. Soc. Rev. **35**(1), 29–38 (2006).

46. J. W. Lyding, T. C. Shen, J. S. Hubacek, J. R. Tucker, and G. C. Abeln, "Nanoscale patterning and oxidation of H-passivated Si(100)-2×1 surfaces with an ultrahigh vacuum scanning tunneling microscope," Appl. Phys. Lett. **64**(15), 2010–2012 (1994).

47. C. Wagner and N. Harned, "EUV lithography: Lithography gets extreme," Nat. Photonics **4**(1), 24–26 (2010).

48. M. Rothschild, "Projection optical lithography," Mater. Today **8**(2), 18–24 (2005).

49. K. Jain, S. Rice, and B. J. Lin, "Ultrafast deep UV lithography using excimer lasers," Polym. Eng. Sci. **23**(18), 1019–1021 (1983).

50. A. Shilov, "TSMC Kicks Off Volume Production of 7nm Chips," https://www.anandtech.com/show/12677/tsmc-kicks-off-volume-production-of-7nm-chips.

51. S. Bajt, "Improved reflectance and stability of Mo-Si multilayers," Opt. Eng. **41**(8), 1797 (2002).

52. R. Soufli, S. Bajt, R. Hudyma, and J. Taylor, "Optics and Multilayer Coatings for EUVL Systems," in *LLNL-BOOK-403314* (2008).

53. H.-K. Cho and J. Ahn, "EUV Mask and Mask Metrology," EUV Lithogr. (May 2019), 325–381 (2009).

54. Y. Watanabe, K. Ota, H. Franken, and V. Banine, "No Title," in *Proceedings of the EUV Source Workshop* (International SEMATEC, Austin, 2005), p. 1.

55. M. van de Kerkhof, H. Jasper, L. Levasier, R. Peeters, R. van Es, J.-W. Bosker, A. Zdravkov, E. Lenderink, F. Evangelista, P. Broman, B. Bilski, and T. Last, "Enabling sub-10nm node lithography: presenting the NXE:3400B EUV scanner," Extrem. Ultrav. Lithogr. VIII **10143**(March), 101430D (2017).

56. S.-S. Kim, R. Chalykh, H. Kim, S. Lee, C. Park, M. Hwang, J.-O. Park, J. Park, H. Kim, J. Jeon, I. Kim, D. Lee, J. Na, J. Kim, S. Lee, H. Kim, and S.-W. Nam, "Progress in EUV lithography toward manufacturing," 1014306 (2017).

57. I. V. Fomenkov, "Laser produced plasma EUV sources for HVM 7nm node lithography: progress in availability and prospects of power scaling," 42 (2019).

58. A. Pirati, J. van Schoot, K. Troost, R. van Ballegoij, P. Krabbendam, J. Stoeldraijer, E. Loopstra, J. Benschop, J. Finders, H. Meiling, E. van Setten, N. Mika, J. Dredonx, U. Stamm, B. Kneer, B. Thuering, W. Kaiser, T. Heil, and S. Migura, "The future of EUV lithography: enabling Moore's Law in the next decade," Extrem. Ultrav. Lithogr. VIII **10143**(March), 101430G (2017).

59. E. van Setten, G. Bottiglieri, J. McNamara, J. van Schoot, K. Troost, J. Zekry, T. Fliervoet, S. Hsu, J. Zimmermann, M. Roesch, B. Bilski, and P. Graeupner, "High NA EUV lithography:

Next step in EUV imaging," **1095709**(March), 5 (2019).

60. S. Atzeni, "Introduction to Laser-Plasma Interaction and Its Applications," in *Atoms, Solids, and Plasmas in Super-Intense Laser Fields* (Springer, 2001), pp. 119–144.

61. I. C. E. Turcu and J. B. Dance, "X-rays from laser plasmas: generation and applications," X-Rays From Laser Plasmas Gener. Appl. by ICE Turcu, JB Danc. pp. 330. ISBN 0-471-98397-7. Wiley-VCH, Novemb. 1998. 330 (1998).

62. S. S. Harilal, "Influence of spot size on propagation dynamics of laser-produced tin plasma," J. Appl. Phys. **102**(12), (2007).

63. Y. Tao, M. S. Tillack, S. S. Harilal, B. O'Shay, F. Najmabadi, and K. L. Sequoia, "Effect of focal spot size on in-band 135 nm extreme ultraviolet emission from laser-produced Sn plasma," Opt. Lett. **31**(16), 2492 (2006).

64. J. Filevich, J. J. Rocca, E. Jankowska, E. C. Hammarsten, K. Kanizay, M. C. Marconi, S. J. Moon, and V. N. Shlyaptsev, "Two-dimensional effects in laser-created plasmas measured with soft-x-ray laser interferometry," Phys. Rev. E **67**(5), 56409 (2003).

65. A. Z. Giovannini and R. S. Abhari, "Three-dimensional extreme ultraviolet emission from a droplet-based laser-produced plasma," J. Appl. Phys. **114**(3), (2013).

66. Y. Shimada, H. Nishimura, M. Nakai, K. Hashimoto, M. Yamaura, Y. Tao, K. Shigemori, T. Okuno, K. Nishihara, T. Kawamura, A. Sunahara, T. Nishikawa, A. Sasaki, K. Nagai, T. Norimatsu, S. Fujioka, S. Uchida, N. Miyanaga, Y. Izawa, and C. Yamanaka,

"Characterization of extreme ultraviolet emission from laser-produced spherical tin plasma generated with multiple laser beams," Appl. Phys. Lett. **86**(5), 1–3 (2005).

67. K. Yoshida, S. Fujioka, T. Higashiguchi, T. Ugomori, N. Tanaka, H. Ohashi, M. Kawasaki, Y. Suzuki, C. Suzuki, K. Tomita, R. Hirose, T. Ejima, M. Nishikino, A. Sunahara, E. Scally, B. Li, T. Yanagida, H. Nishimura, H. Azechi, and G. O'Sullivan, "Efficient extreme ultraviolet emission from one-dimensional spherical plasmas produced by multiple lasers," Appl. Phys. Express **7**(8), (2014).

68. "The energy level diagram of an atom," https://www.learner.org/courses/chemistry/text/text.html?dis=U&num=Ym5WdElUQS9OU289&sec=YzJWaklUQS9OU289.

69. R. D'Arcy, H. Ohashi, S. Suda, H. Tanuma, S. Fujioka, H. Nishimura, K. Nishihara, C. Suzuki, T. Kato, F. Koike, J. White, and G. O'Sullivan, "Transitions and the effects of configuration interaction in the spectra of Sn XV-Sn XVIII," Phys. Rev. A - At. Mol. Opt. Phys. **79**(4), 1–7 (2009).

70. D. Salzmann, *Atomic Physics in Hot Plasmas* (Oxford University Press, 1998).

71. S. S. Harilal, C. V. Bindhu, R. C. Issac, V. P. N. Nampoori, and C. P. G. Vallabhan, "Electron density and temperature measurements in a laser produced carbon plasma," J. Appl. Phys. **82**(5), 2140–2146 (1997).

72. E. Asamoah and Y. Hongbing, "Influence of laser energy on the electron temperature of a laser-induced Mg plasma," Appl. Phys. B Lasers Opt. **123**(1), 1–6 (2017).

73. A. F. Molisch and B. P. Oehry, "Radiation trapping in atomic vapours," 510 (1998).

74. J. A. Koch, B. J. MacGowan, L. B. Da Silva, D. L. Matthews, J. H. Underwood, P. J. Batson, R. W. Lee, R. A. London, and S. Mrowka, "Experimental and theoretical investigation of neonlike selenium x-ray laser spectral linewidths and their variation with amplification," Phys. Rev. A **50**(2), 1877–1898 (1994).

75. R. Dinger, K. Rohr, and H. Weber, "Ion distribution in laser produced plasma on tantalum surfaces at low irradiances," J. Phys. D. Appl. Phys. **13**(12), 2301–2307 (1980).

76. Y. Tao, H. Nishimura, S. Fujioka, A. Sunahara, M. Nakai, T. Okuno, N. Ueda, N. Miyanaga, K. Nishihara, and Y. Izawa, "Characterization of density profile of laser-produced Sn plasma for 13.5nm extreme ultraviolet source," Appl. Phys. Lett. **86**(20), 201501 (2005).

77. S. Fujioka, H. Nishimura, T. Okuno, Y. Tao, N. Ueda, M. Murakami, T. Ando, Q. Gu, K. Nishihara, H. Kurayama, M. Yamaura, T. Norimatsu, H. Furukawa, N. Miyanaga, K. Nagai, Y. Yasuda, S. Uchida, Y.-G. Kang, Y. Shimada, Y. Izawa, and A. Sunahara, "Properties of EUV and particle generations from laser-irradiated solid- and low-density tin targets," in *Emerging Lithographic Technologies IX* (2005), **5751**(May 2005), p. 578.

78. O. Morris, F. O'Reilly, P. Dunne, and P. Hayden, "Angular emission and self-absorption studies of a tin laser produced plasma extreme ultraviolet source between 10 and 18 nm," Appl. Phys. Lett. **92**(23), 18–21 (2008).

79. S. Fujioka, H. Nishimura, K. Nishihara, A. Sasaki, A. Sunahara, T. Okuno, N. Ueda, T. Ando, Y. Tao, Y. Shimada, K. Hashimoto, M. Yamaura, K. Shigemori, M. Nakai, K. Nagai, T.

Norimatsu, T. Nishikawa, N. Miyanaga, Y. Izawa, and K. Mima, "Opacity effect on extreme ultraviolet radiation from laser-produced tin plasmas," Phys. Rev. Lett. **95**(23), 1–4 (2005).

80. J. R. Freeman, S. S. Harilal, and A. Hassanein, "Enhancements of extreme ultraviolet emission using prepulsed Sn laser-produced plasmas for advanced lithography applications," J. Appl. Phys. **110**(8), (2011).

81. S. S. Harilal, M. S. Tillack, Y. Tao, B. O'Shay, R. Paguio, and A. Nikroo, "Extreme-ultraviolet spectral purity and magnetic ion debris mitigation by use of low-density tin targets," Opt. Lett. **31**(10), 1549 (2006).

82. N. Böwering, M. Martins, W. N. Partlo, and I. V. Fomenkov, "Extreme ultraviolet emission spectra of highly ionized xenon and their comparison with model calculations," J. Appl. Phys. **95**(1), 16–23 (2004).

83. G. Schriever, K. Bergmann, and R. Lebert, "Extreme ultraviolet emission of laser-produced plasmas using a cryogenic xenon target," J. Vac. Sci. Technol. B Microelectron. Nanom. Struct. **17**(5), 2058 (2002).

84. F. Gilleron, M. Poirier, T. Blenski, M. Schmidt, and T. Ceccotti, "Emissive properties of xenon ions from a laser-produced plasma in the 100-140 Å spectral range: Atomic-physics analysis of the experimental data," J. Appl. Phys. **94**(3), 2086–2096 (2003).

85. S. A. George, M. Richardson, M. Al-Rabban, G. Shimkaveg, K. Takenoshita, C.-S. Koay, R. Bernath, H. Scott, and W. Silfvast, "EUV generation from lithium laser plasma for lithography," Emerg. Lithogr. Technol. X **6151**(March 2006), 615143 (2006).

86. J. Jonkers, "High power extreme ultra-violet (EUV) light sources for future lithography," Plasma Sources Sci. Technol. **15**, S8 (2006).

87. T. Ando, S. Fujioka, H. Nishimura, N. Ueda, K. Nagai, Y. Yasuda, K. Nishihara, T. Norimatsu, A. Sunahara, Y. Izawa, N. Miyanaga, K. Mima, and M. Murakami, "Optimum laser pulse duration for efficient extreme ultraviolet light generation from laser-produced tin plasmas," Appl. Phys. Lett. **89**(15), 151501 (2006).

88. R. Kodama, T. Mochizuki, K. A. Tanaka, and C. Yamanaka, "Enhancement of keV x-ray emission in laser-produced plasmas by a weak prepulse laser," Appl. Phys. Lett. **50**(12), 720–722 (1987).

89. T. Higashiguchi, N. Dojyo, M. Hamada, W. Sasaki, and S. Kubodera, "Low-debris, efficient laser-produced plasma extreme ultraviolet source by use of a regenerative liquid microjet target containing tin dioxide (SnO2) nanoparticles," Appl. Phys. Lett. **88**(20), 201503 (2006).

90. J. Fujimoto, T. Hori, T. Yanagida, and H. Mizoguchi, "Development of laser-produced tin plasma-based EUV light source technology for HVM EUV lithography," Phys. Res. Int. **2012**(1), (2012).

91. J. Fujimoto, T. Hori, T. Yanagida, T. Ohta, Y. Kawasuji, Y. Shiraishi, T. Abe, and T. Kodama, "Development of laser-produced plasma based EUV light source technology for HVM EUV lithography," in *Extreme Ultraviolet (EUV) Lithography III* (2012), **8322 of Pr**, pp. 1–13.

92. D. S. KUZNETSOV, A. E. YAKSHIN, J. M. STURM, R. W. E. VAN DE KRUIJS, E. LOUIS, and F.

BIJKERK, "High-reflectance La / B-based multilayer mirror for 6 . x nm wavelength," Opt. Lett. **40**(16), 3778–3781 (2015).

93. D. Kilbane and G. O'Sullivan, "Extreme ultraviolet emission spectra of Gd and Tb ions," J. Appl. Phys. **108**(10), 1–6 (2010).

94. T. Higashiguchi, B. Li, Y. Suzuki, M. Kawasaki, H. Ohashi, S. Torii, D. Nakamura, A. Takahashi, T. Okada, W. Jiang, T. Miura, A. Endo, P. Dunne, G. O'Sullivan, and T. Makimura, "Characteristics of extreme ultraviolet emission from mid-infrared laser-produced rare-earth Gd plasmas," Opt. Express **21**(26), 31837 (2013).

95. T. Otsuka, D. Kilbane, T. Higashiguchi, N. Yugami, T. Yatagai, W. Jiang, A. Endo, P. Dunne, and G. O'Sullivan, "Systematic investigation of self-absorption and conversion efficiency of 6.7 nm extreme ultraviolet sources," Appl. Phys. Lett. **97**(23), 2008–2011 (2010).

96. S. S. Churilov, R. R. Kildiyarova, A. N. Ryabtsev, and S. V Sadovsky, "EUV spectra of Gd and Tb ions excited in laser-produced and vacuum spark plasmas," Phys. Scr. **80**(4), 2–8 (2009).

Chapter 2 Pulse Shape Dependence of the EUV Emission from a Sn Laser-Produced-Plasma Using Temporally-Synthesized Irradiation Pulses

2.1 Introduction

After decades of development, Extreme Ultraviolet (EUV) lithography based on Sn laser-produced plasma (LPP) emitting at wavelengths near 13.5 nm [1–8] has been advanced to meet that demands of high volume manufacturing (HVM) of integrated circuits. A requirement for achieving HVM is the generation of sufficient EUV power, which, over the past decades, has increased by more than a factor of 20 [6]. However, additional increases in EUV power are still desired to increase wafer throughput. In addition to employing more powerful driver lasers, these further increases depend on the optimization of the conversion efficiency (CE) on laser energy into in-band EUV radiation. Here we report the results of the study of the CE dependence of a Sn LPP on laser pulse shape. The experiments were conducted irradiating flat Sn solid targets with pulses of different shapes generated by an innovative pulse synthesizer.

EUV CE is defined here as the ratio of EUV energy radiated into 2π space within a 2% bandwidth near the central wavelength of 13.5nm to the energy of the excitation laser pulse that is employed to create the plasma. Different methods have been explored to increase the CE of Sn LPP. Previous works have investigated the CE dependence on the laser wavelength [9,10], the

duration of excitation laser pulse [9,11–13], the initial density of the target [14,15], the target geometry [16,17], the focal spot size [13], and the laser energy deposition history by the addition of a pre-pulse preceding the main excitation laser pulse [18,19]. In particular, the use of the pre-pulse technique has made it possible to achieve a significant increase in the CE of Sn LPP [4]. In this work, we study another variable: the laser pulse shape. To generate pulses of arbitrary shape, a pulse synthesizer based on a cryogenic Yb: YAG laser system was implemented. Different pulse synthesizing techniques have been reported previously. In refs [20] and [21] femtosecond pulses of arbitrary shapes were generated using spectral filtering in a temporally nondispersive grating set up for applications such as optical communications and spectroscopy. However, femtosecond pulse durations are not optimal for the efficient generation of EUV emission from a Sn LPP. In reference [22] birefringent prisms were used to split an incident beam into four replicas and form a flat top pulse with a pulse duration of one hundred picoseconds by recombining the replicas with appropriate delays for the purpose of pumping an optical parametric amplification system. The configuration and operation of the pulse synthesizer used to conduct the present work are summarized in Section II. Although the primary technique for EUV generation is irradiating Sn droplets with CO_2 at λ=10.6 μm, in this investigation we studied the influence of the pulse shape on the EUV emission from a plasma created by focusing a λ=1.03 μm laser onto a slab Sn target. The concept of pulse shaping approach could be adapted to λ=10.6 um, droplet targets, and other Sn LPP configurations of interest. Since it makes sense to investigate the influence of pulse shape in the vicinity of the optimum conditions for maximum CE, we scanned a multi-dimensional parameter space to find such conditions. Scans were

conducted as a function of laser intensity, the key parameter influencing the plasma temperature, pulse length, and focal spot size,

2.2 Experimental setup

The experiments were conducted by introducing a pulse synthesizer into a chirped pulse amplification chain of a diode-pumped Yb: YAG laser, as shown in Figure 2-1 (a). The front end of the laser system consists of a mode-locked oscillator, a pulse stretcher, and a regenerative amplifier. The details of the front end of this laser are described in ref [23]. The regenerative amplifier can be operated in two different modes: Q-switched / cavity-dumped mode or injection seeded. When operated in Q-switched / cavity-dumped mode, it can output pulses with a duration of several nanoseconds depending on the width of the window of the Pockels cell after the regenerative amplifier. When operated in seeded mode, it can output pulses with a duration of several hundreds of picoseconds depending on the configuration of the grating stretcher. For the results here, the stretched pulses had a duration of 300 ps FWHM, after gain narrowing in the power amplifier. In order to generate synthesized pulses of arbitrary shapes, a pulse synthesizer is introduced after the regenerative amplifier, as shown in Figure 2-1 (a). A schematic diagram of the pulse synthesizer is shown in Figure 2-1 (b). First, the output pulse of the regenerative amplifier is spatially expanded 100 times in the horizontal direction using a cylindrical telescope. Subsequently, the spatially expanded pulse is split into 10 channels, each associated with a sub-pulse. Each sub-pulse passes through a liquid crystal phase retarder and is then reflected back by a retro-reflector. The reflected sub-pulses return through the liquid crystal

phase retarders and the cylindrical telescope. Finally, the sub-pulses merge and are extracted by a cube polarizer. The intensity of each sub-pulse can be adjusted when the voltage on each liquid crystal is controlled in real-time using a control program. The retro-reflectors are mounted on rails such that the distance between any two retro-reflectors can be changed, thereby controlling the inter-pulse temporal separation. When the sub-pulses are spread out evenly, the temporal separation between any two adjacent sub-pulses can be changed from 0 to ~1ns, resulting in a total pulse duration of up to 9.3 ns. When combined with a pulse compressor, this synthesize allows for the production of arbitrary sequences of sub-10 picosecond-duration pulses. For the experiments reported here, the output was not compressed, allowing for the tailoring of nanosecond duration pulses with a resolution of a few hundred picoseconds. The capability of adjusting the intensity of each sub-pulse and the distance between any two retro-reflectors makes it possible to form any shape of synthesized pulse and to introduce an arbitrary sequence of pulses. A program is used to control the shape of the pulse in real-time by monitoring the output pulse of the laser system and automatically changing the voltages on the liquid crystal phase retarders to achieve the designed pulse shape.

After being extracted by the cube polarizer, the sequence of sub-pulses is sent into a second regenerative amplifier to regain the energy necessary to operate the subsequent power amplifiers near saturation. The energy of the synthesized pulse is increased to 100 mJ by a cryogenically cooled diode-pumped Yb: YAG multi-pass amplifier operating at λ=1.03 μm [24]. Examples of synthesized pulses are illustrated in Figure 2-2. These pulse traces demonstrate the capability of generating a sequence of pulses separated by hundreds of picoseconds to form arbitrary intensity contours which we are calling synthesized pulses. It should be noted that here

the duration of a synthesized pulse is measured from the half maximum of the rising edge of the leading sub-pulse to the half maximum of the falling edge of the trailing sub-pulse, and the pulse duration of a Q-switched or seeded pulse is measured at its FWHM value.

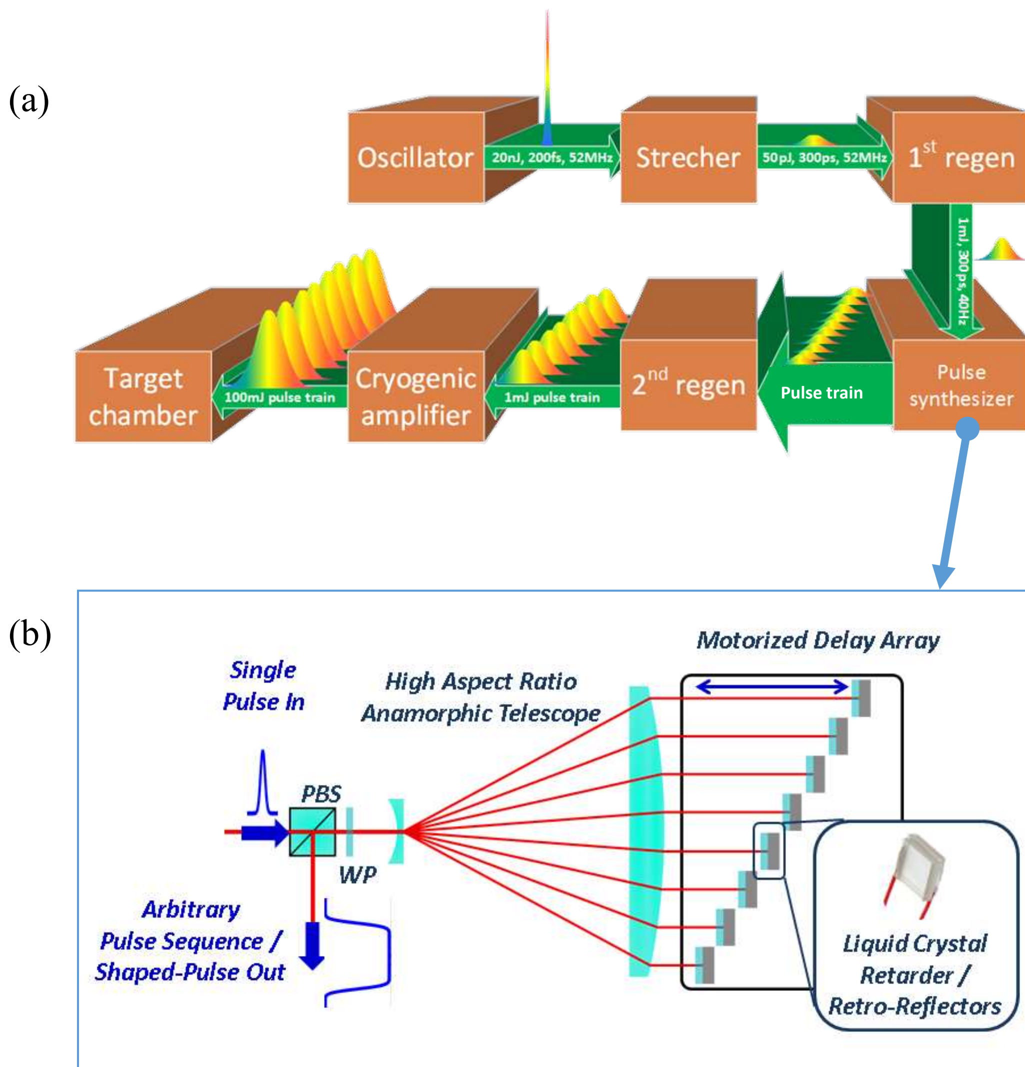

Figure 2-1. (a) Block diagram of the laser pulse synthesizer system. The sub-pulses in the pulse train that are generated by the pulse synthesizer are made co-linear after being amplified by the second regenerative amplifier. In the diagram, the sub-pulses are deliberately displaced in the horizontal direction for visual clarity. (b) Schematic of the pulse synthesizer.

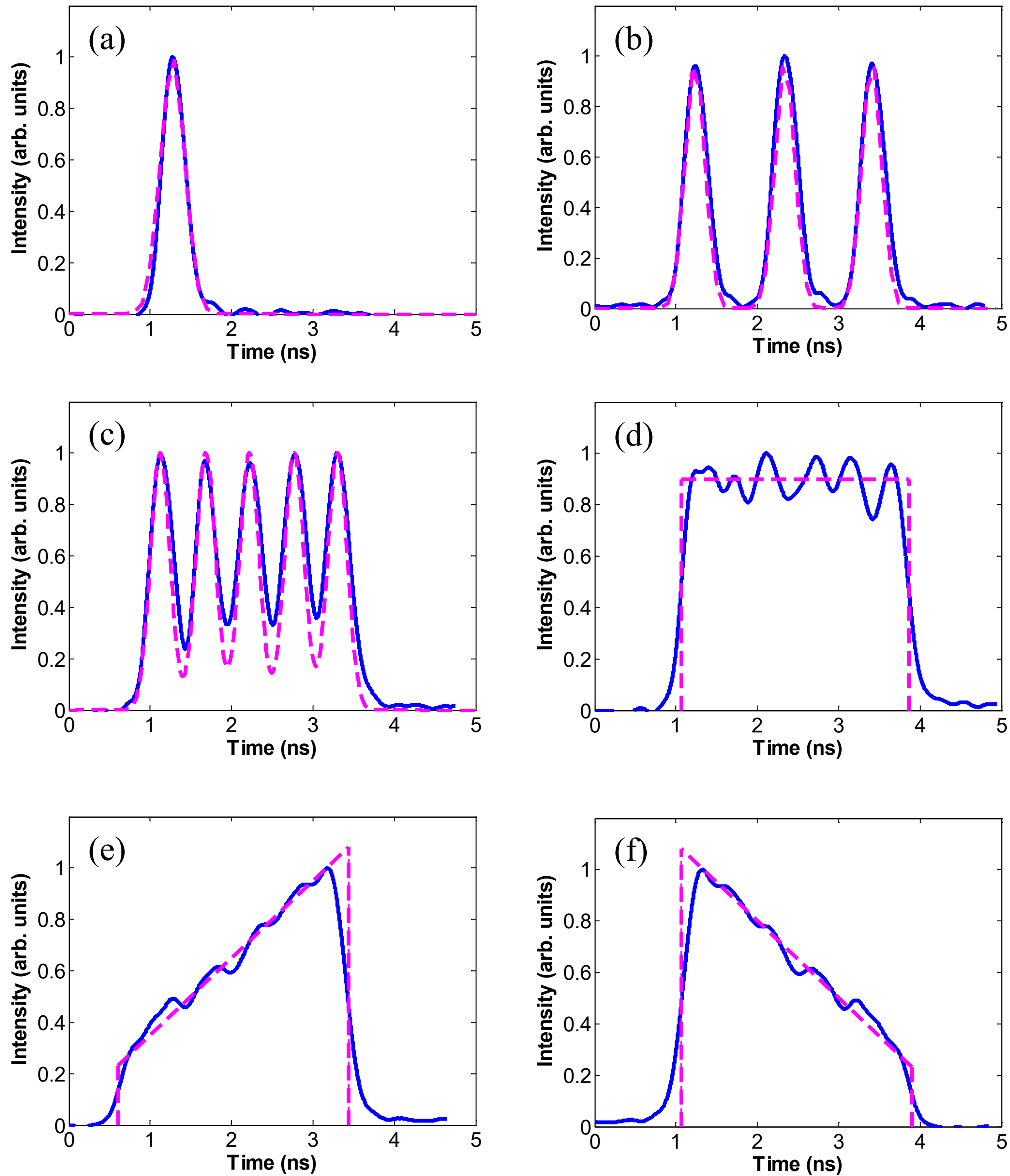

Figure 2-2. Examples of synthesized pulses: The dashed traces are the designed shapes, and the blue traces are the measured synthesized pulses. The input pulses into the synthesizer have a pulse duration of 300 ps FWHM. In order to form different pulse shapes, number of one (a), three (b), five (c), ten (d, e, f) channels are used, and the voltages applied to the liquid crystals phase retarders are adjusted to form square (d), up-ramp (e) and down-ramp (f) shapes.

The amplified synthesized pulses are focused onto a polished Sn slab target to generate the plasmas. The spot focus diameter was adjusted from 100 μm to 200 μm by using lenses with

different focal lengths. The Sn LPP emission was characterized using a EUV diagnosis suite, which is similar to that used in ref. [25], but adapted for operation at 13.5 nm and expanded to include the capability of time-resolved measurements. The energy of emitted EUV radiation was measured by three energy monitors that are positioned in the same horizontal plane that contains the Sn LPP and the irradiation laser at angles of 6°, 46°, and 86° with respect to the target normal. The EUV pulse energy monitors consist of an EUV-sensitive photodiode, a Mo/Si mirror, and a 0.3 μm thick Zr thin film filter. The total wavelength-resolved responsivity of each energy monitor near λ=13.5 nm was calibrated at the Advanced Light Source synchrotron [26]. The combination of Zr filters and multilayer Mo/Si mirrors makes it possible to detect only the in-band 13.5nm EUV emission. The spectral emission was measured using a flat-field grazing-incidence spectrometer consisting of a variable-line-spacing diffraction grating with a nominal ruling of 1200 lines/mm and a back-illuminated CCD detector. The measured spectral emission wavelength was calibrated using the 2p→ 1s transition line of Li^{3+} at λ=13.5nm and the absorption edge of silicon at λ=12.5nm. For the first calibration, LiOH powder was spread over the Sn target to generate emission from the same plane, and for the second a 100 nm thick silicon filter was used.

The time-resolved EUV emission was measured by using a Mo/Si concave mirror to reflect and focus EUV emission from the Sn LPP onto a fast EUV silicon photodiode. A digitizing oscilloscope with 1.5 GHz analog bandwidth was employed to record the signal. The impulse response of the entire photodiode-based detecting system was calibrated using the ultrashort duration pulses from an 18.9 nm Ni-like Mo EUV laser [27]. The duration of the pulses of this type of plasma-based laser is ~ 5 ps [28] that for practical purposes is a delta function with respect to the time

scale of interest here. The recorded 10% - 90% rise time of the entire detection system was measured to be 0.89 ns. A Zr filter was placed in front of the fast EUV photodiode to block IR and visible light from reaching the photodiode. In addition, we used an EUV imaging system to monitor the size of EUV emitting region of the plasma from both normal and tangential directions. Magnified images of the in-band plasma emission were obtained using a concave Mo/Si multilayer mirror with a radius of curvature of 0.25 meters and a EUV-sensitive CCD. The magnification factor used was 12x and 14x for normal and tangential directions, respectively.

2.3 Experimental results

2.3.1 Angular distribution of the EUV emission

The angular distribution of the EUV emission shown in Figure 2-3 was obtained using an array of three energy-monitors placed at different angles. The total EUV yield was obtained by fitting the measured emission angular distribution with a 2nd order polynomial and integrating this distribution over a solid angle of 2π, assuming the EUV emission is symmetric about the central axis of the Sn LPP. The laser irradiation parameters, including the pulse shape, pulse energy, and focal spot size, were scanned when measuring the angular distribution of the EUV emission. This allowed us to determine the CE more accurately than assuming an isotropic distribution, as done in previous measurements [14,16]. Figure 2-3 (a) shows a comparison of the angular profiles of EUV emission for different laser pulse shapes while the 80 mJ laser pulse energy and 150 µm focal spot diameters remained constant. In Figure 2-3 (b) each angular intensity distribution is normalized to the same maximum to facilitate comparison. The EUV emission is observed to

decrease as a function of angle with respect to the target normal, which is in agreement with previous studies of Sn LPP [29]. Additionally, the angular profile of the EUV emission corresponding to the synthesized square pulse is observed to be flatter than the angular profiles corresponding to the other pulse shapes. This more homogeneous angular distribution of the EUV emission results from the temporally constant irradiation flux that creates a more homogeneous LPP of greater radial extent, with more uniform temperature and more homogeneous dynamic Doppler effect and optical depth.

2.3.2 CE as a function of laser fluence for different pulse shapes

The CE of the Sn LPPs was measured as a function of laser fluence for different pulse shapes. The spectral distribution corresponding to different pulse shapes and pre-pulse sequences were analyzed. Here we limit the discussion to several distinct pulses designed to have different rise times and pulse shapes, including a Q-switched pulse, a synthesized square pulse, a synthesized up-ramp pulse, and a synthesized down-ramp pulse. The Q-switched pulse has a pulse duration of ~ 3ns FWHM. The synthesized pulses have a pulse duration of 3ns, which is measured from the half maximum of the rising edge of the leading sub-pulse to the half maximum of the falling edge of the trailing sub-pulse. It was found that the Q-switched pulse yields a CE of ~ 2.0 % which is in general agreement with previous works using λ=1 μm laser and flat solid Sn targets [10,16]. As shown in Figure 2-4, the synthesized square pulse yields a CE of 2.7%, which is 35% higher than the CE of the Q-switched pulse. The synthesized up-ramp and down-ramp pulse yield a similar CE of ~2.4%, which is slightly lower than the CE of the synthesized square pulse. The experimental results match well with simulations conducted using the transient hydrodynamic /

atomics physics model Radex [30–33]. The simulations indicate that the ratio of optimal CE corresponding to synthesized square pulse, synthesized up-ramp pulse, and synthesized down-ramp pulse is 1:0.83:0.76.

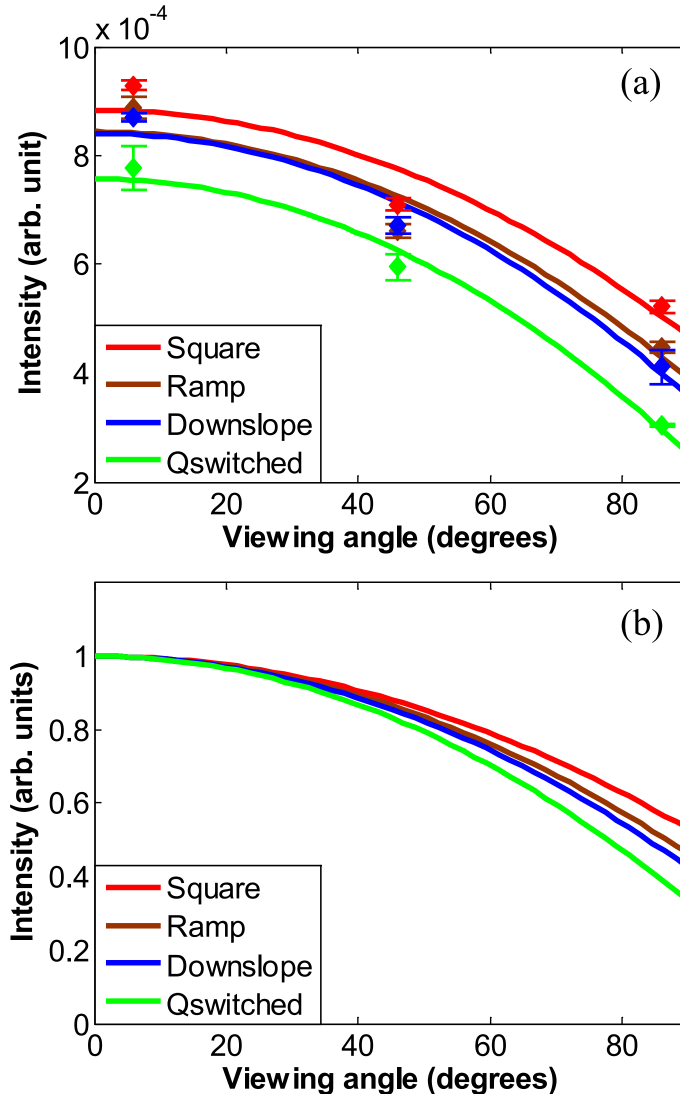

Figure 2-3. (a) Measured EUV emission intensity at angles of 6°, 46°, 86° with respect to the normal of the target surface and the fitted angular profiles of EUV emission for Sn LPP created using different laser pulse shapes: square (red), up-ramp (brown), down-ramp (blue), and Q-switched (green). A laser pulse energy of 80 mJ laser pulse and 150 µm focal spot diameter remained constant. (b) Normalized angular profiles of the EUV emission.

For the synthesized square pulse, the optimal CE occurs at a laser fluence of ~2.5×10^2 J/cm^2 in the experiment, corresponding to a laser intensity of ~ 9.0×10^{10} W/cm^2. The reason why the

synthesized square pulse yields the highest CE is attributed to the fact after a fast rise the pulse intensity reaches a flat top with the optimum value to generate in-band 13.5 nm radiation, making more efficient use of the laser pump energy. In contrast, the other pulse shapes only reach the optimum excitation for a short duration.

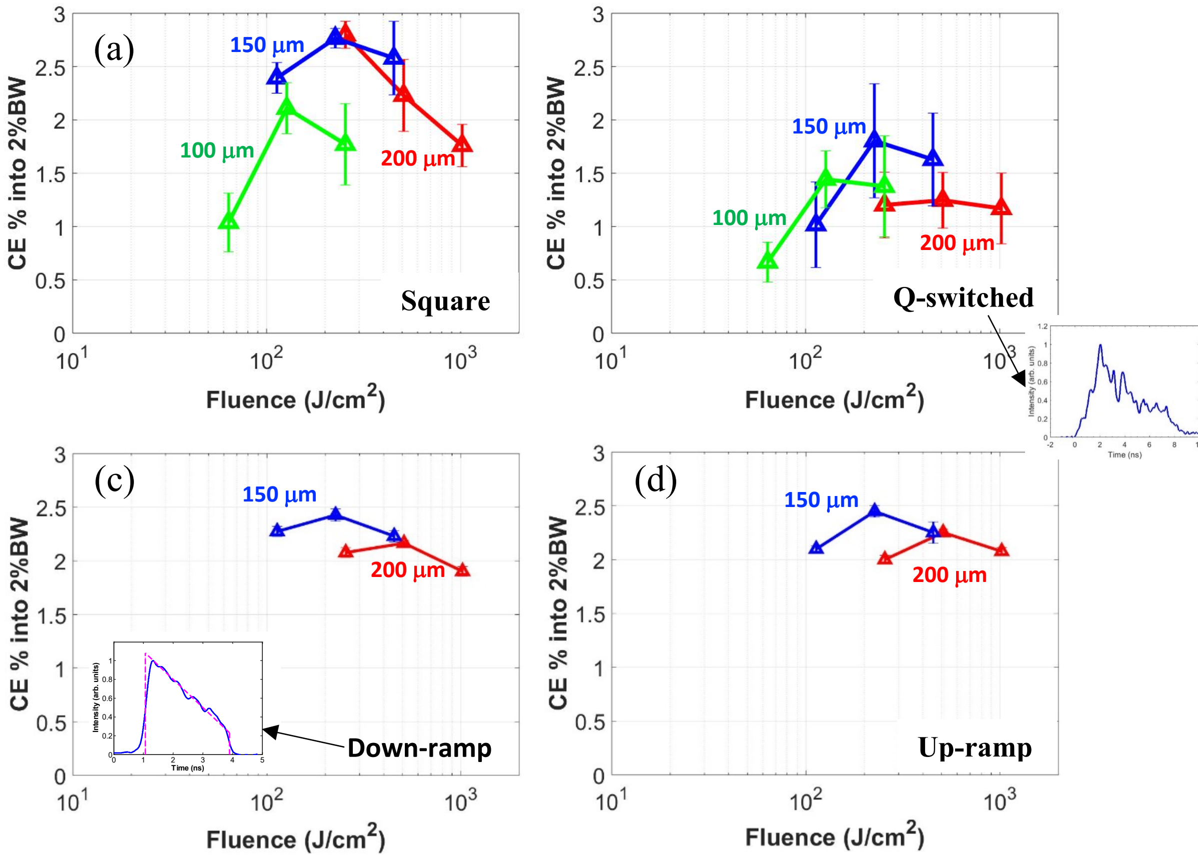

Figure 2-4. CE as a function of irradiation fluence for different laser pulse shapes (a) Synthesized square pulse (b) Q-switched pulse, (c) Synthetized down-ramp pulse, (d) Synthetized up-ramp pulse. For each pulse shape, three focal spot sizes are used, including 100 μm (green), 150 μm (blue), and 200 μm (red). And for each focal spot size, three pulse energies are used, including 20mJ, 40mJ and 80mJ. A typical Q-switched pulse shape is inserted in (b), and the Q-switched pulse has a pulse width (FWHM) of ~3ns although it has a long tail.

The CE is sensitive to the pulse duration of the square pulse, in particular when the pulse is shorter than 1.5 ns. As shown in Figure 2-5, the EUV CE increases with pulse duration up to 4 ns. The simulations show that the CE will continue to grow until quasi-stationary conditions of

plasma flow are reached at pulse durations of 6-8 ns. Using our current 10 channels set up illustrated in Figure 2-1 (b) the synthesized square pulse cannot be extended further. This is because increasing pulse durations requires increased separation between the sub-pulses that introduces an increased intensity modulation that was found to be detrimental to the CE. For example, the CE generated using synthesized square pulse decreases from 2.7% to 2.0% when the temporal separation between sub-pulses increases from 0.4ns to 1.0ns, causing the intensity modulation to increase from 42% to 100 %.

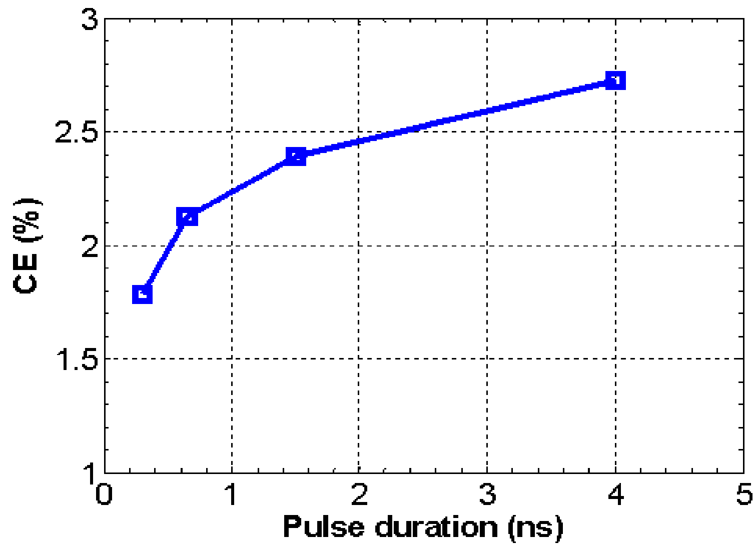

Figure 2-5. CE of Sn LPP for 2% bandwidth centered at 13.5 nm as a function of pulse duration of synthesized square pulse. The laser pulse energy is 80mJ, and the spot size is 150 μm.

2.3.3 Spectroscopic characterization of the EUV emission

The in-band EUV spectra of the Sn LPP were observed under the different irradiation conditions. The emission was recorded at 60° from the target normal using the EUV spectrometer described above. The spectral emission generated using four different pulse shapes including a synthesized

square pulse (3ns), a synthesized ramp pulse (3ns), a Q-switched pulse (3ns), and a single 300ps FWHM duration pulse are shown in Figure 2-6. Firstly, we observed that the peak intensity of the spectrum of the plasma created using synthesized a square pulse is the highest among all of the pulse shapes, in accordance with the CE measurements. For the Sn LPPs generated using Q-switched pulse, synthesized square pulse, and synthesized up-ramp pulse, corresponding to pulse energy of 80mJ and focal spot size of 150 μm, the peak intensities all fall near 13.5nm and the normalized spectral emission profiles practically overlap, as shown in Figure 2-6 (a) and (b). However, the spectral emission of the plasma generated using the 300 ps pulse is broader and shifted to longer wavelength, because this plasma has a broader range of ion charge states and has the highest mean ionization state among the pulse shapes [25]. This happens as a result of maintaining the laser pulse energy constant for all pulse durations. The shorter laser pulses correspond to higher intensities leads to higher peak temperatures and results in a larger spread of ion charges due to the transient property of ionization. Secondly, we investigated the influence of focal spot size on the spectral emission of Sn LPP. The peak intensity of the spectral emission of the plasmas created using 150um diameter focal spot is the highest among all the focal spot sizes (100μm, 150μm, and 200μm) as shown in Figure 2-6 (c). The reason is probably because the Sn plasma corresponding to 150 μm has the highest abundance of the Sn ion species which emit around λ=13.5 nm. Although the peak wavelength shift between different focal spot sizes is very small, the spectral emission of Sn LPP generated using 150 μm spot is narrower than those generated using the other two focal spot sizes. Narrower spectral emission results in a better overlap between the spectral emission and the reflectivity band of the sequence of Mo/Si

mirrors used for EUV projection lithography which is generally much narrower than the spectral emission from the Sn LPP [34].

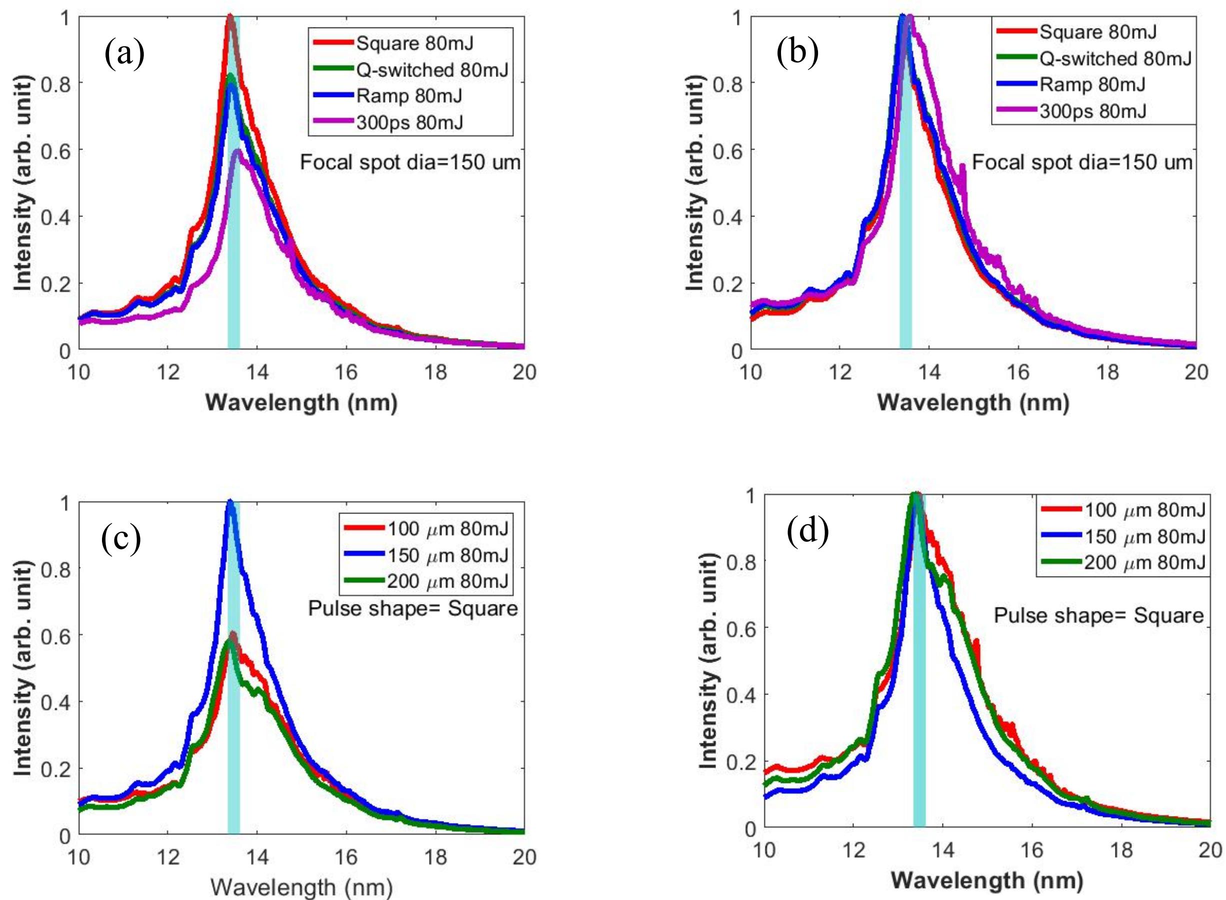

Figure 2-6. As measured (a) and normalized (b) spectral emissions of Sn LPP generated corresponding to synthesized square (red), Q-switched pulse (green), synthesized ramp pulses (blue) and single pulse (purple) and keeping the pulse energy of 80mJ and focal spot size of 150 μm. The measured (c) and normalized (d) spectral emissions of Sn LPP generated for focal spot sizes of 100 μm (red), 150 μm (blue), and 200 μm (green), keeping the pulse shape as synthesized square pulse and keeping the pulse energy as 80mJ.

As the focal spot size increases, resonance line reabsorption also becomes more significant [35]. Model simulations indicate that somewhat larger spot diameters would be beneficial for larger CE due to an increase of plasma lifetime respect to the radiative cooling time. However, the required optimum laser pulse energy would be outside the range of the laser used in these experiments. Additionally, a broad range of irradiation intensities was scanned to investigate

variations in the spectrum. The wavelength corresponding to the peak intensity for different pulse shapes, focal spot sizes, and pulse energies are shown in Figure 2-7. This “V” shape trend was reported by a previous theoretical study [36]. The peak intensity wavelength of the spectral emission of Sn LPP is observed to first shift to shorter wavelength with increased irradiation intensity ($<10^{11}$W/cm^2) as the mean degree of ionization reaches the Sn^{14+}. When the irradiation intensity is further increased, the trend reverses and the wavelength shifts to longer wavelength. This red-shift is due to the increased splitting of n=4 ground state when the Sn ion is ionized from the closed-shell Kr-like ionization state to higher ionization states.

2.3.4 Time-resolved EUV emission

We also performed time-resolved measurements of the EUV in-band emission at different angles. In this study, the Sn LPPs were created by focusing synthesized square pulses of 3 ns duration into 150 µm FWHM focal spots and varying the pulse energy from 20mJ to 80mJ. A concave Mo/Si mirror was positioned at 15° or 82° with respect to the normal of the target surface to collect in-band EUV emission and focus it onto a fast silicon photodiode. The duration of the EUV emission at 15° (Figure 2-8 (a)) is observed to increase with laser pulse energy. When the measured time evolution of the EUV emission is deconvolved from the impulse response of the detection system, the lifetime of the EUV emission (FWHM) observed at 15° is 3.7ns, 5.5ns, and 8.1ns for pulse energies of 20mJ, 40mJ and 80mJ respectively. The conclusion is that the EUV emission at this angle increases as a function of laser pulse intensity and outlasts the duration of the laser excitation pulse by up to almost three times when 80 mJ pulses are used to generate the Sn LPP.

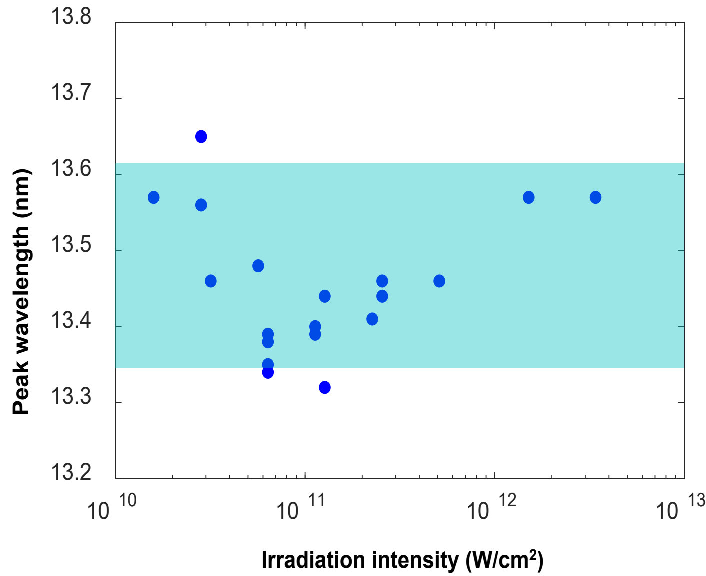

Figure 2-7. EUV peak emission wavelength as a function of irradiation intensity. The shadow represents the reflectivity band of the Mo/Si mirror.

In contrast, the lifetime of the EUV emission observed at 82° remains relatively constant and similar to the laser pulse duration: 2.9ns, 3.3ns and 3.7ns (FWHM) for pulse energies of 20mJ, 40mJ and 80mJ respectively Figure 2-8 (b)). The time-resolved EUV emission was also simulated using a transient hydrodynamic / atomics physics model and was convolved with the impulse response of the detection system in order to compare it with the measured EUV emission. Figure 2-8 (c)-(e) shows a good agreement between the computed and measured emission at 82° for all three pulse energies. In the direction of the target normal, where the maximum velocity gradients exist, the opacity is decreased by the dynamic Doppler effect that shifts the center wavelength of the lines, facilitating the emission [37]. The emission from an optically thin plasma would be isotropic because each emitter would contribute equally in all directions. However, in this case, the plasma is substantially optically thick. In the direction of the target normal, the decrease in emissivity as the plasma expands is compensated by the nearly quadratic increase of

the emitting surface, and the increase in plasma effective emitting depth. As a result, the plasma continues to emit as it expands after the laser pulse ends. In the case of observation along the surface, where the plasma is also optically thick, the increase of the emitting surface area is weaker and approximately linear. Consequently, in this direction, the decrease in emissivity with decreasing temperature and density is not compensated by the increase in source size. As a result, the emitted EUV power in this direction ends as the laser intensity decreases. In summary, the observed strong dependence of the duration of the EUV emission as a function of angle is likely to be the result of the combined effects of the large optical depth of the resonance lines and the different scaling with time of the EUV emitting area in the directions normal and parallel to the target surface after the laser pulse ends. Another possible contributing cause to the EUV pulse duration anisotropy is the creation of a cold plasma in the periphery of the irradiated spot at late times, which can absorb the EUV radiation and influence the hydrodynamic. The generation of such peripheral plasma driven by plasma radiation has been previously detected using soft x-ray laser interferometry [38].

In order to further investigate the dynamics of the EUV emission, we designed a double pulse sequence, as shown in Figure 2-9. We first irradiated the Sn target using a 300ps, 40 mJ laser pulse. After a selected delay ranging from 0ns to 5ns, we sent a second 300ps laser pulse of equal energy to re-heat the Sn LPP.

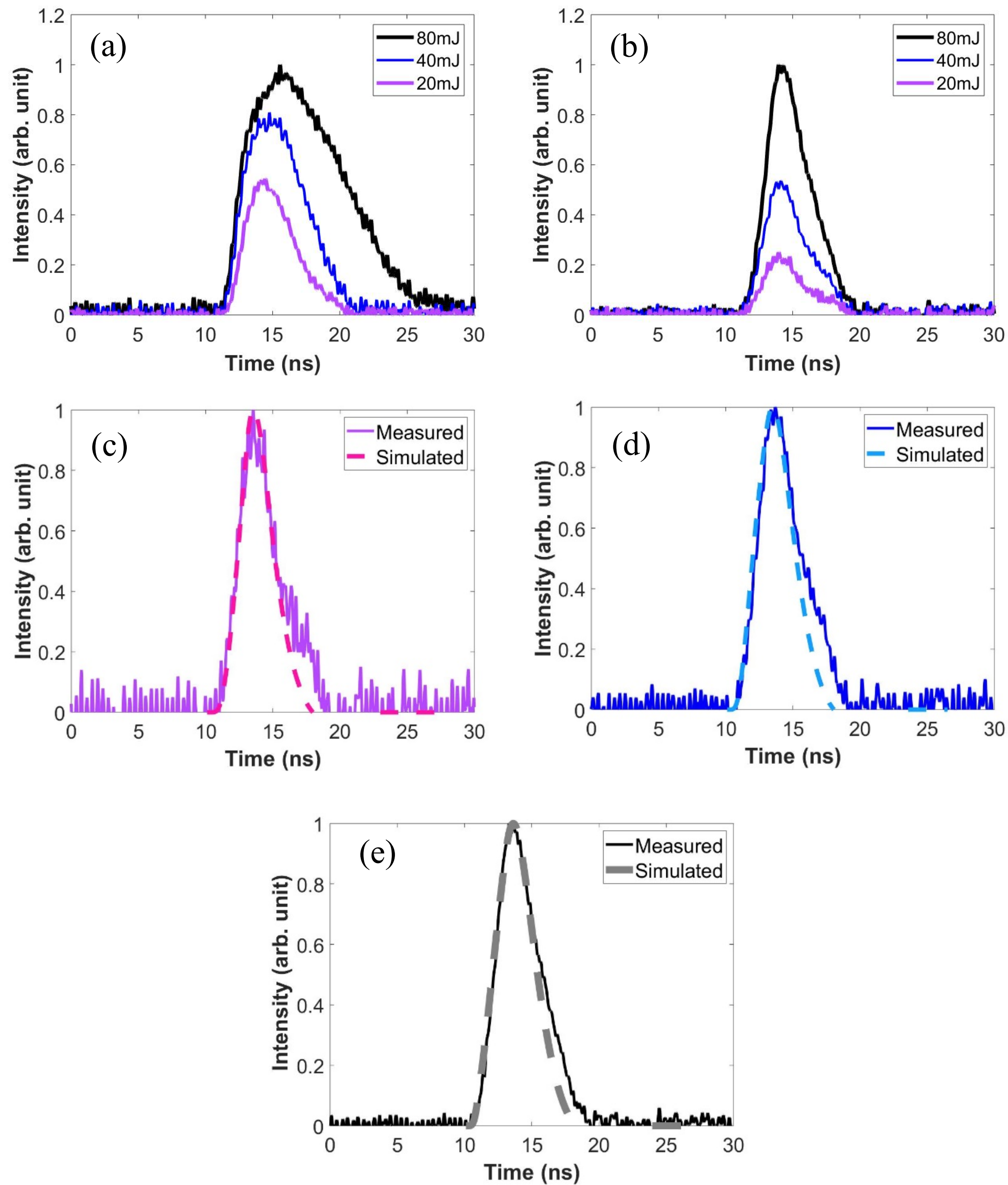

Figure 2-8. (a) and (b): Time-resolved EUV emission, from Sn LPP created using 3ns square pulse and 150 μm diameter focal spot, observed at 15° (a) and 82° (b) with respect to the target normal. The pulse energy varies from 20mJ to 80mJ. (c)-(e): Comparison of the measured and simulated time-resolved EUV emissions for Sn LPP created red at 82° from the target normal. The pulse energy is 20mJ (c), 40mJ (d) and 80mJ (e). The irradiation corresponds to 3ns square pulses, focused into 150 μm diameter spot.

As expected, the lifetime of the EUV emission increased with the temporal separation between the two pulses, but the intensity of EUV emission decreased. As a result, the integrated EUV emission remained almost the same, independent of the pulse separation. This appears to indicate the re-heating of the plasma with delayed laser pulses to increase the duration of the EUV emission does not appear to be a straightforward way to improve CE. The plasma corresponding to 0 ns temporal delay was excited with a single pulse with energy equal to the sum of the two pulses. The EUV yield was observed to be lower than that corresponding to the other temporal delays because in this case the irradiation intensity is too high, and the Sn plasma is overionized.

2.3.5 EUV-emitting source size

The dependence of EUV-emitting source size on irradiation parameters, including pulse duration, focal spot size, and pulse energy, and pulse shape, was studied by acquiring in-band EUV images of the plasmas. Figure 2-10 (a) shows in-band EUV images observed along the target normal direction for plasmas created using the synthesized square pulses. The time-integrated size of the EUV emitting plasma region is observed to be similar to the laser focal spot size and to slightly increase with laser pulse energy. The EUV source size is not particularly sensitive to pulse shape (not shown in Figure 2-10). In-band EUV images were also recorded in the tangential direction. Figure 2-10 (b) shows EUV images taken along the surface for plasmas created using synthesized square pulse and different pulse energies focal spot sizes.

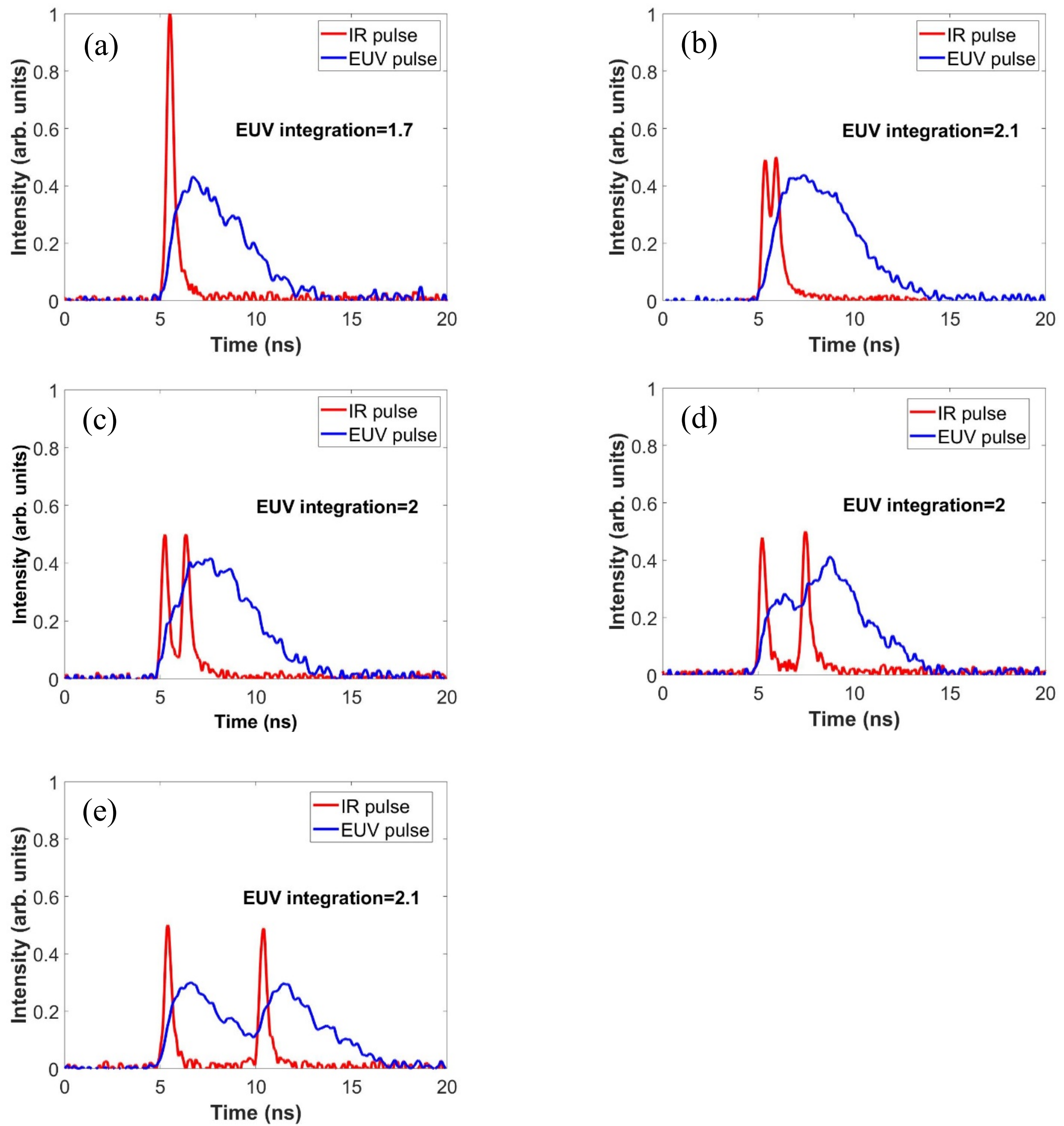

Figure 2-9. The time-resolved EUV emission from Sn LPP created using two 300 ps laser pulses temporally separated by (a) 0 ns, (b) 0.6 ns, (c) 1.1 ns, (d) 2.3 ns and (e) 5 ns.

The expected increased EUV-emitting volume with laser pulse duration, theoretically discussed in reference [11], is observed in Figure 2-10 (c). This figure shows the increase of the EUV emitting region with pulse duration for synthesized square pulses of 300ps, 1.5ns, and 3ns

duration. The data was obtained keeping the laser pulse energy and focal spot size constant at 40 mJ and 150 μm, respectively. The simulation results shown in Figure 2-11 are obtained using the code Radex and illustrate how the increased pulse duration results in an increase in the EUV emitting plasma volume, by comparing the electron temperature and electron density distribution for plasmas produced by 300 ps and 3 ns pulses. Figure 2-11 (a) and (b) shows that the Sn LPP created using 3ns synthesized square pulse results in a significantly larger plasma region heated to the necessary electron temperature for EUV emission. Figure 2-11 (c), (d) show that the electron density profiles for the two pulse durations are not very different. The wider high-temperature region in both the spatial and temporal domains results in increased EUV emission and in the improvement in CE with increased laser pulse duration illustrated in Figure 2-5.

2.4 Summary

In conclusion, we have studied the dependence of the 13.5 nm EUV emission from LPPs generated irradiating solid Sn targets with λ=1.03 μm laser pulses on laser pulse shape and other irradiation parameters. Measurements were conducted focusing synthesized pulses of different shape, duration, and energy from a single Yb: YAG laser onto slab Sn targets. The measured CE of ~ 2 % for Q-switched pulses is consistent with the values reported from previous work in which slab Sn targets were irradiated with λ=1 μm pulses [12,14]. Synthesized square pulses were observed to yield the highest CE (2.7%) among all the pulse shapes studied. The synthesized square pulse CE was ~ 35% higher than that corresponding to Q-switched pulse. The CE was also

measured to increase with pulse duration up to the maximum pulse length investigated, 4 ns. A long-lasting square pulse has the advantage of maintaining for the longest time the pre-selected optimum irradiation conditions, leading to maximum CE.

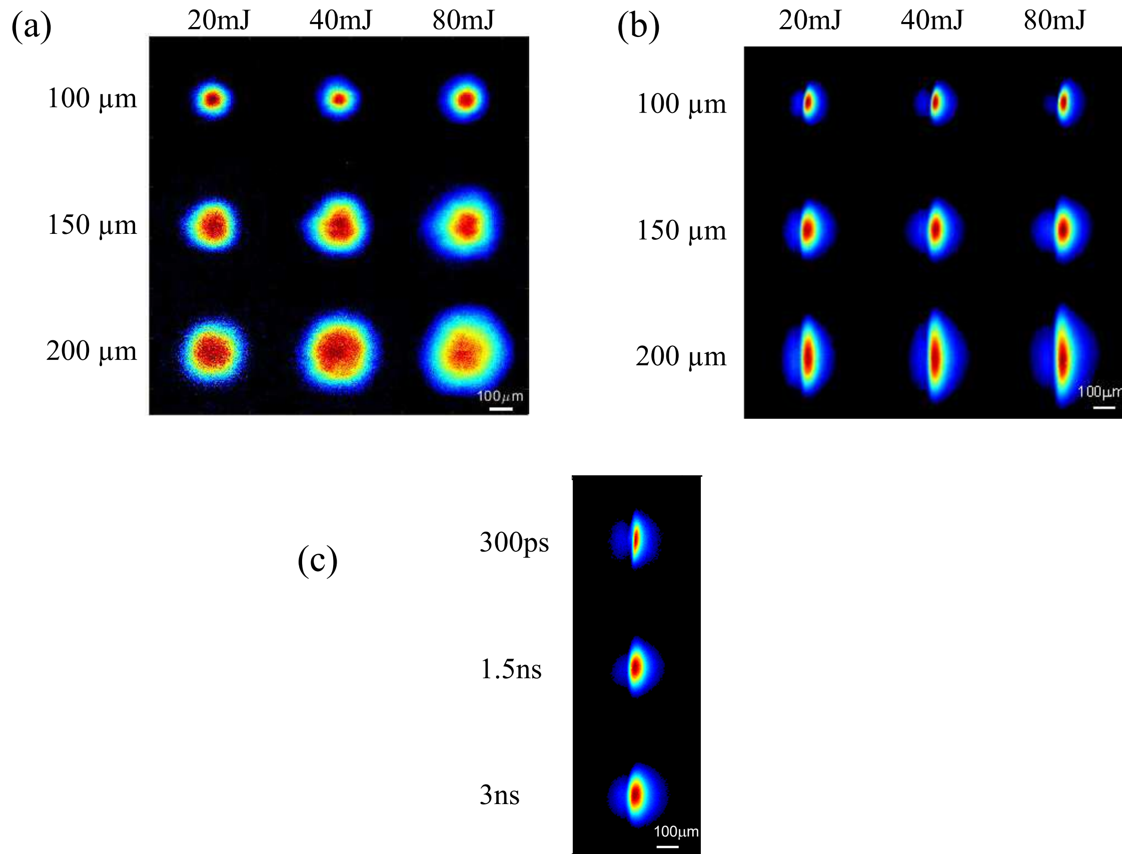

Figure 2-10. (a) In-band EUV images of plasma recorded normal to the target, and (b) tangential to the target. In (a) and (b), each row corresponds to one focal spot size, and each column corresponds to one laser pulse energy. (c) In-band EUV Images recorded tangential to the target for different irradiation pulse durations. The pulse energy was 40 mJ, and the focal spot size was 150 μm. The size of the EUV-emitting region in the direction of the target normal increases with the laser pulse duration. The pulse shape is square for all images.

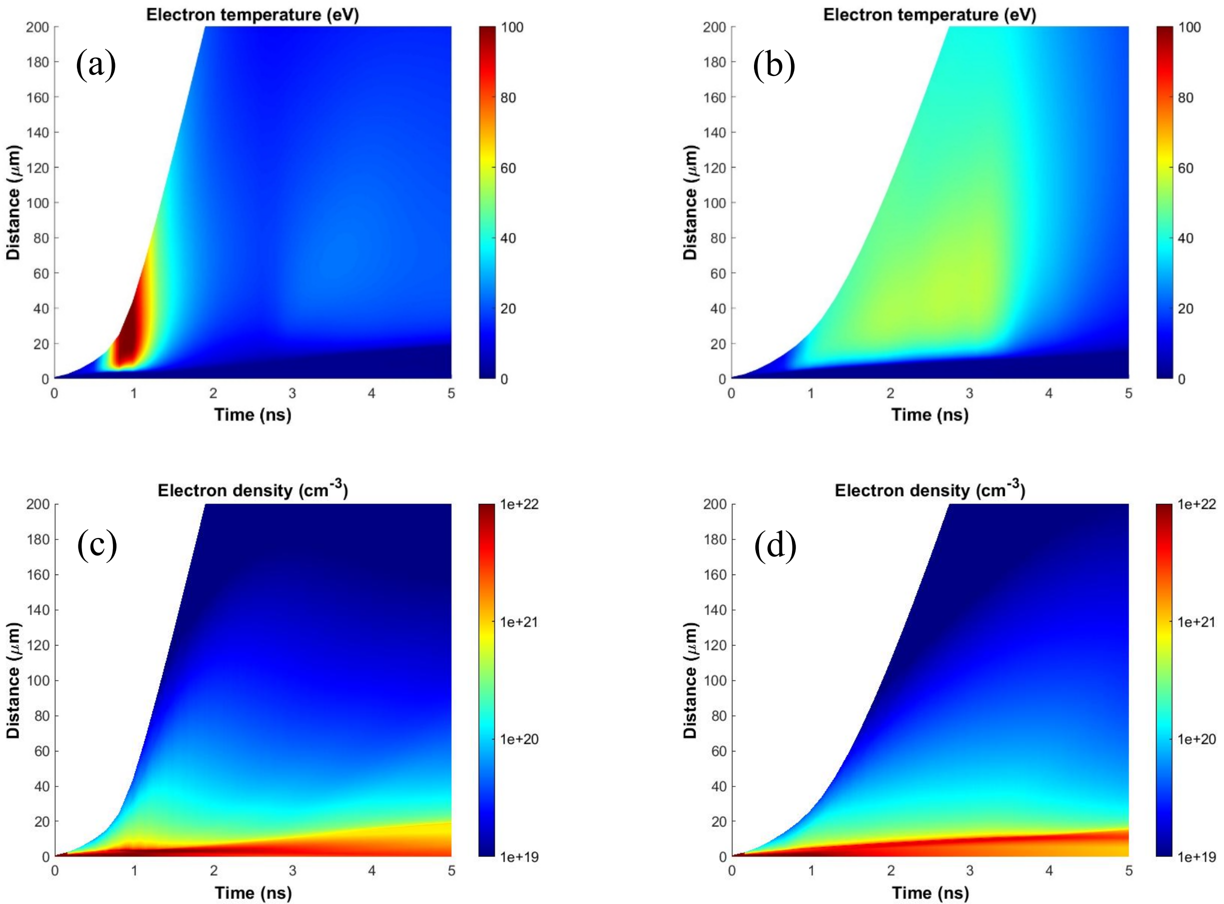

Figure 2-11. Simulated profile of plasma temperature of the Sn LPP created using: (a) 300ps pulse and (b) 3ns square pulse. (c) Simulated profile of electron density for a 300ps pulse, and (d) 3ns pulse. The laser pulse energy is 40 mJ, and focal spot size is 150 µm.

The resulting EUV spectra recorded as a function of irradiation intensity show that the wavelength corresponding to the peak emission has a 'V' shape dependence on the irradiation intensity. This is the result of the wavelength dependence of the n=4-n=4 transitions on the ion charge state and corroborates the well-known fact that that the peak intensity wavelength can be tuned to match the reflectivity band of Mo/Si mirror by changing the irradiation intensity. Time-resolved EUV emission measurements along the target normal show that the lifetime of EUV emission increases with irradiation pulse energy and can outlast the irradiation pulse by several nanoseconds. However, the duration of the EUV emission along the target surface is

similar to the irradiation pulse duration and is almost independent of pulse energy. This newly observed anisotropy of the EUV pulse duration is likely to the result of the competition between the rate of increase of the emitting plasma volume and the decrease of the emittance plasma as it expands and cools after the laser pulse ends. Another possible contributing cause is the creation of a cold plasma in the periphery of the irradiated spot at late times that can absorb the EUV radiation after the laser pulse ends. Experiments conducted irradiating the target with a sequence of two time-delayed pulses while maintaining the total pulse energy constant showed that the EUV yield remained almost the same, independent of the pulse separation. This suggests that re-heating of the plasma with delayed laser pulses is not a straightforward way to improve CE.

References

[1] D. J. Nagel, C. M. Brown, M. C. Peckerar, M. L. Ginter, J. A. Robinson, T. J. McIlrath, P. K. Carroll, T. J. McIlrath, and P. K. Carroll, Appl. Opt. 23, 1428 (1984).

[2] J. E. Bjorkholm, J. Bokor, L. Eichner, R. R. Freeman, J. Gregus, T. E. Jewell, W. M. Mansfield, A. A. Mac Dowell, E. L. Raab, and W. T. Silfvast, J. Vac. Sci. Technol. B Microelectron. Process. Phenom. 8, 1509 (1990).

[3] D. A. Tichenor, G. D. Kubiak, M. E. Malinowski, R. H. Stulen, S. J. Haney, K. W. Berger, R. P. Nissen, G. A. Wilkerson, P. H. Paul, S. R. Birtola, P. S. Jin, R. W. Arling, A. K. Ray-Chaudhuri, W. C. Sweatt, W. W. Chow, J. E. Bjorkholm, R. R. Freeman, M. D. Himel, A. A. MacDowell, D. M. Tennant, L. A. Fetter, O. R. Wood II, W. K. Waskiewicz, D. L. White, D. L. Windt, and T. E. Jewell, Electron-Beam, X-Ray, Ion-Beam Submicrom. Lithogr. Manuf. IV 2194, 95 (2005).

[4] M. van de Kerkhof, H. Jasper, L. Levasier, R. Peeters, R. van Es, J.-W. Bosker, A. Zdravkov, E. Lenderink, F. Evangelista, P. Broman, B. Bilski, and T. Last, Extrem. Ultrav. Lithogr. VIII 10143, 101430D (2017).

[5] S.-S. Kim, R. Chalykh, H. Kim, S. Lee, C. Park, M. Hwang, J.-O. Park, J. Park, H. Kim, and J. Jeon, in Extrem. Ultrav. Lithogr. VIII (International Society for Optics and Photonics, 2017), p. 1014306.

[6] I. V Fomenkov, in Extrem. Ultrav. Lithogr. X (International Society for Optics and Photonics,

2019), p. 1095719.

[7] A. Pirati, J. van Schoot, K. Troost, R. van Ballegoij, P. Krabbendam, J. Stoeldraijer, E. Loopstra, J. Benschop, J. Finders, H. Meiling, E. van Setten, N. Mika, J. Dredonx, U. Stamm, B. Kneer, B. Thuering, W. Kaiser, T. Heil, and S. Migura, Extrem. Ultrav. Lithogr. VIII 10143, 101430G (2017).

[8] E. van Setten, G. Bottiglieri, J. McNamara, J. van Schoot, K. Troost, J. Zekry, T. Fliervoet, S. Hsu, J. Zimmermann, M. Roesch, B. Bilski, and P. Graeupner, in Extrem. Ultrav. Lithogr. X (International Society for Optics and Photonics, 2019), p. 1095709.

[9] H. Tanaka, A. Matsumoto, K. Akinaga, A. Takahashi, and T. Okada, Appl. Phys. Lett. 87, 4 (2005).

[10] A. SUNAHARA, K. NISHIHARA, and A. SASAKI, Plasma Fusion Res. 3, 043 (2009).

[11] T. Ando, S. Fujioka, H. Nishimura, N. Ueda, K. Nagai, Y. Yasuda, K. Nishihara, T. Norimatsu, A. Sunahara, Y. Izawa, N. Miyanaga, K. Mima, and M. Murakami, Appl. Phys. Lett. 89, 151501 (2006).

[12] A. Roy, S. S. Harilal, M. P. Polek, S. M. Hassan, A. Endo, and A. Hassanein, Phys. Plasmas 21, (2014).

[13] Y. Tao, S. S. Harilal, M. S. Tillack, K. L. Sequoia, B. O'Shay, and F. Najmabadi, Opt. Lett. 31, 2492 (2006).

[14] P. Hayden, A. Cummings, N. Murphy, G. O'Sullivan, P. Sheridan, J. White, and P. Dunne, J.

Appl. Phys. 99, 093302 (2006).

[15] T. Okuno, S. Fujioka, H. Nishimura, Y. Tao, K. Nagai, Q. Gu, N. Ueda, T. Ando, K. Nishihara, T. Norimatsu, N. Miyanaga, Y. Izawa, K. Mima, A. Sunahara, H. Furukawa, and A. Sasaki, Appl. Phys. Lett. 88, 1 (2006).

[16] Y. Ueno, G. Soumagne, A. Sumitani, A. Endo, and T. Higashiguchi, Appl. Phys. Lett. 91, 1 (2007).

[17] A. Z. Giovannini and R. S. Abhari, J. Appl. Phys. 114, (2013).

[18] R. Kodama, T. Mochizuki, K. A. Tanaka, and C. Yamanaka, Appl. Phys. Lett. 50, 720 (1987).

[19] T. Higashiguchi, N. Dojyo, M. Hamada, W. Sasaki, and S. Kubodera, Appl. Phys. Lett. 88, 201503 (2006).

[20] A. M. Weiner, J. P. Heritage, and E. M. Kirschner, J. Opt. Soc. Am. B 5, 1563 (1988).

[21] A. M. Weiner, D. E. Leaird, J. S. Patel, and J. R. Wullert, Opt. Lett. 15, 326 (1990).

[22] J. A. Fülöp, Z. Major, B. Horváth, F. Tavella, A. Baltuška, and F. Krausz, Appl. Phys. B Lasers Opt. 87, 79 (2007).

[23] B. A. Reagan, A. H. Curtis, K. A. Wernsing, F. J. Furch, B. M. Luther, and J. J. Rocca, IEEE J. Quantum Electron. 48, 827 (2012).

[24] A. H. Curtis, B. A. Reagan, K. A. Wernsing, F. J. Furch, B. M. Luther, and J. J. Rocca, Opt. Lett. 36, 2164 (2011).

[25] L. Yin, H. Wang, B. A. Reagan, C. Baumgarten, E. Gullikson, M. Berrill, V. N. Shlyaptsev, and J. J. Rocca, Phys. Rev. Appl. 6, 034009 (2016).

[26] E. M. Gullikson, S. Mrowka, and B. B. Kaufmann, Emerg. Lithogr. Technol. V 4343, 363 (2003).

[27] B. M. Luther, Y. Wang, M. A. Larotonda, D. Alessi, M. Berrill, M. C. Marconi, J. J. Rocca, and V. N. Shlyaptsev, Opt. Lett. 30, 165 (2005).

[28] M. A. Larotonda, Y. Wang, M. Berrill, B. M. Luther, J. J. Rocca, M. M. Shakya, S. Gilbertson, and Z. Chang, Opt. Lett. 31, 3043 (2006).

[29] O. Morris, F. O'Reilly, P. Dunne, and P. Hayden, Appl. Phys. Lett. 92, 18 (2008).

[30] A. V Vinogradov and V. N. Shlyaptsev, Sov. J. Quantum Electron. 13, 1511 (1983).

[31] Y. V. Afanas'ev, V. P. Avtonomov, N. G. Basov, G. Korn, G. V. Sklizkov, and V. N. Shlyaptsev, J. Sov. Laser Res. 10, 1 (1989).

[32] M. Berrill, Y. Wang, M. A. Larotonda, B. M. Luther, V. N. Shlyaptsev, and J. J. Rocca, Phys. Rev. A - At. Mol. Opt. Phys. 75, 1 (2007).

[33] A. V Vinogradov and V. N. Shlyaptsev, Sov. J. Quantum Electron. 17, 1 (1987).

[34] R. Soufli, S. Bajt, R. Hudyma, and J. Taylor, in LLNL-BOOK-403314 (2008).

[35] S. Fujioka, H. Nishimura, K. Nishihara, A. Sasaki, A. Sunahara, T. Okuno, N. Ueda, T. Ando, Y. Tao, Y. Shimada, K. Hashimoto, M. Yamaura, K. Shigemori, M. Nakai, K. Nagai, T.

Norimatsu, T. Nishikawa, N. Miyanaga, Y. Izawa, and K. Mima, Phys. Rev. Lett. 95, 1 (2005).

[36] K. Nishihara, A. Sunahara, A. Sasaki, M. Nunami, H. Tanuma, S. Fujioka, Y. Shimada, K. Fujima, H. Furukawa, T. Kato, F. Koike, R. More, M. Murakami, T. Nishikawa, V. Zhakhovskii, K. Gamata, A. Takata, H. Ueda, H. Nishimura, Y. Izawa, N. Miyanaga, and K. Mima, Phys. Plasmas 15, (2008).

[37] R. C. Elton, X-Ray Lasers (Elsevier, 2012).

[38] J. Filevich, J. J. Rocca, E. Jankowska, E. C. Hammarsten, K. Kanizay, M. C. Marconi, S. J. Moon, and V. N. Shlyaptsev, Phys. Rev. E 67, 56409 (2003).

Chapter 3 A Programmable Pulse Synthesizer for the Generation of Joule-Level Picosecond Laser Pulses of Arbitrary Shape

3.1 Introduction

Laser pulse shaping and sequencing have been useful in a wide variety of applications, such as providing the optimal drive for inertial confinement fusion[1,2], increasing the gain and energy of plasma-based soft x-ray lasers [3][4][5], precompensation of pulse shape distortion in fiber amplifier systems [6], efficient optical parametric amplification [7], and optical manipulation of molecular motion [8]. Pulse-shaping also has application in increasing the conversion efficiency in laser-driven plasma sources for EUV lithography [9].

Several methods have been used to generate pulse shapes and pulse sequences. One is based on amplitude modulation, either direct modulation of the drive current of a CW master oscillator [10,11] or external modulation of its CW output [6,12–14]. In the direct modulation method, an arbitrary waveform generator (AWG) generates an electrical waveform which is converted and amplified by a current driver. The output of the current driver is then used to drive a CW master oscillator to generate laser pulses with arbitrary shapes. In the external modulation method, a single electro-optical modulator (EOM) or multiple EOMs controlled by an AWG are used to modulate the output of a CW master oscillator to obtain arbitrary laser pulse shapes, which are

seeded into amplifiers to generate shaped pulses with higher energy. Shaped pulses with energies up to 437 mJ and durations down to 0.43 ns have been demonstrated with a chain of amplifiers[15]. The EOM-based pulse shaping scheme can also be used to compensate the pulse shape distortion due to the gain saturation of amplifiers in fiber-based MOPA systems. However, since the master oscillators operate in the CW mode, pulses generated using this method are not compressible.

Besides amplitude modulation, phase modulation can also be used to temporally shape laser pulses [16]. Phase modulation can be achieved by introducing an array of liquid crystals between a nondispersive pair of gratings. The gratings are positioned at the object plane, and the image plane of a $4f$ lens system and the array of liquid crystals is placed at the Fourier plane of the $4f$ lens system. The array of liquid crystals works as a phase mask. Since the signal $f(t-\tau)$ in the time domain and the signal $F(\omega)\exp(-i\omega\tau)$ in the spectral domain are a Fourier transform pair, the phase retardation that is introduced into a certain spectral component in the spectral domain results in a temporal delay of the corresponding spectral component in the time domain. . Consequently, the temporal delay is limited to a few picoseconds [17].. Additionally, the amplitude of the temporally delayed pulses must be selected beforehand by using an amplitude mask. Another recently developed technique generated narrowband, low energy, temporally-shaped seed pulses with 4 ps resolution and several hundred picoseconds lengths through spectral shaping of a seed pulse combined with difference frequency generation [18]. This technique is advantageous because it allows direct temporal patterning as the mapping from the spectral shaping to time is linear and one-to-one, however the maximum record length is limited

to achievable stretch length of the chirped pulse amplification system involved in creation of these pulses.

Pulse stacking is a promising technique to temporally shape laser pulses. This technique usually involves pulse splitting and recombination. The pulse splitting can be implemented using amplitude division. An input laser pulse is split into ordinary and extraordinary sub-pulses using birefringent prisms. The sub-pulses are retroreflected by end mirrors and recombine at a polarizer. The shaping and amplification of picosecond pulses to 100mJ level energy was realized using pulse stacking [7]. However, the number of sub-pulses is limited by the complexity of the mechanical design. To the best of our knowledge, None of these system simultaneously generate synthesized pulses of Joule-level energy, resolution of a few picoseconds, and a record length greater than a few hundred picoseconds.

We report a pulse shaping technique with programmability for the generation of Joule-level pulses and pulse trains of arbitrary shapes up to 9ns long. The resolution of pulse shaping can be chosen to be 300 ps FWHM or 8 ps FWHM, depending on the specific application. This pulse shaping technique is also based on pulse stacking. In order to implement this pulse shaping technique, a pulse synthesizer was built and inserted into a cryogenically cooled diode-pumped Yb: YAG laser system [19,20]. The generated sub-pulses can be compressed to sub-5 ps FWHM. Trains of ten sub-pulses can be generated with peak powers of > 10 GW in the case all the sub-pulses are of equal amplitude.

3.2 Experimental setup

The pulse synthesizer illustrated in Figure 3-1, consists of three functional modules: a two-stage cylindrical telescope, an array of liquid crystals, and a set of sliding retro-reflectors inserted into a cryogenically cooled diode-pumped Yb: YAG laser system. The laser system, described latter, is composed of two room temperature regenerative amplifiers and a sequence of two cryogenically cooled Yb: YAG high power amplifiers. The input pulse from the first regenerative amplifier is horizontally expanded 100 times by the two-stage cylindrical telescope. The first telescope consists of an f=-5cm cylindrical lens and an f=10cm cylindrical lens, having an expansion factor of 2. The second stage consists of an f=1cm acylindrical lens and a 100cm radius of curvature concave cylindrical mirror, having an expansion factor of 50. The use of the acylindrical lens and the concave cylindrical mirror helps to significantly reduce the spherical aberration.

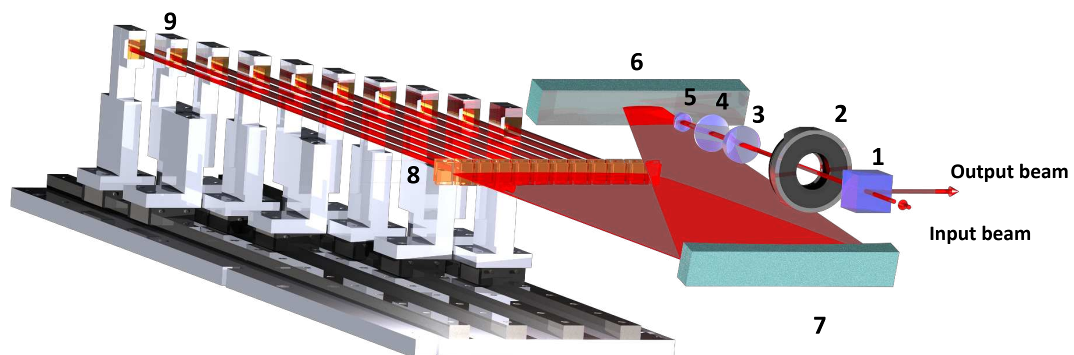

Figure 3-1 A 3-D schematic diagram of the pulse synthesizer. 1. Polarizing cube, 2. Have-wave plate, 3. Negative cylindrical lens, 4. Positive cylindrical lens, 5. Positive acylindrical lens, 6. Flat mirror, 7. Concave cylindrical mirror, 8. Liquid crystals, 9. Mobilized retroreflectors.

The horizontally expanded pulse is subsequently split into ten sub-pulses. Each sub-pulse passes through a liquid crystal retarder and is reflected back by a retro-reflector. The retroreflected sub-pulses again passthrough the liquid crystals and the telescope, where they are recombined. Finally, the sub-pulses are extracted by a polarizing cube. The pulse entering the pulse synthesizer is linearly polarized, and the direction of polarization can be tuned using a $\lambda/2$ wave plate. The polarization state of a sub-pulse changes after it passes through a liquid crystal twice. Therefore, the amplitude of each sub-pulse can be controlled by selecting the voltage applied to the corresponding liquid crystal. A Photography of the pulse synthesizer is shown in Figure 3-2. The transmission dependence of one single channel on the voltage applied was measured using the setup shown in Figure 3-3 (a) is shown in Figure 3-3 (b). There are two peaks of transmission corresponding to double-pass phase retardations of π and 3π. The voltage range from 1 V to 1.8 V was chosen for controlling the transmission. A block diagram of the system that controls the voltage applied to the liquid crystals is illustrated in Figure 3-4 (a). A photodiode detects the output of the laser system in real-time. The signal is digitized by an oscilloscope and is relayed to a laptop computer running the control algorithm. This control program compares the shape of the detected signal with the designed pulse shape and adjusts the voltages on the liquid crystals through a voltage control circuit in order to match the pulse shape of the output of the laser system to the designed pulse shape.

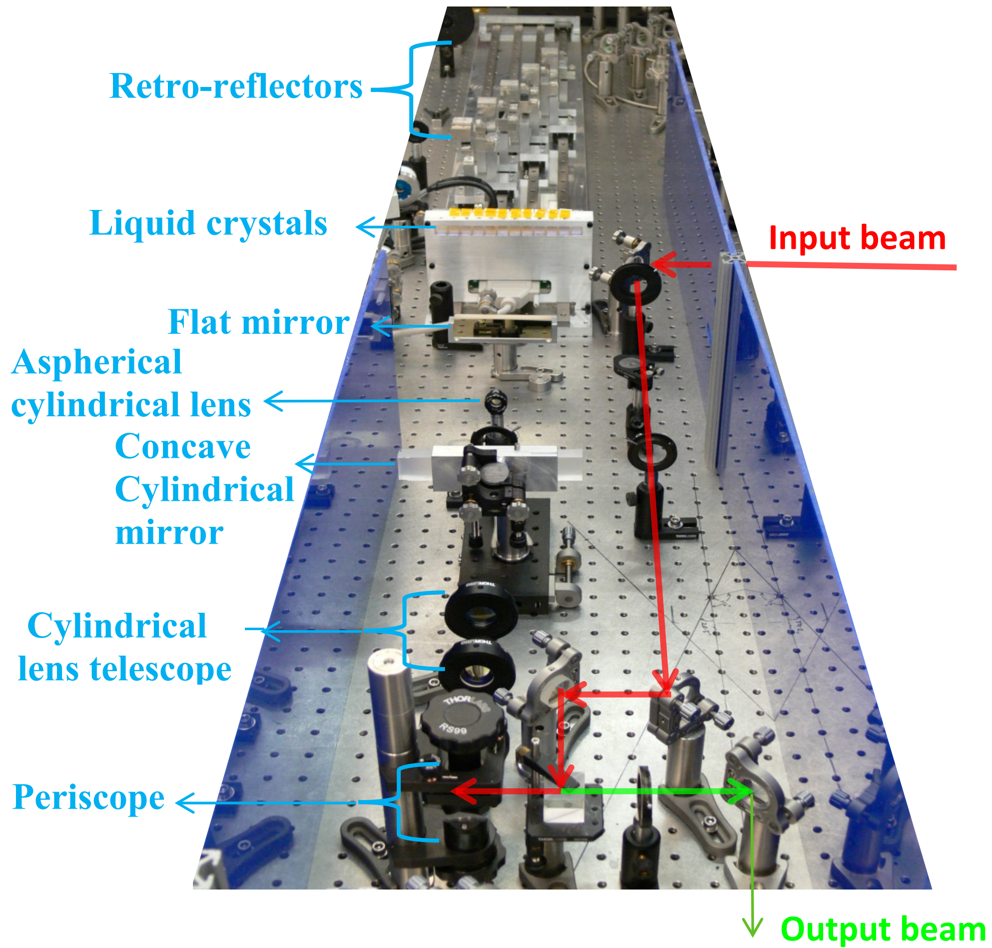

Figure 3-2 Photograph showing the layout and components of the pulse synthesizer. The red arrows indicate the optical path along which the input beam enters the pulse synthesizer. The green arrow indicates the output beam.

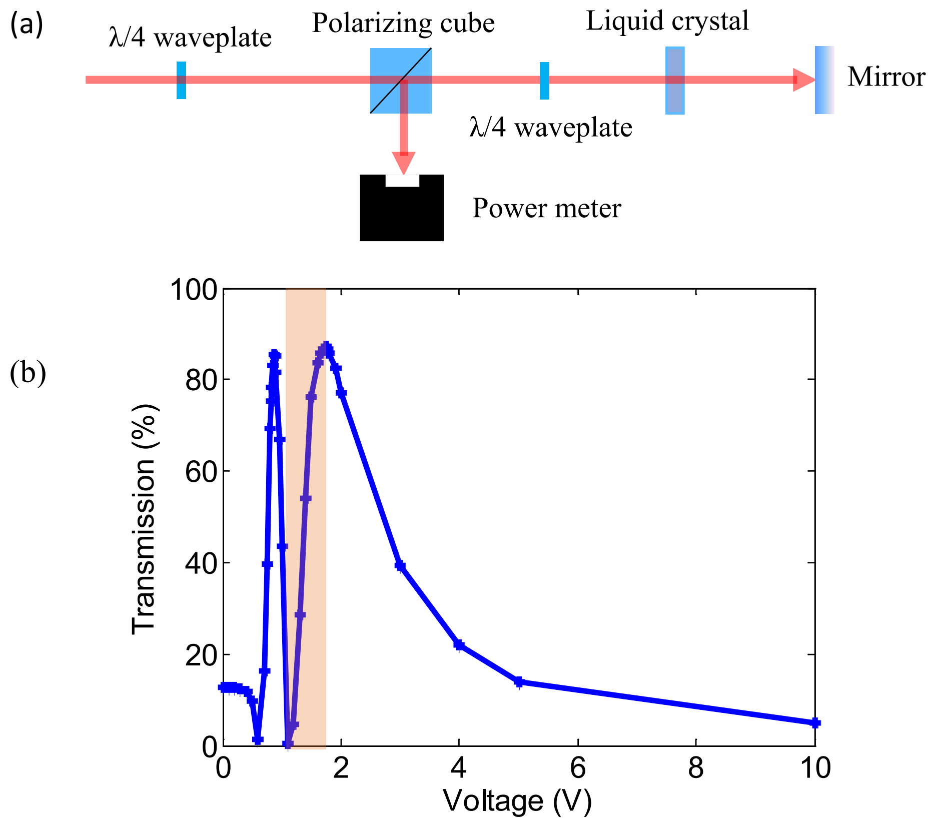

Figure 3-3 Measurement of the transmission of a pulse synthesizer channel. (a) Schematic of the experimental setup used for measuring the transmission of a channel of the pulse synthesizer. (b) Transmission measurement result. The two peaks represent phase retardation of π and 3π respectively. The shadowed region identifies the voltage range of adjustment used in this work.

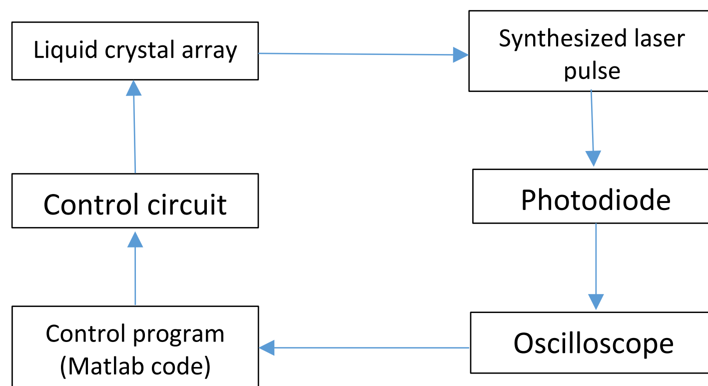

Figure 3-4 Synthesizer control system block diagram. The oscilloscope relays the waveform of the laser pulse detected by the photodiode to a computer. The control program obtains the difference between the detected waveform and a designed pulse shape and converts it into the voltages that need to be applied to the liquid crystals. The laser system will output a pulse shape that is closer to the designed pulse shape. The control system forms a closed loop.

The algorithm of the control program consists of three functional steps: initialization, comparison, and adjustment. **1) Initialization**. An amplitude array of ten elements m_n, with n=1-10 is introduced to describe the designed pulse shape. The element m_n represents the amplitude of the nth sub-pulse and has a range from 0 to 1. For example, a synthesized square pulse is represented by an array M_s = [1, 1, 1, 1, 1, 1, 1, 1, 1, 1] and a synthesized ramp pulse is represented by an array M_r = [1, 2, 3, 4, 5, 6, 7, 8, 9, 10]/10, as shown in Figure 3-5 (a) (b). When the program starts, it uses an initialization amplitude array M_0 = [1, 0, 0, 0, 0, 0, 0, 0, 0, 1] to maximize the amplitudes of the first sub-pulse and the tenth sub-pulse and minimize the amplitudes of the other sub-pulses, as shown in Figure 3-5 (c). The amplitude of a sub-pulse is changed according to the pre-measured liquid crystal transmission as a function of voltage shown in Figure 3-3 (b). The peaks of the first and tenth sub-pulse can be found at times $t=p_1$ and $t=p_{10}$. Since in this example, the sub-pulses are evenly separated, the temporal separation between every two adjacent sub-pulses is calculated as $s= (p_{10}- p_1)/9$. Therefore, the time corresponding to the peaks of all ten sub-pulses can be determined as an array of times: P= [p_1, p_1+s, p_1+2s, p_1+3s, p_1+4s, p_1+5s, p_1+6s, p_1+7s, p_1+8s, p_1+9s], where $p_1 + 9s = p_{10}$. **2) Comparison**. The program reads an acquired waveform from the oscilloscope. Given an array of times P, the amplitudes of the sub-pulse peaks in the acquired waveform can be found as an array A_{acq}= [a_1, a_2, a_3, a_4, a_5, a_6, a_7, a_8, a_9, a_{10}]. The amplitude array A_{acq} is normalized to its maximum element and is subsequently subtracted from the designed amplitude array M_{des}, resulting in an amplitude difference array D= [d_1, d_2, d_3, d_4, d_5, d_6, d_7, d_8, d_9, d_{10}], where $d_n=m_n-a_n$. **3) Adjustment**. With the amplitude difference array D and the pre-measured transmission as a function of voltage in Figure 3-3 (b), an array of voltage control signals V= [v_1, v_2, v_3, v_4, v_5, v_6,

v_7, v_8, v_9, v_{10}] is generated and relayed to the voltage control circuit. The voltage control circuit then adjusts the voltages on the liquid crystals according to V, changing the shape of the synthesized pulse.

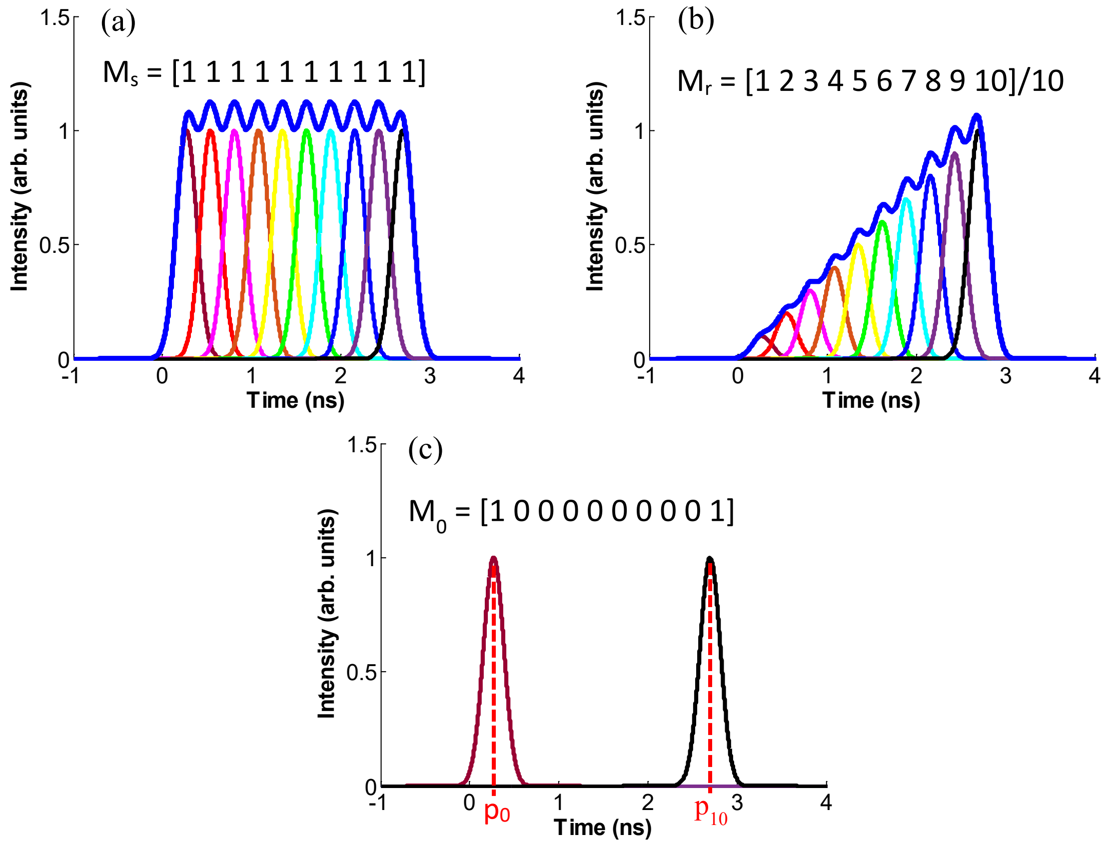

Figure 3-5 (a) Programmed synthesized square pulse, (b) programmed synthesized ramp pulse, (c) initialization of the control program.

The pulse synthesizer was implemented in a cryogenically cooled diode-pumped Yb: YAG laser system, as illustrated in Figure 3-6. Laser seed pulses are generated by a mode-locked Yb: KYW oscillator. The oscillator produces pulses at a repetition rate of 56MHz with an average power of 1 W. The oscillator pulses have a ~5nm FWHM spectral bandwidth centered at 1032nm and a pulse duration of ~ 300fs. In order to be amplified, these pulses are stretched into 300ps FWHM

pulses in a folded Martinez stretcher [21]. The stretched pulses are selected at 20 Hz repetition rate using a Pockels cell and are injected into a regenerative amplifier, as shown in Figure 3-7. This first regenerative amplifier produces 0.8 mJ laser pulses which are injected into the pulse synthesizer. After the pulse synthesizer, the total energy of the synthesized pulse is about 10 μJ and may vary with the pulse shape. Moreover, the sub-pulses are not co-linear after the pulse synthesizer. To facilitate efficient amplification in the cryogenically-cooled Yb: YAG power amplifiers, the synthesized pulses are injected into a second regenerative amplifier which not only increases their pulse energy to compensate for loses in the pulse shaper but also improves their beam quality. The sub-pulses from the pulse synthesizer are overlapped with the pump spot in the second regenerative amplifier gain medium by adjusting the retro-reflectors. After being amplified by the second regenerative amplifier, the total pulse energy of the train of ten sub-pulses is brought back to ~ 0.8 mJ. The beam quality of the sub-pulses is significantly improved by the second regenerative amplifier, and additionally the sub-pulses are made co-linear after being amplified as required for efficient further amplification and use.

The synthesized pulse train is first amplified to ~100 mJ by the first of two cryogenically-cooled Yb: YAG amplifiers and is subsequently further amplified to 1.3 J by the second amplifier. This two stages of high power cryogenically-cooled Yb: YAG amplifiers are similar to those described in reference [22] and [19] respectively. They are based on liquid nitrogen-cooled active mirror slabs and make use of multi-pass configurations. A sequence of two Pockels cells and three polarizers is inserted between the second regenerative amplifier and the first cryogenically-cooled power Yb: YAG amplifier to suppress on-axis amplified spontaneous emission and leakage from the second regenerative amplifier.

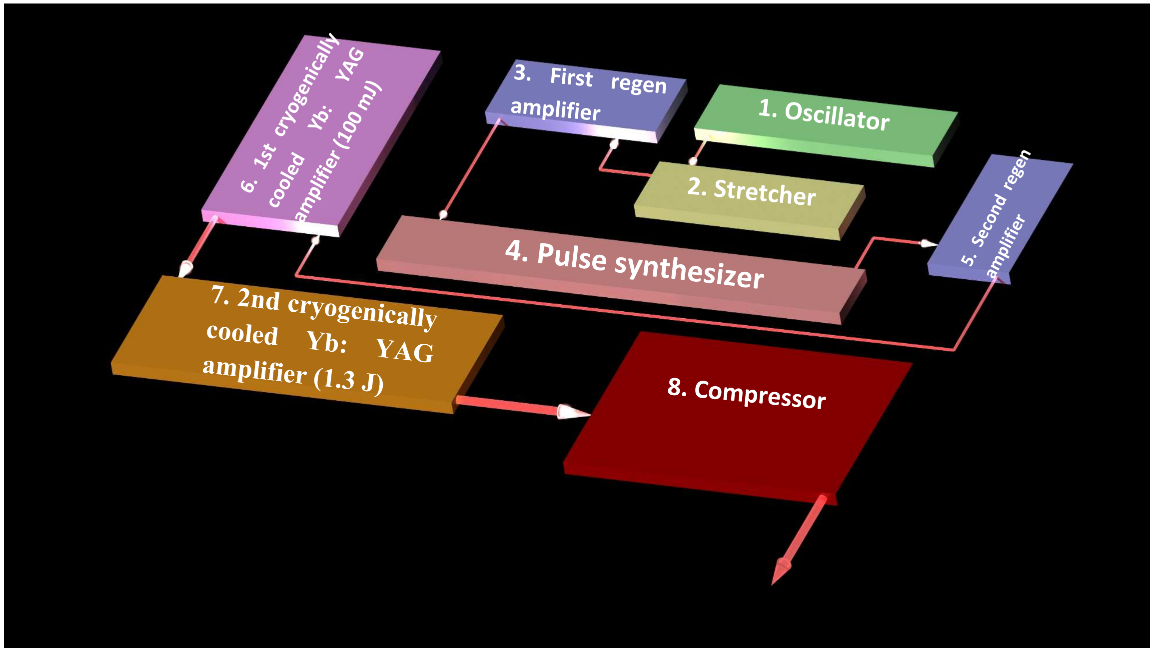

Figure 3-6 Schematic of the laser system for the generation of synthesized pulses.

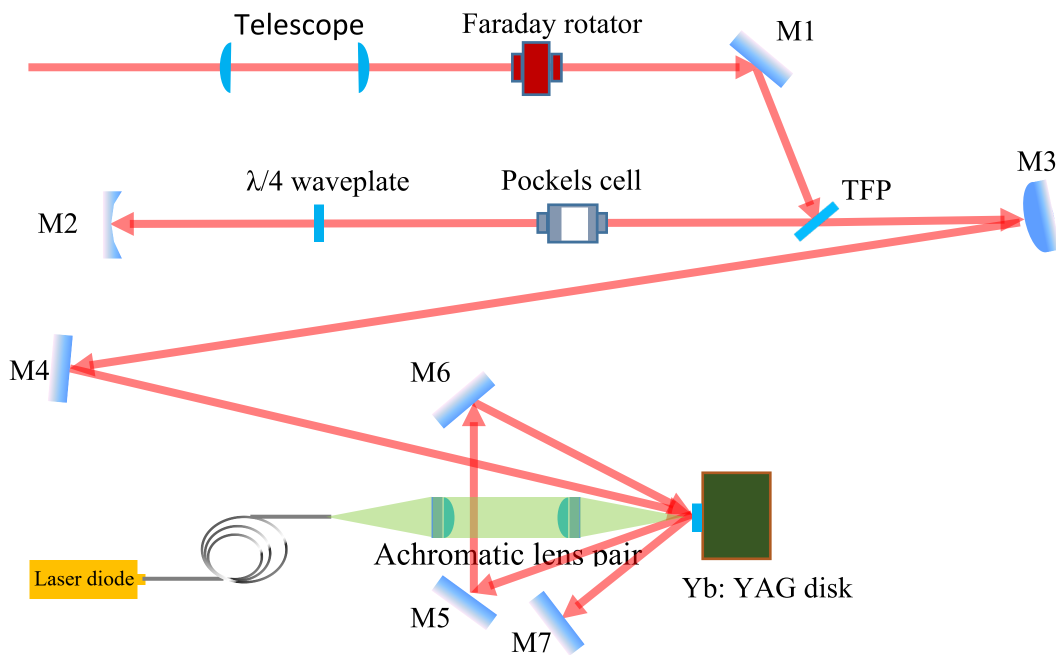

Figure 3-7 Schematic of the regenerative amplifier.

Another advantage of this pulse shaping technique is that the synthesized high energy pulses are chirped and can be compressed into sub-pulses of picosecond duration by a grating pulse compressor [20]. The cryogenically cooled Yb: YAG amplifiers have a bandwidth of ~ 0.3nm, which is sufficient to allow compression into pulses of sub-5 ps duration[22]. The peak power of a sub-pulse in a compressed pulse shape can be as high as 10 GW for the case in which all sub-pulses have equal amplitude.

3.3 Results and discussion

The pulse synthesizer enables us to generate high energy synthesized pulses with arbitrary shapes and pulse sequences. Figure 3-8 shows examples of synthesized pulse shapes and pulse sequences in the nanosecond pulse regime with a total pulse energy of 1.3 J. A sequence of 300 ps FWHM pulses, a rectangular pulse and a down-ramp pulse are shown. From the output of the pulse synthesizer (10 μJ) to the output of the second cryogenically-cooled Yb: YAG amplifier (1.3 J), the amplification factor is as high as 1.3×10^5. The programmable nature of the device allows us to compensate for gain saturation to obtain high energy pulses of arbitrary shapes. Hence, we have demonstrated a pulse synthesizer with the capacity to form any pulse shapes under high amplification factors.

The use of the synthesizer in a chirped pulse amplification laser system also allows us to also generate pulse sequences and pulses of arbitrary shape in the picosecond regime. These pulses were generated using the same setup used to generate the pulses shown in Figure 3-8 and adding a grating pulse compressor. The gratings are dielectric gratings with 1720 lines/mm for 1.03 µm

wavelength. The efficiency of the compressor is ~ 70%. After the compressor, the sub-pulses were compressed to ~ 8 ps FWHM. Figure 3-9 shows four examples of the compressed pulse sequences.

The capabilities of this pulse shaper can be further extended. The position of the retroflectors can be altered by motors controlled by a computer, which will allow adjusting the temporal separation between any two sub-pulses in real-time. The real-time programmability of this pulse synthesizer offers the opportunity to develop a self-learning system to search for the optimal pulse shapes for given applications. These include, for example, the excitation of laser plasma-based soft x-ray lasers which are very sensitive to the amplitude, shape and time of pre-pulses. Another example is the optimization of the EUV emission of laser-created plasmas for advanced lithography, where a high level of control of pre-pulses could result in an improvement in conversion efficiency into the EUV. The control system could be upgraded to measure the output of the EUV lithography light source or soft x-ray laser source, and a genetic algorithm could be used to scan the parameter space of pulse shapes and intensity for optimal output.

In summary, we have demonstrated a novel pulse shaping technique based on wave front division and recombination. With this technique, we were able to synthesize 1.3 J pulses of arbitrary shapes up to 9ns long with a resolution of 8 ps .The demonstrated pulse shaping technique can become a powerful tool in several applications in light-matter interactions for radiation sources in which the time history of the main pulse and pre-pulses is important.

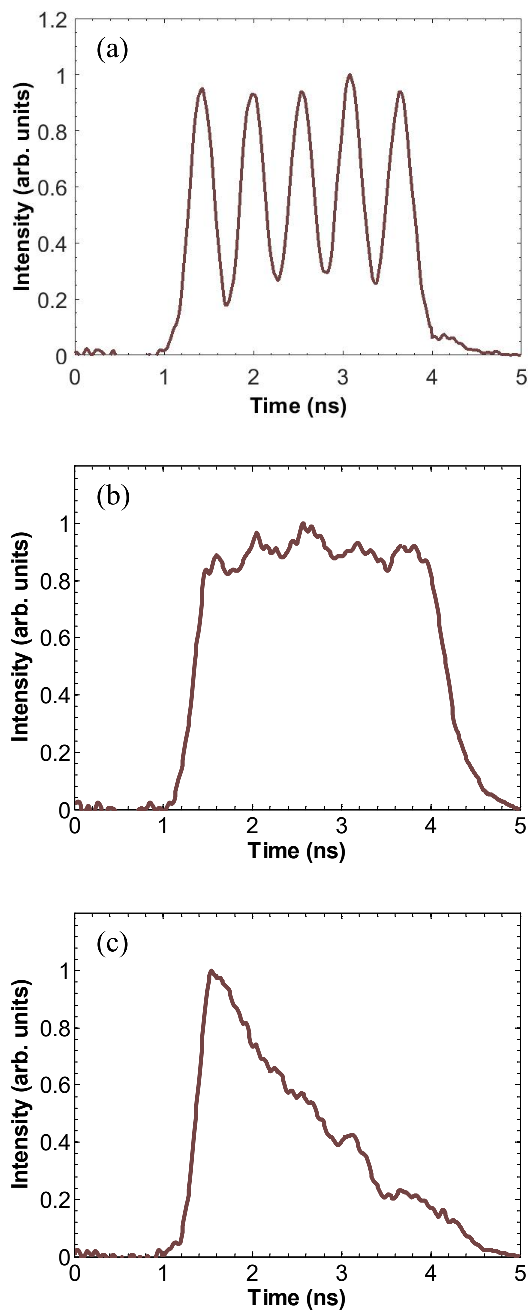

Figure 3-8 Examples of 1.3 J synthesized pulses. (a) Synthesized train of five pulses. The modulation can be adjusted by selecting the separation between pulses, (b) synthesized square pulse, (c) synthesized down-ramp pulse.

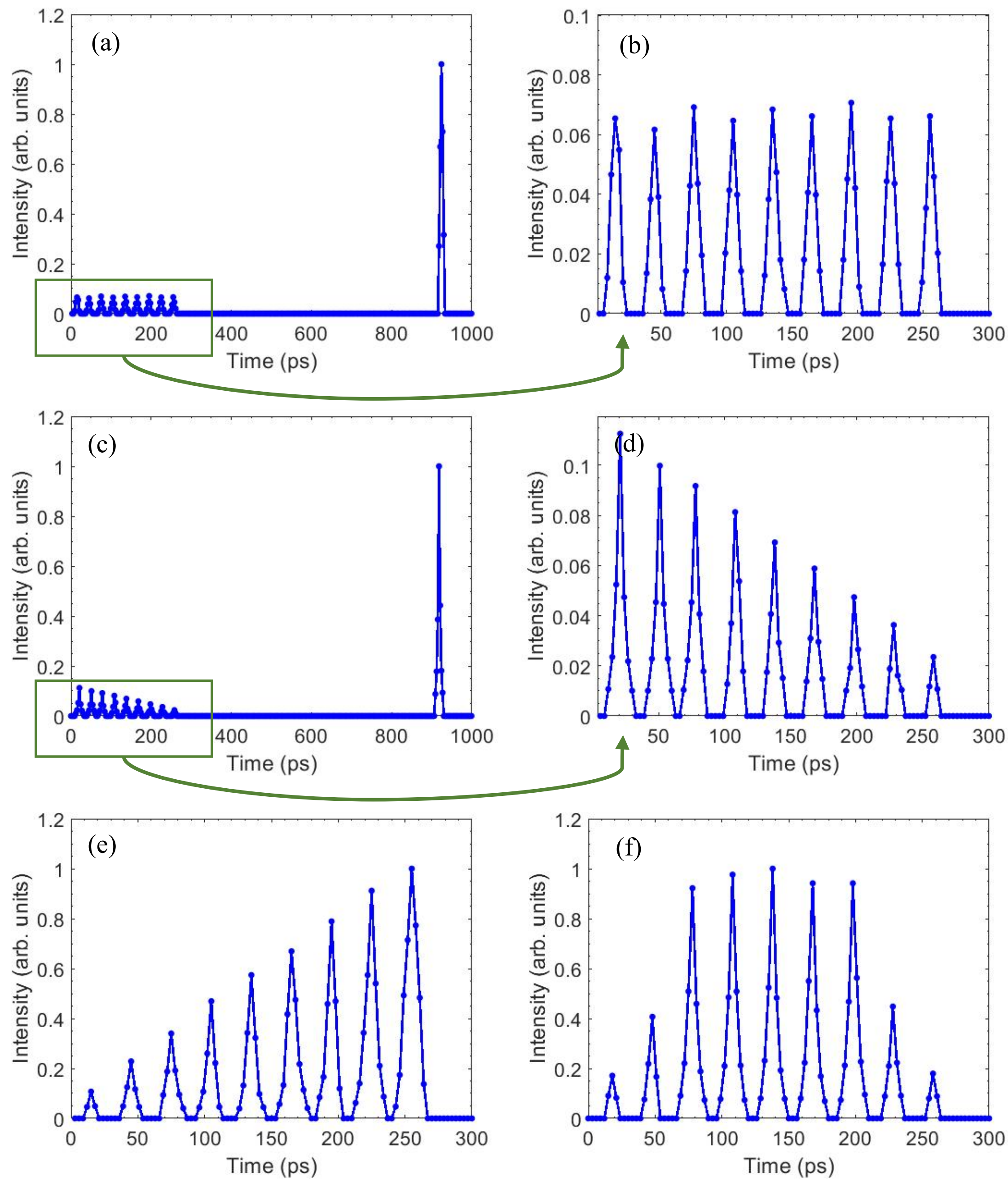

Figure 3-9 Autocorrelation results of the compressed synthesized trains of picosecond pulses. (a) Synthesized train of nine pre-pulses and a main pulse. The temporal separation between two adjacent pre-pulses is 30 ps, and the main pulse is delayed by 670 ps from the last pre-pulse. The pre-pulses have almost the same intensity. (b) A zoomed-in figure of the nine pre-pulses in (a). (c) Synthesized train of nine pre-pulses and a main pulse. The temporal separation between two adjacent pre-pulses is 30 ps, and the main pulse is delayed by 670 ps from the last pre-pulse. The pre-pulses form a ramp down shape. (d) A zoomed-in figure of the nine pre-pulses in (c). (e) Synthesized up-ramp pulse train of nine pulses. (f) Synthesized plateau pulse train. The temporal separation between two adjacent pre-pulses is 30 ps. The total energy of the pulse train is 0.9 J in (a), (c), (e), and (f). The duration of each pulse is ~ 8 ps FWHM.

References

1. S. C. Burkhart, R. B. Wilcox, D. Browning, and F. A. Penko, "Amplitude and Phase Modulation with Waveguide Optics," Proc. SPIE 3047, Solid State Lasers Appl. to Inert. Confin. Fusion Second Annu. Int. Conf. (1997).

2. O. A. Hurricane, D. A. Callahan, D. T. Casey, P. M. Celliers, C. Cerjan, E. L. Dewald, T. R. Dittrich, T. Döppner, D. E. Hinkel, L. F. B. Hopkins, J. L. Kline, S. Le Pape, T. Ma, A. G. Macphee, J. L. Milovich, A. Pak, H. S. Park, P. K. Patel, B. A. Remington, J. D. Salmonson, P. T. Springer, and R. Tommasini, "Fuel gain exceeding unity in an inertially confined fusion implosion," Nature **506**(7488), 343–347 (2014).

3. J. Nilsen, B. J. MacGowan, L. B. Da Silva, J. C. Moreno, K. Cammann, B. Ahlers, D. Henn, C. Dumschat, and A. A. S, "Prepulse technique for producing low-Z Ne-like x-ray lasers," Phys. Rev. A **48**(6), 4682–4685 (1993).

4. P. V. Nickles, V. N. Shlyaptsev, M. Kalachnikov, M. Schnürer, I. Will, and W. Sandner, "Short pulse X-ray laser at 32.6 nm based on transient gain in Ne-like titanium," Phys. Rev. Lett. **78**(14), 2748–2751 (1997).

5. B. A. Reagan, M. Berrill, K. A. Wernsing, C. Baumgarten, M. Woolston, and J. J. Rocca, "High-average-power , 100-Hz-repetition-rate , tabletop soft-x-ray lasers at sub-15-nm wavelengths," Phys. Rev. A **053820**, 1–7 (2014).

6. M. Nie, Q. Liu, E. Ji, X. Cao, X. Fu, and M. Gong, "Active pulse shaping for end-pumped

Nd:YVO4 amplifier with high gain," Opt. Lett. **42**(6), 1051–1054 (2017).

7. J. A. Fülöp, Z. Major, B. Horváth, F. Tavella, A. Baltuška, and F. Krausz, "Shaping of picosecond pulses for pumping optical parametric amplification," Appl. Phys. B Lasers Opt. **87**(1), 79–84 (2007).

8. A. M. Weiner, D. E. Leaird, G. P. Wiederrecht, K. A. Nelson, and D. M. Hercules, "Femtosecond Pulse Sequences Used for Optical Manipulation of Molecular Motion," Science **247**(4948), 1317–1319 (1990).

9. A. A. Schafgans, D. J. Brown, I. V. Fomenkov, R. Sandstrom, A. Ershov, G. Vaschenko, R. Rafac, M. Purvis, S. Rokitski, Y. Tao, D. J. Riggs, W. J. Dunstan, M. Graham, N. R. Farrar, D. C. Brandt, N. Böwering, A. Pirati, N. Harned, C. Wagner, H. Meiling, and R. Kool, "Performance optimization of MOPA pre-pulse LPP light source," Extrem. Ultrav. Lithogr. VI **9422**, 94220B (2015).

10. K. T. Vu, A. Malinowski, and D. J. Richardson, "Adaptive pulse shape control in a diode-seeded nanosecond fiber MOPA system," Opt. Express **14**(23), 10996–11001 (2006).

11. D. N. Schimpf, C. Ruchert, D. Nodop, J. Limpert, F. Salin, and T. Andreas, "Compensation of pulse-distortion in saturated laser amplifiers Abstract :," Opt. Express **16**(22), 330–339 (2008).

12. M. Nie, X. Cao, Q. Liu, E. Ji, X. Fu, P. M. Technology, and P. Instrument, "100 μJ pulse energy in burst-mode-operated hybrid fiber-bulk amplifier system with envelope shaping," Opt. Express **25**(12), 13557–13566 (2017).

13. R. A. Meijer, A. S. Stodolna, K. S. E. Eikema, and S. Witte, "High-energy Nd:YAG laser system with arbitrary sub-nanosecond pulse shaping capability," Opt. Lett. **42**(14), 2758–2761 (2017).

14. G. Brunton, G. Erbert, D. Browning, and E. Tse, "The shaping of a national ignition campaign pulsed waveform," Fusion Eng. Des. **87**(12), 1940–1944 (2012).

15. R. A. Meijer, A. S. Stodolna, K. S. E. Eikema, and S. Witte, "High-energy Nd:YAG laser system with arbitrary sub-nanosecond pulse shaping capability," Opt. Lett. **42**(14), 2758–2761 (2017).

16. A. M. Weiner, J. P. Heritage, and E. M. Kirschner, "High-resolution femtosecond pulse shaping," J. Opt. Soc. Am. B **5**(8), 1563 (1988).

17. A. M. Weiner, D. E. Leaird, J. S. Patel, and J. R. Wullert, "Programmable femtosecond pulse shaping by use of a multielement liquid-crystal phase modulator," Opt. Lett. **15**(6), 326 (1990).

18. D. E. Mittelberger, R. D. Muir, M. Y. Hamamoto, M. A. Prantil, and J. E. Heebner, "Frequency-to-time optical arbitrary waveform generator," Opt. Lett. **44**(11), 2863 (2019).

19. F. J. Furch, B. A. Reagan, B. M. Luther, A. H. Curtis, S. P. Meehan, and J. J. Rocca, "Demonstration of an all-diode-pumped soft x-ray laser," Opt. Lett. **34**(21), 3352–3354 (2009).

20. B. A. Reagan, K. A. Wernsing, A. H. Curtis, F. J. Furch, B. M. Luther, D. Patel, C. S. Menoni,

and J. J. Rocca, "Demonstration of a 100 Hz repetition rate gain-saturated diode-pumped table-top soft x-ray laser," Opt. Lett. **37**(17), 3624–3626 (2012).

21. O. Martinez, "3000 times grating compressor with positive group velocity dispersion: Application to fiber compensation in 1.3-1.6 µm region," IEEE J. Quantum Electron. **23**(1), 59–64 (1987).

22. A. H. Curtis, B. A. Reagan, K. A. Wernsing, F. J. Furch, B. M. Luther, and J. J. Rocca, "Demonstration of a compact 100 Hz, 0.1 J, diode-pumped picosecond laser," Opt. Lett. **36**(11), 2164 (2011).

Chapter 4 Comprehensive Characterization of BEUV Emission from Gd/Tb LPP

4.1 Introduction

The continuous increase in the number of transistors per chip that has fueled the growth of the semiconductor industry for the past several decades [1] requires printing increasingly smaller features. Progress in lithography is key in enabling this growth. To make this possible, projection lithography using progressively shorter wavelengths has been employed in combination with other solutions. Immersion lithography with λ=193 nm light and its combination with multiple patterning has been used for the past several years to continue reducing the critical dimension. This has allowed the semiconductor industry to reach the 14nm node for MPU and DRAM as outlined in the International Technology Roadmap for Semiconductors (ITRS) in high volume production using this wavelength, a remarkable achievement. However, the use of 193 nm illumination is approaching its ultimate limit [2]. Extreme Ultraviolet Lithography (EUVL) using λ=13.5 nm light generated from laser-produced Sn plasmas is being used by device manufactures to develop processes for insertion into high volume manufacturing at the 7nm logic node [3]. This technology, which has been in development for decades, will serve to manufacture the next generations of computer processors and other integrated circuits. Given the long time necessary to translate such complex technology into high volume manufacturing, interest has recently

arisen in light sources near λ = 6.7 nm for the development of the next generation lithography, termed "beyond extreme ultraviolet lithography" (BEUVL), because of the availability of highly reflective mirrors at this wavelength.

Highly ionized Gd and Tb plasmas emitting at wavelengths near λ = 6.7 nm [4,5] in the form of an unresolved transition array (UTA) are primary light source candidates for BEUVL [6]. They can produce intense emission within the reflection region of La/B-multilayer mirrors, whose near normal incidence reflectivity can theoretically reach values up to 80% [7]. A reflectivity of 64.1% at λ = 6.65nm with 0.06nm FWHM bandwidth has been already realized experimentally [8]. Complementing research on high reflectivity mirror coatings and photoresist, the development of a high-power light source at this wavelength is a significant challenge that must be addressed. The spectral profile of the emission is determined by the plasma parameters, in particular the ion species distribution. The n=4-4 transitions from Gd^{16+}-Gd^{20+} emit in the neighborhood of 6.7 nm [5]. Previously reported steady state plasma computations have estimated that Gd plasmas have the maximum emission near 6.7nm when the electron temperature T_e is around 120ev [9]. The electron temperature is mainly determined by the laser intensity. Aside from the plasma temperature and density, the plasma size also plays a role in the emission, affecting both its rate of expansion and opacity. The rate of expansion determines the rate of adiabatic cooling [10] that affects the conversion efficiency of laser energy into BEUV emission.

The results of several previous studies of the emission from laser-produced Gd plasmas in the spectral region of interest for BEUVL have been published [4,9,11–15]. Measurements of CE as a function of laser intensity have been reported from different experiments conducted using

different laser pulse durations. In one of them λ= 1064 nm wavelength pulses of 10ns duration were used to achieve a CE of up to 0.3 % into a 0.6% bandwidth in 2π solid angle and a maximum CE of 0.4% was reported using λ= 1064 μm 150 ps pulses from a different laser [11]. By using low density target and dual laser pulse irradiation, the CE was observed to be as high as 0.54% when a main pulse intensity of 5.6×10^{12} W/cm^2 was used [12]. Another work reported a CE of 0.8% into the same bandwidth from one-dimensional spherical plasmas produced by a twelve joule Nd: glass laser [13]. Laser pulses from a λ= 10.6 μm CO_2 laser have been reported to produce a maximum CE of 0.7% at a laser irradiation intensity of 1.2×10^{11} W/cm^2 [14]. In all cases the CE results were obtained by measuring the 6.7nm light emitted using a single detector placed at a fixed angle with respect to the target and assuming that the emission was isotropic. Other experiments have been conducted to observe the spectral distribution of the emission of interest [4,9,11–15], and one experiment reported the Gd plasma size plasma images obtained with an X-ray pinhole camera [13]. In summary, a significant amount of information has recently been obtained from different experiments conducted using different lasers.

In this paper, we report the results of a comprehensive study of the λ = 6.7nm BEUV emission from laser produced Gd and Tb plasmas over a broad range of irradiation pulse parameters using the same experimental setup and a single laser with pulse duration tunable from 120 ps to 4 ns for all the measurements. This allows for direct comparison of the results without the possible inconsistencies that could arise from comparisons of measurements made using different setups. A suite of diagnostics was employed including an array of five calibrated energy monitors that measured the angular distribution of the BEUV emission for angles ranging from normal incidence to grazing. This allowed us to make more accurate estimates of the CE without

assuming isotropic emission as in past measurements [11,13]. BEUV emission spectra were measured as a function of laser pulse duration, emission angle, and spatial location within the plasma to understand the plasma conditions relevant to conversion efficiency. Images of the BEUV emitting plasma region at BEUV wavelength were obtained as a function of irradiation parameters. CE and spectral measurements are also reported for Tb plasmas. A maximum CE of 0.47% into a 0.6% bandwidth centered at λ = 6.74nm in 2π solid angle was measured for a Gd plasma created by 2ns laser pulses, and a similar CE of 0.45% was measured for a Tb plasma. The plasma physics behind the measured trends is discussed below with the support of transient hydrodynamic / atomics physics simulations. The simulations were conducted using an upgraded version of the hydrodynamic / atomic physics code RADEX [16–19] originally developed to simulate plasmas for soft x-ray laser amplification, employing a Lagrangian grid and atomic collisional and radiative rates from the HULLAC code [20]. RADEX calculates self-consistent radiation transport for several hundred thousand lines originating from more than 5000 levels of all possible ion stages. Radiation transport is computed using the Biberman-Holstein approximation. This chapter was previously published in reference [21].

4.2 Experimental Setup

shows a schematic of the experiment setup. We used a diode-pumped, chirped pulse amplification (CPA) laser system based on a cryogenically-cooled Yb: YAG amplifier that produces pulses with energies of up to 100 mJ at λ = 1030nm [22,23]. This laser provides pulses with duration ranging from 120 ps to 4 ns at a repetition rate of up to 100 Hz. Its output can also be

boosted up to 1 J installing an additional amplifier [24,25], but the experiments reported here were conducted at energies below 100mJ. Laser pulses of 120-220 ps durations were generated by adjusting the grating pulse stretcher. Durations of 2-4ns were produced by operating the regenerative amplifier in Q-switch / cavity-dump mode and subsequently temporally clipping the pulses to the desired pulse duration using a Pockels cell and a polarizer pair prior to further amplification. This approach preserves the laser beam spatial characteristics when the laser is switched between different pulse durations, allowing for a more direct comparison of the dependence of BEUV emission on pulse duration than if different lasers were used. Pulses from this laser were focused in vacuum onto polished Gd and Tb slab targets using three different lenses to obtain focal spot diameters of 30µm, 55µm and 85µm FWHM. The targets were mounted on a motorized stage in order to renew the target surface after each shot. Consequently, the average BEUV output power is expected to increase linearly as a function of repetition rate provided absorption of the generated radiation by increased amount of vapor in the chamber is not an issue.

An array of five calibrated BEUV energy monitors was used to simultaneously measure the angular distribution of the BEUV emission on every shot. These energy monitors were positioned on an 18 cm radius circle with the plasma at the center at angles of 6°, 26°, 46°, 66°, 86° with respect to the normal of the target surface. Each energy monitor contained a BEUV sensitive silicon photodiode, a thin zirconium foil to reject visible light, and a La/B_4C multilayer mirror with reflectivity centered at about 6.74nm with a bandwidth of 0.08 nm FWHM (Figure 4-1. (b)). The total (foil, mirror and photodiode) spectral responsivity of each energy monitor was calibrated using the Advanced Light Source synchrotron (ALS) (Figure 4-1 (c)).

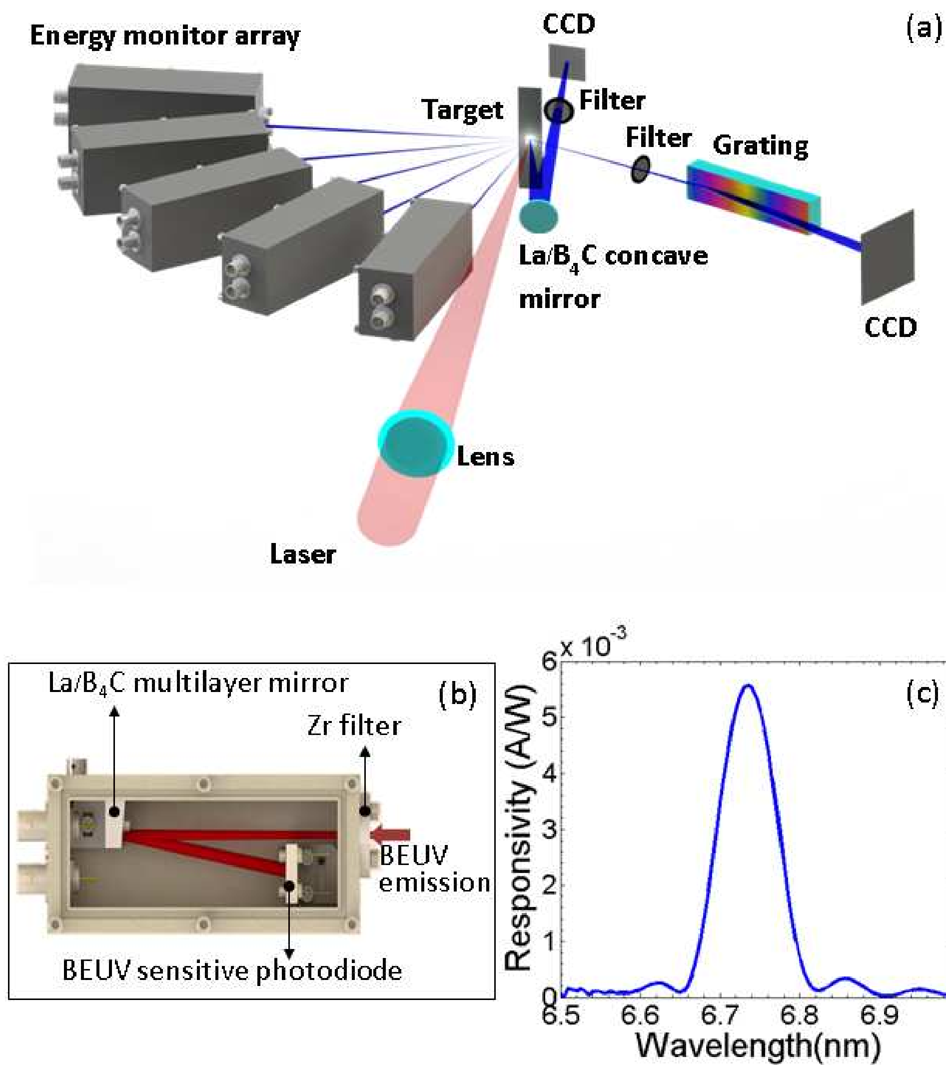

Figure 4-1. (a) Schematic diagram of the experiment setup. (b) Internal configuration of the energy monitors. (c) Absolute calibration of the responsivity of one of the energy monitors measured using the ALS synchrotron.

The measurement of the BEUV emission from near-normal to near-grazing incidence with calibrated detectors allows for accurate conversion efficiency measurements. The spectral emission was measured using a flat-field grazing incidence spectrometer consisting of a variable-line-spacing diffraction grating with a nominal ruling of 1200 lines/mm and a back-illuminated CCD detector. The spectrometer, which has a spectral resolution of about 0.03 nm, was calibrated using the second diffraction order of C V/ C VI emission lines which were excited by irradiating a

graphite target. The spectrometer was placed to observe the spectral emission at angles of 20°, 60° and 85° with respect to target normal. The efficiencies of the spectrometer diffraction grating and foil filter over the spectral band of interest were also calibrated at the ALS.

In addition, we used a BEUV imaging system to measure the size of BEUV emitting plasma region from both normal (frontview) and lateral (sideview) direction. Images of the plasma emission at BEUV wavelength were obtained using a La/B_4C multilayer concave mirror with a radius of curvature of 230 mm and a EUV-sensitive CCD. The magnification of this imaging system for frontview imaging and sideview imaging was 13x and 14x, respectively. The combination of the La/B_4C multilayer mirror with Ag and Al foils to block longer wavelength light ensures that only the emission near λ = 6.7nm contributes to the plasma images. The characteristics of this imaging system include high in-band fluence that results in a high signal to noise ratio and a spatial resolution of ~ 5µm on the object plane limited by spherical aberration of the mirror. Since the size of the plasmas in our experiments was in the range from 30µm to 100 µm, this imaging system has the capability of producing high resolution in-band images of the plasma sources.

4.3 Spectral Characterization

In this section we discuss the spectral characterization of the Gd and Tb plasmas. This includes the variations of the BEUV spectral emission as a function of laser pulse duration, viewing angle, and spatial location within plasma. To measure the BEUV spectral emission as function of laser pulse duration the spectrometer was aligned to capture the plasma emission at an angle of 60° from the target normal. The plasmas were produced by laser pulses with a focal spot size of

55µm, pulse energy of 60mJ, and different pulse durations between 120ps and 4ns corresponding to intensities between 4.1×10^{11} and 1.4×10^{13} W cm^{-2}.

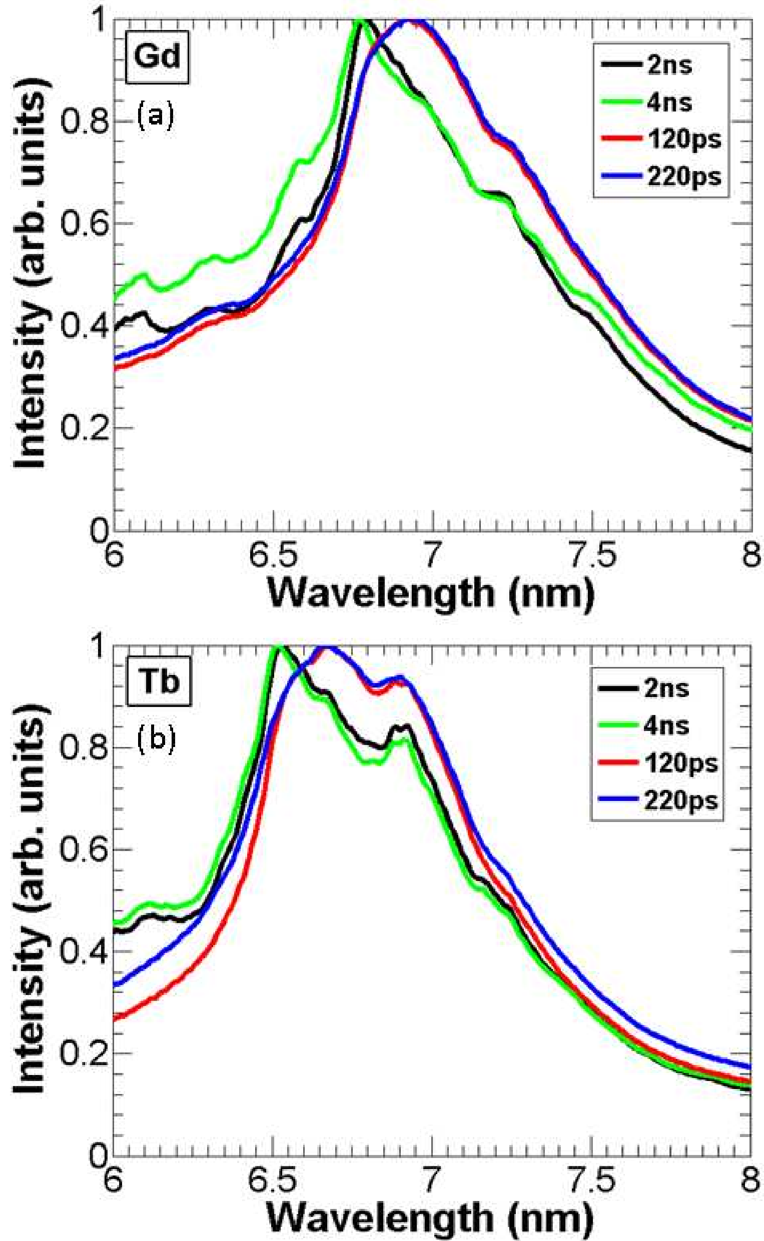

Figure 4-2. Measured Gd (a) and Tb (b) spectra corresponding to plasmas generated by 60mJ pulses with different pulse durations. The laser focus spot size on target was 55 µm. The spectra were measured at 60 degrees from the target normal.

As shown in Figure 4-2 (a), the peak emission wavelength of plasmas created with 120ps and 220ps pulses was measured to be around 6.93 nm, and that for the 2ns and 4ns pulses was measured to be near 6.78nm. Shift of the peak emission was also observed when we changed laser pulse energy from 20mJ to 80mJ while keeping laser pulse duration and focal spot size constant. Spectra of the emission from Tb plasmas acquired under the same laser irradiation conditions are shown in Figure 4-2 (b). They demonstrate a similar trend to that observed for the Gd plasma emission, with plasmas generated by shorter pulses emitting at longer wavelengths. The wavelength of the Tb plasma emission is shorter than that of the Gd plasma emission: the peak wavelength of the spectrum from plasmas produced by the same laser pulse durations was measured to be near 6.67nm for the plasmas created with the picosecond pulses, and 6.52nm for nanosecond pulses respectively.

As noticed above, the peak emission shifts to longer wavelength as the laser pulse duration is shortened. This wavelength shift is caused by the increase of the mean ion charge that occurs when the pulse duration becomes shorter and the irradiation intensity increases. The model simulation results shown in Figure 4-3 (a) (b) indicate that the dominant ions in the Gd plasmas created using 2ns laser pulses are Rh-like Gd^{19+} and Ru-like $Gd^{20+}$and Figure 4-4 (a) and (b) show the simulated temperature of the plasma created with 2ns and 220ps laser pulses respectively**.** The laser pulse energy is 60 mJ and laser spot size is 55 µm for both pulse durations for the simulation. The plasma created by the 2ns laser pulses is computed to have a maximum electron temperature of ~ 110eV, while the plasma created by 220ps laser pulses has a maximum temperature of ~ 300eV. The higher plasma temperature in the latter case causes an increase in the ion charge state, Z. Since the mean wavelength of the n=4-4 transitions in Gd ions ($Z > 18+$)

shifts to longer wavelength as ion charge increases [4,26], the spectral emission of Gd plasmas created using picosecond laser pulse shifts accordingly with respect to the emission of Gd plasmas created using nanosecond laser pulses.

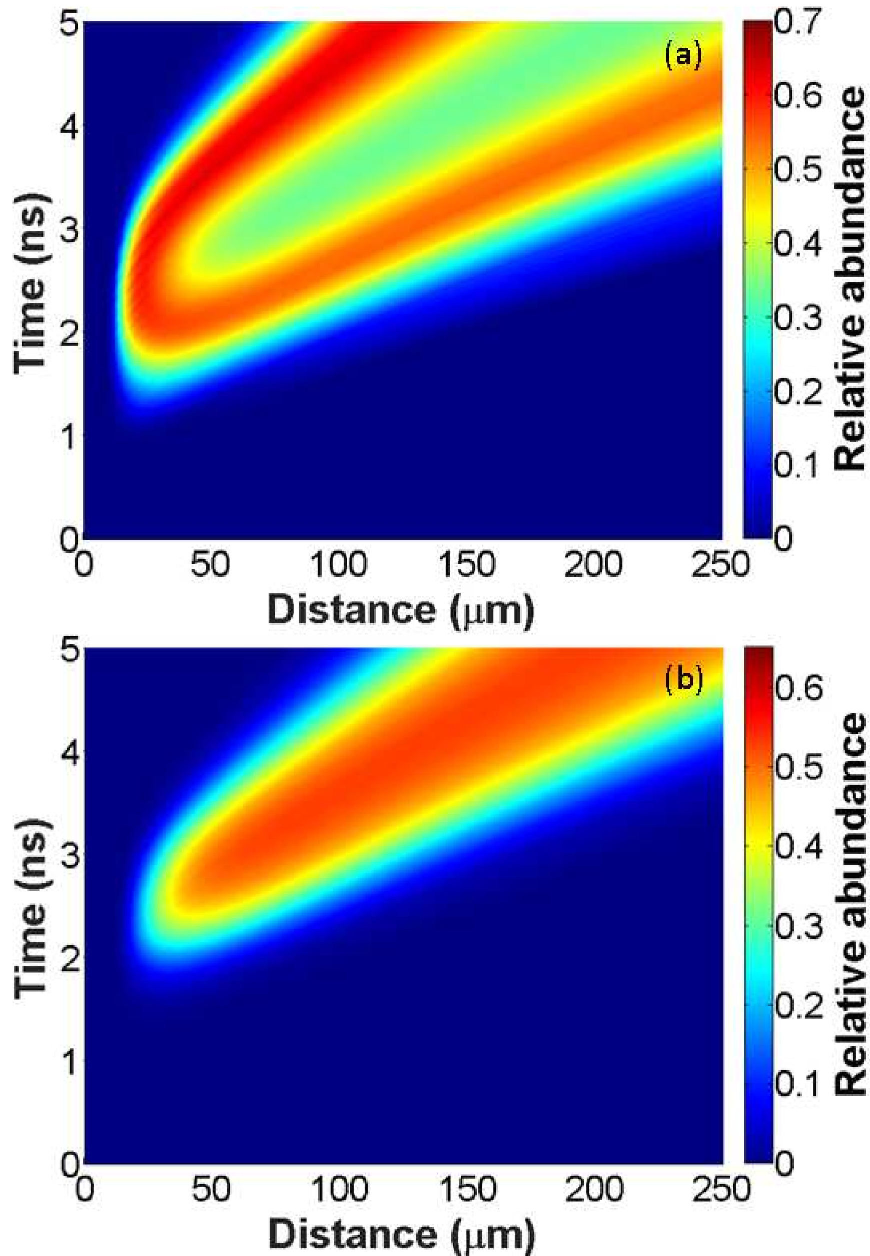

Figure 4-3. Simulated the relative ion abundance of: (a) Rh-like Gd^{19+}; (b) Ru-like Gd^{20} for a Gd plasma created with a 60 mJ pulse of 2ns duration spot 55 µm FWHM spot size. The horizontal axis represents the distance from the target surface and the vertical axis represents the time from the beginning of the laser pulse.

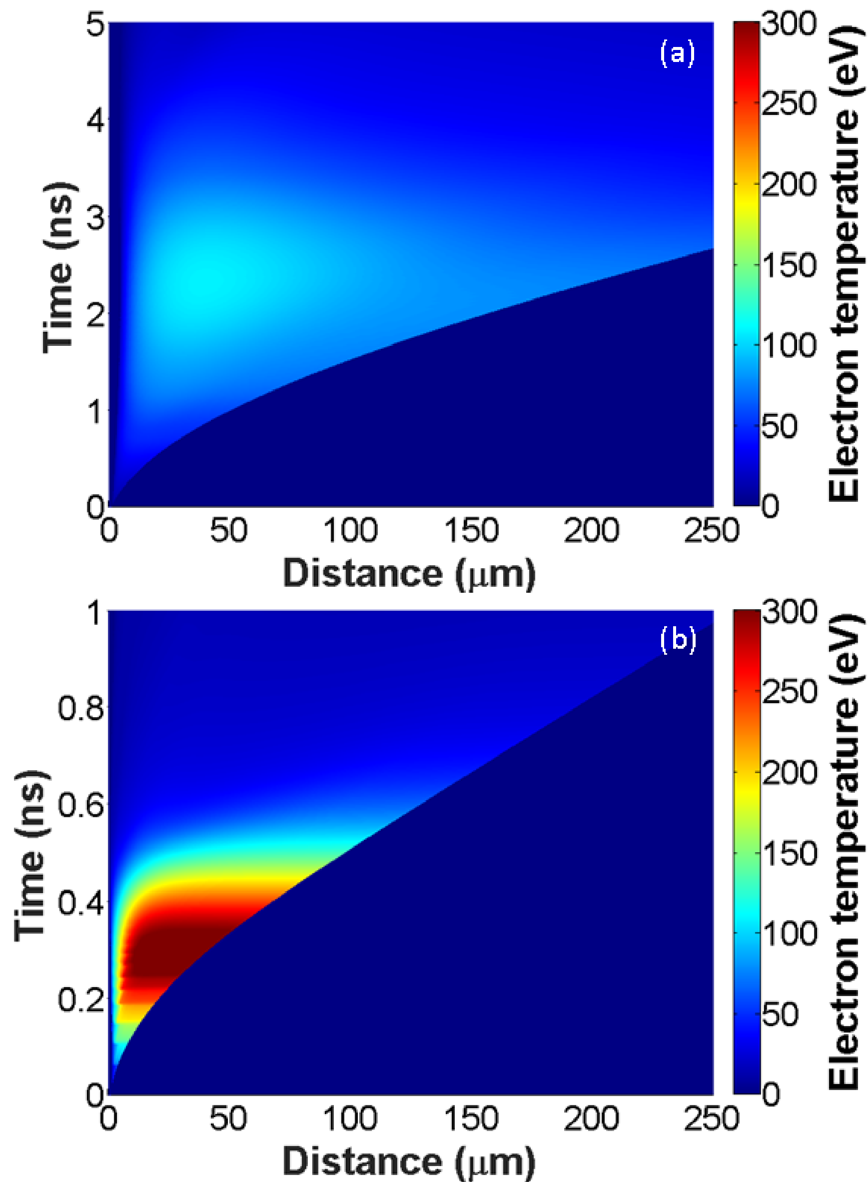

Figure 4-4. Simulated plasma temperature (eV) for plasmas created by 2ns (a) and 220ps (b) laser pulses. The laser pulse energy is 60 mJ and the focus spot size is 55 μm.

This somewhat unusual effect of decreased photon energy with increased Z is due to the increased splitting of n=4 ground state when the Gd ion is ionized from the closed shell Pd-like ionization state to higher ionization states according to our simulation. The spectra obtained with the picosecond laser pulse durations are also observed to be broader than those obtained with the nanosecond laser pulses. Two different facts contribute to this effect. First, the hotter

picosecond plasma has a broader distribution of ion species, which in combination emit over a broader bandwidth. Second, each of these more highly ionized 4d ions (Z > 18+) emit over a broader spectral range. The broadening and spectral shift of the Tb plasma to longer wavelengths for shorter laser pulses (Figure 4-2 (b)) is due to the same physics that causes the similar phenomena observed in Gd.

BEUV spectral emission was also measured at angles of 20° and 85° from the target normal for two laser pulse durations of 220ps, 2ns to study the angular dependence of the BEUV spectral emission. A laser pulse energy 60 mJ and focal spot size of 55 µm were also employed for these measurements. The spectral emission from these plasmas is similar for all angles as shown in Figure 4-5 (a), (b).

The above spectroscopic studies correspond to the emission from the entire Gd plasma. In order to better understand the origin of the emission, a 20µm slit was used to define the plasma region from which the spectrometer gathers the light. The slit was placed about 3 mm away from the plasma and was mounted on a motorized stage. The plasma was created by focusing 220ps, 60mJ driver laser pulses into 55 µm spot on Gd planar target. The slit was moved in 20 µm steps along the direction normal to the target surface to allow the emission from a 20µm slice of Gd plasma to be recorded by the spectrometer on each step. The results are shown in Figure 4-6. In order to verify the validity of the measurement, we summed the spectra corresponding to all plasma regions to form a whole-plasma spectrum and compared it with the 220ps spectra in Figure 4-2 (a) acquired without the slit. The two spectra match very well.

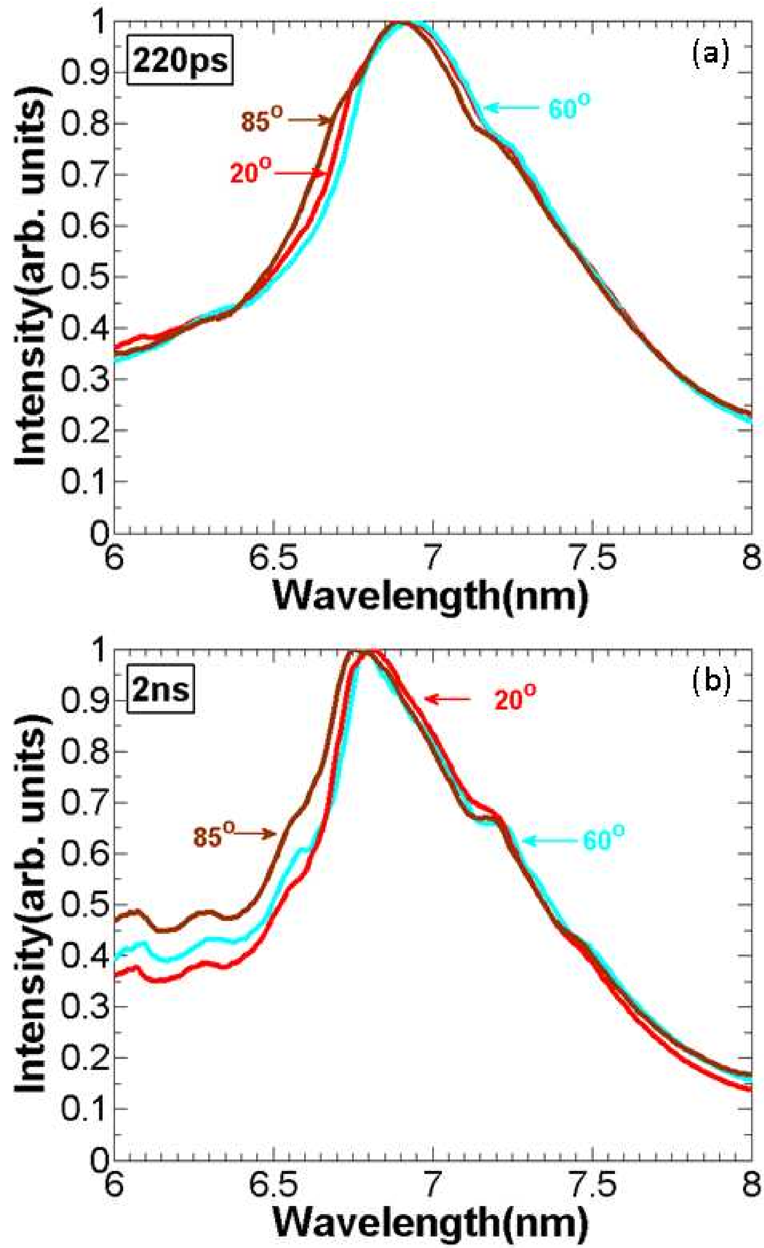

Figure 4-5. Measured spectral emission of the Gd plasmas at observation angles of 85° (brown), 60° (cyan) and 20° (red) from the target normal for three pulse durations 220ps (a), 2ns (b). The pulse energy is 60 mJ and focal spot size is 55 µm.

As seen in the Figure 4-6 (a), as the distance from the target surface increases, the spectral emission initially becomes stronger and peaks at about 50 µm from the surface. At larger distances the spectral emission becomes weaker. In Figure 4-6 (b) the spectra corresponding to

each plasma location are normalized to allow for a better comparison of the spectral distributions. The spectral width becomes narrower as the distance increases. As the slit is moved from 50 µm to 150 µm, the peak of the spectrum also shifts towards shorter wavelengths from 6.98 nm to 6.80 nm.

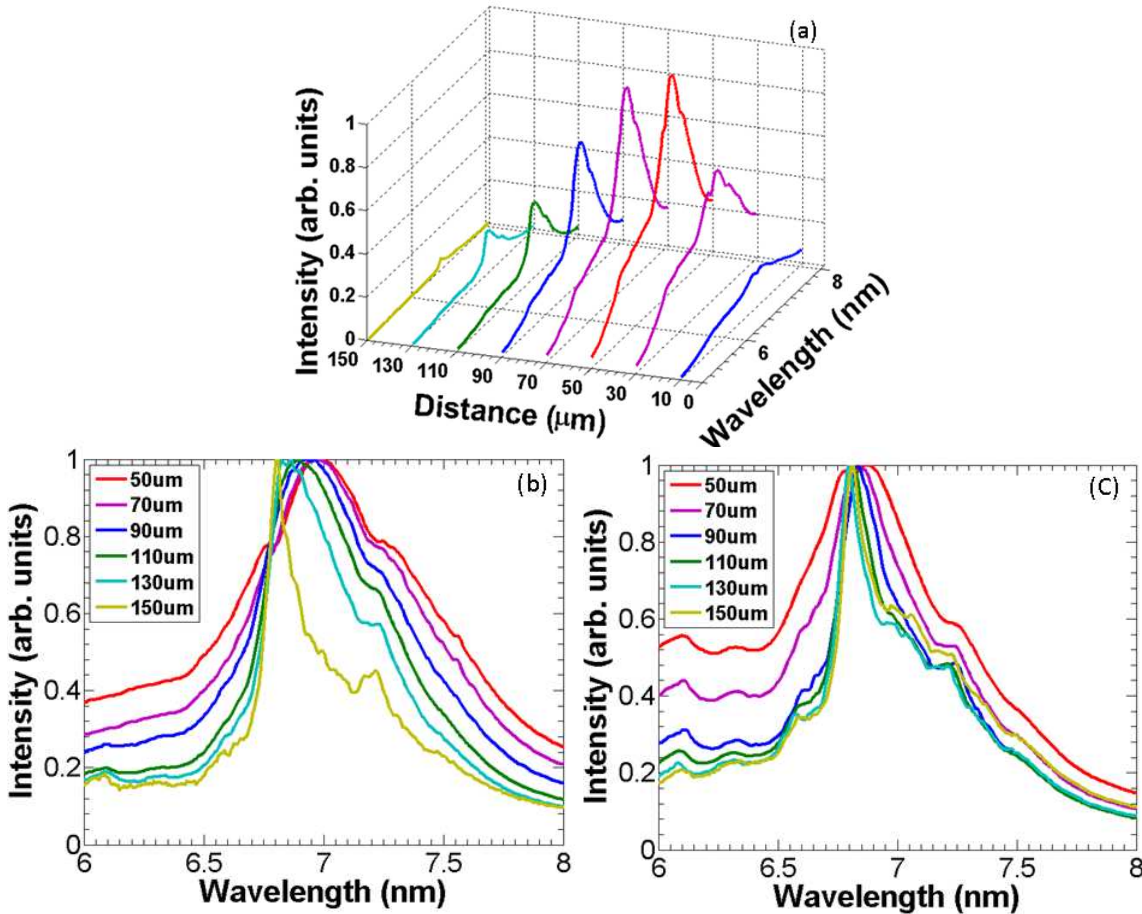

Figure 4-6. (a) Spectral emission of the Gd plasma produced with 220ps laser pulse at different distances from the target surface. (b) Normalized spectral emission of the Gd plasma produced with 220ps laser pulse at different distances from the target surface. (c) Normalized spectral emission of the Gd plasma produced with 4ns laser pulse at different distances from the target surface. The plasmas were created by focusing 220ps/4ns, 60mJ pulses into a 55 µm spot.

This occurs because as the slit is placed to collect light from distances far from the target the contribution to the emission originates from the lower charge ions. The n=4-4 transitions of Pd-

like Gd^{18+} ions and the n=5-1 transitions of lower charge ions contribute to the shift towards lower wavelengths. In contrast, from 50 μm to 150 μm the shift of the peak of the spectrum for plasma produced with 4ns laser pulse is much smaller as demonstrated in Figure 4-6 (c). Figure 4-6 (b), (c) show that the plasma produced with the picosecond pulses have a significantly larger spectral shift of the BEUV emission as a function of distance from the target, as compared with the plasmas generated by the nanosecond pulses, broadening the spectra.

Figure 4-7. (a) shows the spatial distribution of the spectral emission from a Gd plasma produced with 220ps laser pulse. The spatial distribution of the spectral emission is formed by stacking the spectra obtained at different distances along the target normal. The spatial intensity profile of the emission near λ=6.74 nm, which is obtained by spectrally integrating the emission falling in the reflectivity band of the La/B_4C mirror used for plasma imaging in section VI, is shown in Figure 4-7 (b). The intensity peak of the Gd plasma emission is observed to occurs at 50 μm from the target surface. This measured spatial intensity profile matches that obtained from plasma imaging under the same laser condition discussed in section VI. The good agreement of the integral of the measured spatial distribution of the spectral emission with the spatial profile of the source intensity obtained from imaging the plasma under the same laser condition (Figure 4-7 (b)) validates the measurements.

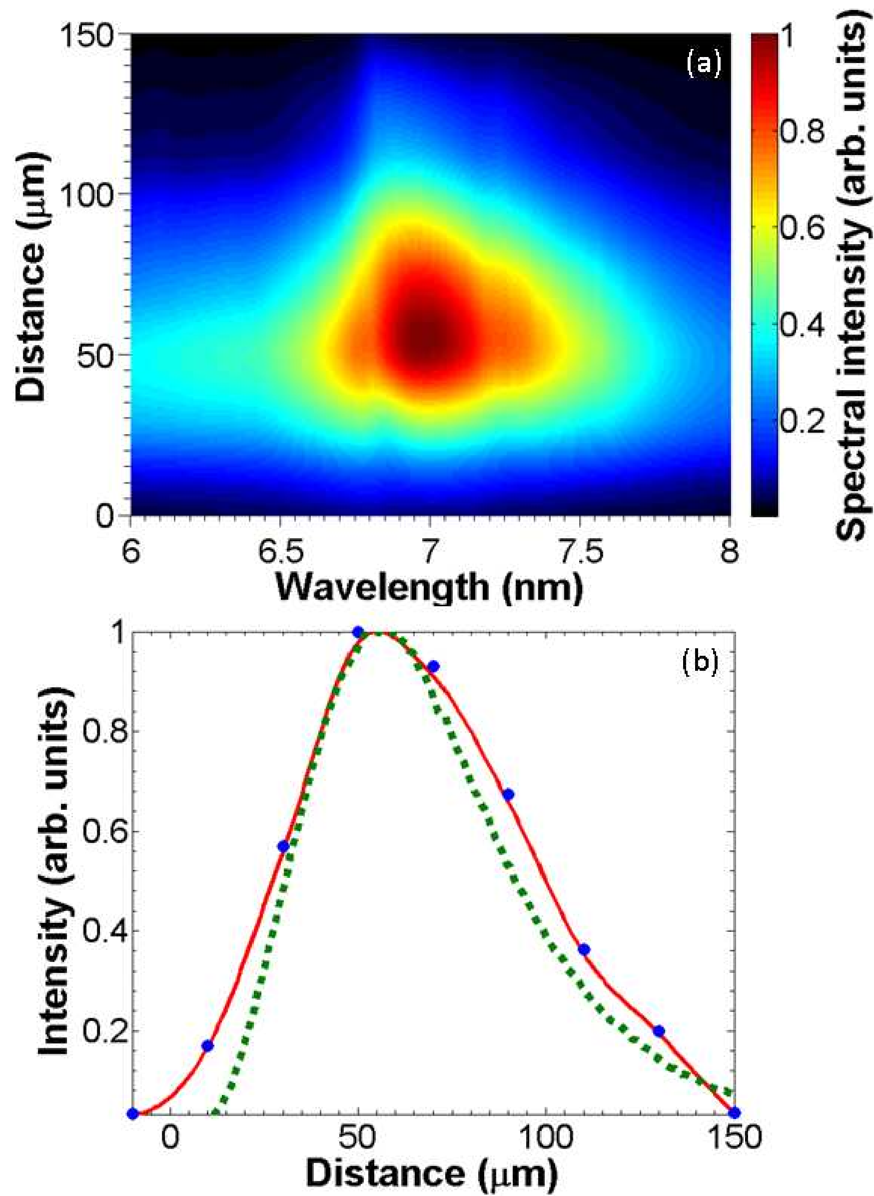

Figure 4-7. (a) Spatially resolved spectral profile of Gd plasma produced with 220ps laser pulse formed by combining the spectra shown in Figure 4-6 (a). Cubic interpolation between spatial steps is used to smooth the profile. (b) The spatial intensity profile of the emission near λ=6.7 nm obtained from (a). Original data shown as blue solid dots, and interpolation shown as a red solid line compared with the spatial intensity profile of Gd plasma emission near λ = 6.7nm obtained from the plasma image in Section VI obtained (green dashed line) for the same laser irradiation conditions.

4.4 Angular Distribution of the BEUV Emission

The angular distribution of the BEUV emission shown in Figure 4-8 was obtained using an array of energy-monitors covering one entire quadrant. The total BEUV yield was obtained by fitting the measured data with a 2nd order polynomial and integrating this angular distribution of the emission over a solid angle of 2π. The Gd plasma emission was assumed to be symmetric about the central axis of the plasma. Irradiation parameters including the pulse duration, pulse energy and focal spot size were scanned when measuring the angular distribution of the BEUV emission. This allowed us to investigate how the irradiation parameters influence the angular distribution of the emission and to more precisely determine the conversion efficiency by integrating the real angular distribution of the emission over 2π instead of assuming an isotropic distribution as done in previous measurements [11,13]. Figure 4-8 (a) shows a comparison of the angular distributions of emission for different laser pulse durations while the 60 mJ laser pulse energy and 55 μm focal spot diameter remained constant. In Figure 4-8 (b) each angular intensity distribution is normalized to the same maximum to facilitate the comparison of the shape of the angular distribution.

The first observation is that the emission decreases as the angle respect to the target normal increases, which is also observed for Tin LPP [27]. Also the angular distribution of the emission corresponding to the shorter pulse duration is more convex. This is possibly the result of the dynamic Doppler effect being more prominent in the hotter plasmas of the picosecond pulses, which shifts the emitting line frequencies due to velocity gradients in the accelerated plasma.

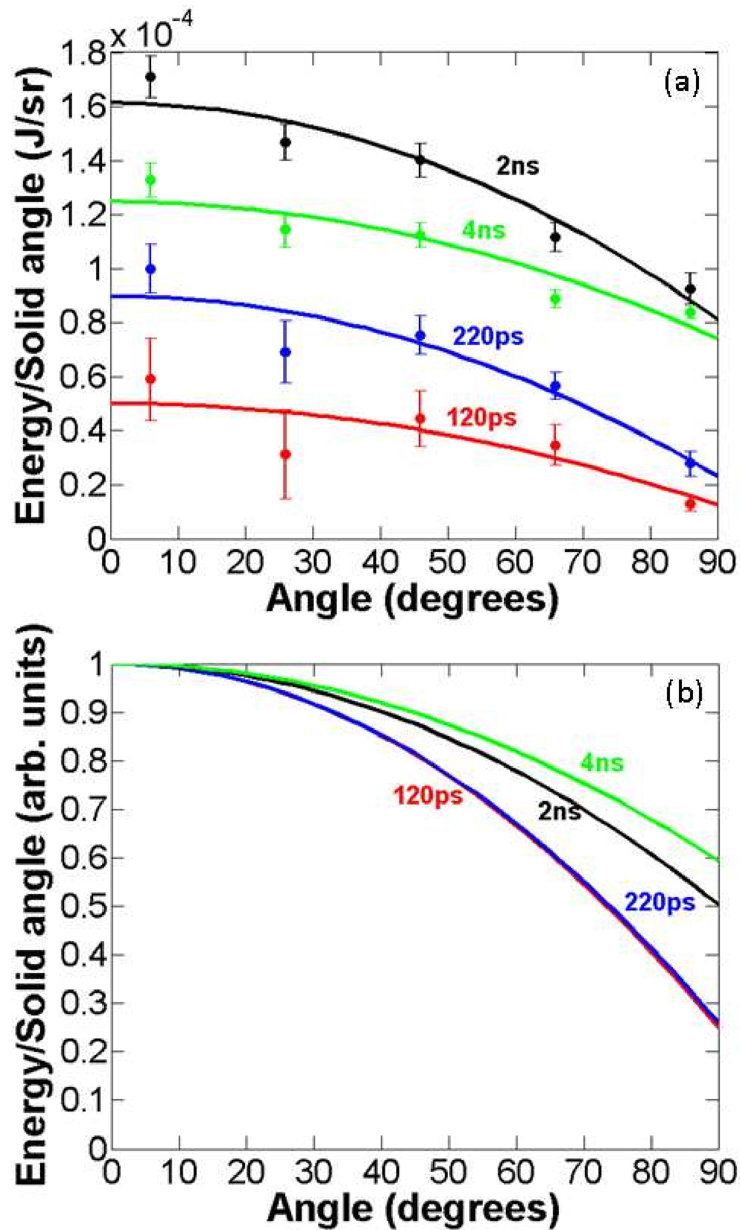

Figure 4-8. (a) Measured angular distributions of the BEUV emission from Gd plasmas created with laser pulse durations of 120ps FWHM (red), 220ps FWHM (blue), 2ns FWHM (black) and 4ns FWHM (green) while the laser pulse energy remained 60 mJ and the focal spot size remained 55 µm FWHM. The curves are 2nd order polynomial fits to the data; (b) Fits of the data from (a) normalized for the purpose of comparison of the angular distribution corresponding to different pulse duration.

This makes the resonant absorption lines more transparent in the direction normal to the target than parallel to the target surface. The average influence of this effect is small, as it affects only the strongest resonance lines while the majority of other 4-4 lines remain close to optical thin. In

addition, a comparison of the angular distributions for focal spots of 30 μm FWHM and 55 μm FWHM shows that the focal spot size does not greatly affect the angular distribution of the emission

4.5 Conversion Efficiency Measurements

Figure 4-9 shows the measured CE of laser pulse energy into λ=6.7nm emission energy for both Gd (Figure 4-9 (a)) and Tb (Figure 4-9 (b)) plasmas for different laser intensities ranging from 1.4×10^{11} W/cm^2 to 6.1×10^{13} W/cm^2. Each curve was obtained by varying the laser pulse energy while keeping all other parameters constant. The highest CE for Gd, 0.47%, was obtained at a laser intensity of 6.8×10^{11}W/cm^2 with a laser pulse duration of 2ns. Both the maximum CE value and the laser intensity at which the maximum CE occurs are similar to those reported in in previous modeling work [28]. It should be noticed that if the CE were to be computed using the data from a single detector placed at 45 degrees assuming an isotropic distribution, the CE values would be overestimated by up to 28%. The discrepancy between CE values obtained from measuring the angular distribution and assuming an isotropic angular distribution increases as the laser pulse becomes shorter because in this case the angular distribution of the emission becomes more convex as shown in Figure 4-8. As shown in Figure 4-4, the Gd plasmas created using the 220ps laser pulses are much hotter than those created with the 2ns laser pulse, which causes the spectral emission of the Gd plasma to shift to more highly ionized species and away from the peak of responsivity of the energy monitors. As discussed in Section III the spectra of the Gd plasmas created using 2ns and 4ns duration pulses overlap better with the responsivity

of the energy monitors used in the CE measurements. Additionally, in the nanosecond regime the observed CE corresponding to the case of laser focal spot size of 55 μm FWHM is higher than that with focal spot size of 30 μm FWHM, which was predicted by modeling work [29]. This is because the smaller plasma created by the latter cools faster due to the larger expansion heat loss [10], making the ratio of the radiative lifetime to hydrodynamic cooling time smaller.

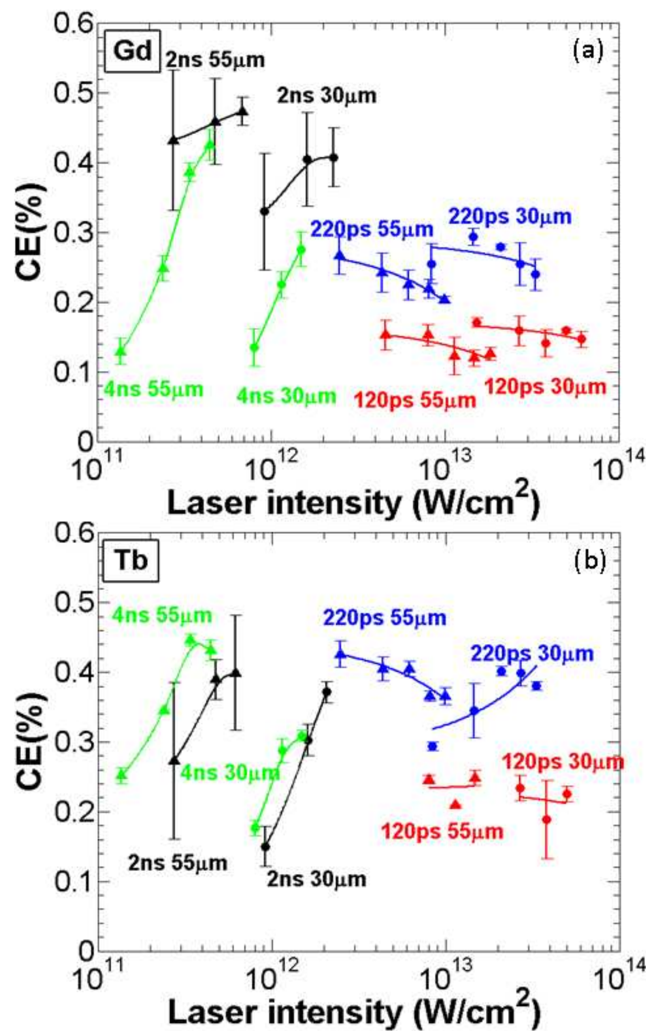

Figure 4-9. Measured dependence of CE on laser intensity for (a) Gd and (b) Tb plasmas. The CE was measured for four pulse durations: 120ps FWHM (red), 220ps FWHM (blue), 2ns FWHM (black), and 4ns FWHM (green) for two different spot sizes: 30 um FWHM (solid dots) and 55 um FWHM (solid triangles) as a function of laser pulse energy. For each condition (pulse duration, pulse energy, focal spot size), the mean of 5 shots is shown. The BEUV emission energy for each shot was computed by integrating the angular distribution over 2π solid angle.

The measured dependence of the CE of the Tb plasma on laser intensity is similar to that of the Gd plasma, except that the CE of the Tb plasma for the picosecond laser pulse is higher than the CE of the Gd plasma created with the same laser pulse duration. The reason for this is that in the case of the picosecond laser pulse the spectral emission of the Tb plasma has a better overlap with the responsivity of the energy monitors than that of the Gd plasma emission. The best CE for the Tb plasma was measured to be 0.45% which was obtained with a driver laser intensity of 3.4×10^{11} W/cm^2. These results indicate that the precise responsivity of the BEUV energy monitors plays a significant role in the measured conversion efficiency and must be taken into account when comparing the results between different experiments.

4.6 Plasma Imaging

Plasma imaging allowed us to determine the size of the BEUV emitting plasma region and the pattern of the Gd plasma expansion under different irradiation conditions. Frontview and sideview images of the Gd plasmas at BEUV wavelength were obtained for different laser focus spot sizes and pulse durations. With a laser pulse energy of 60 mJ, a focal spot size of 55µm FWHM, and laser pulse durations varying from 220ps to 4ns, we obtained the frontview and sideview images as shown in Figure 4-10. The BEUV emitting region of the Gd plasmas has a lateral dimension (parallel to target surface) similar to the laser spot size and is insensitive to the laser pulse duration. The sideview Gd plasma images in Figure 4-11 were taken for laser focus spot sizes of 30µm, 55µm and 85µm. For each laser focus spot size the laser pulse duration was varied, while the pulse energy remained 60 mJ. As the size of the laser focus decreases, the

plasma size in the lateral direction decreases and the lateral expansion of the plasma becomes stronger. In the direction normal to target, the size of the BEUV emitting plasma shrinks slightly as the laser focal spot size decreases. The sideview images show the reflection of the Gd plasma emission from the target surface, as seen in Figure 4-10. We determined the location of the target surface using the reflected BEUV light from the target surface. The peak of the BEUV emitting plasma region is measured to be located about 50 µm from the surface of target and is rather insensitive to the laser pulse duration. Figure 4-12 shows a simulated BEUV emission density map for a Gd plasma created focusing a 2ns, 60mJ laser pulse into a 55 µm diameter spot. In the simulated emission density map we can see the BEUV emission peak is also located about 50 µm from the target and the size of the BEUV emitting plasma region in the normal direction is about 85 µm FWHM, which matches well with the experimental image taken under the same laser conditions.

4.7 Summary

In conclusion, we conducted both experiments and simulations to study the emission of laser produced Gd and Tb plasmas at wavelengths near 6.7nm. All the measurements were conducted focusing laser pulses of durations ranging from 120ps to 4ns from a single λ=1030nm laser onto slab target. We measured the spectral emission, the angular distribution of the emission, the conversion efficiency, and the plasma source size for different irradiation conditions. Model simulations show that in the Gd plasmas created at an irradiation intensity of 8.2×10^{11} W cm^{-2} using 2ns laser pulses the dominant ions are Rh-like Gd^{19+} and Ru-like Gd^{20+}.

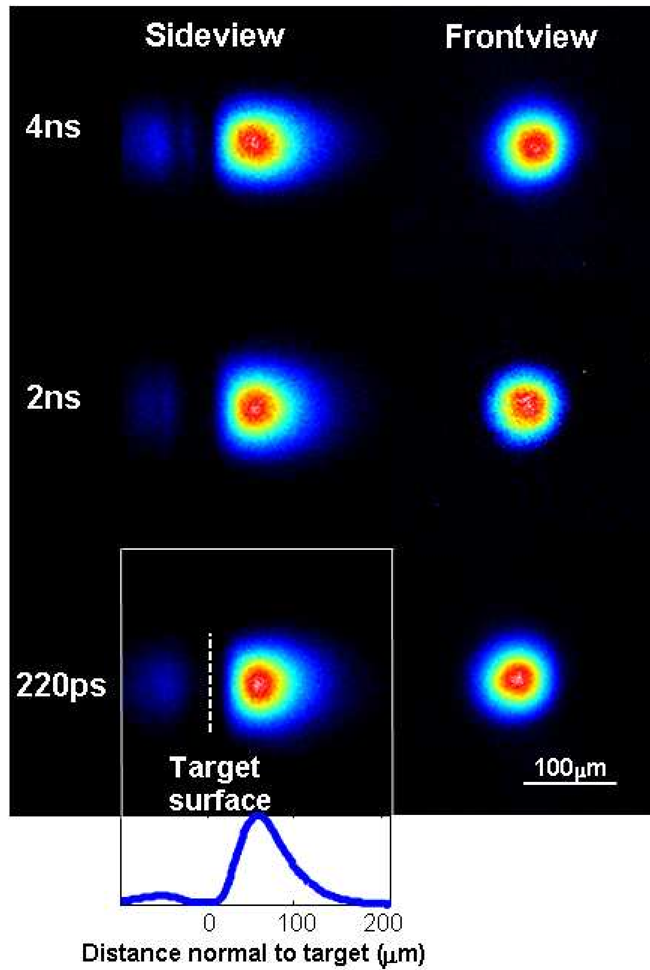

Figure 4-10. Plasma images of BEUV emitting region from Gd plasmas obtained focusing 60mJ laser pulses into a spot diameter of ~55 μm (FWHM). The left column shows sideview plasma images viewed parallel to the target surface. The images in the right column are frontview plasma images taken in the direction normal to target surface. Sideview and frontview plasma images corresponding to 220ps, 2ns and 4ns FWHM laser pulse durations are shown. Each plasma image is normalized to its maximum intensity. The inset plot shows the position of target surface (dashed line) determined by dividing the distance between the maxima of the plasma emission and its reflection from the target surface. The inset also shows the intensity profile of the sideview image.

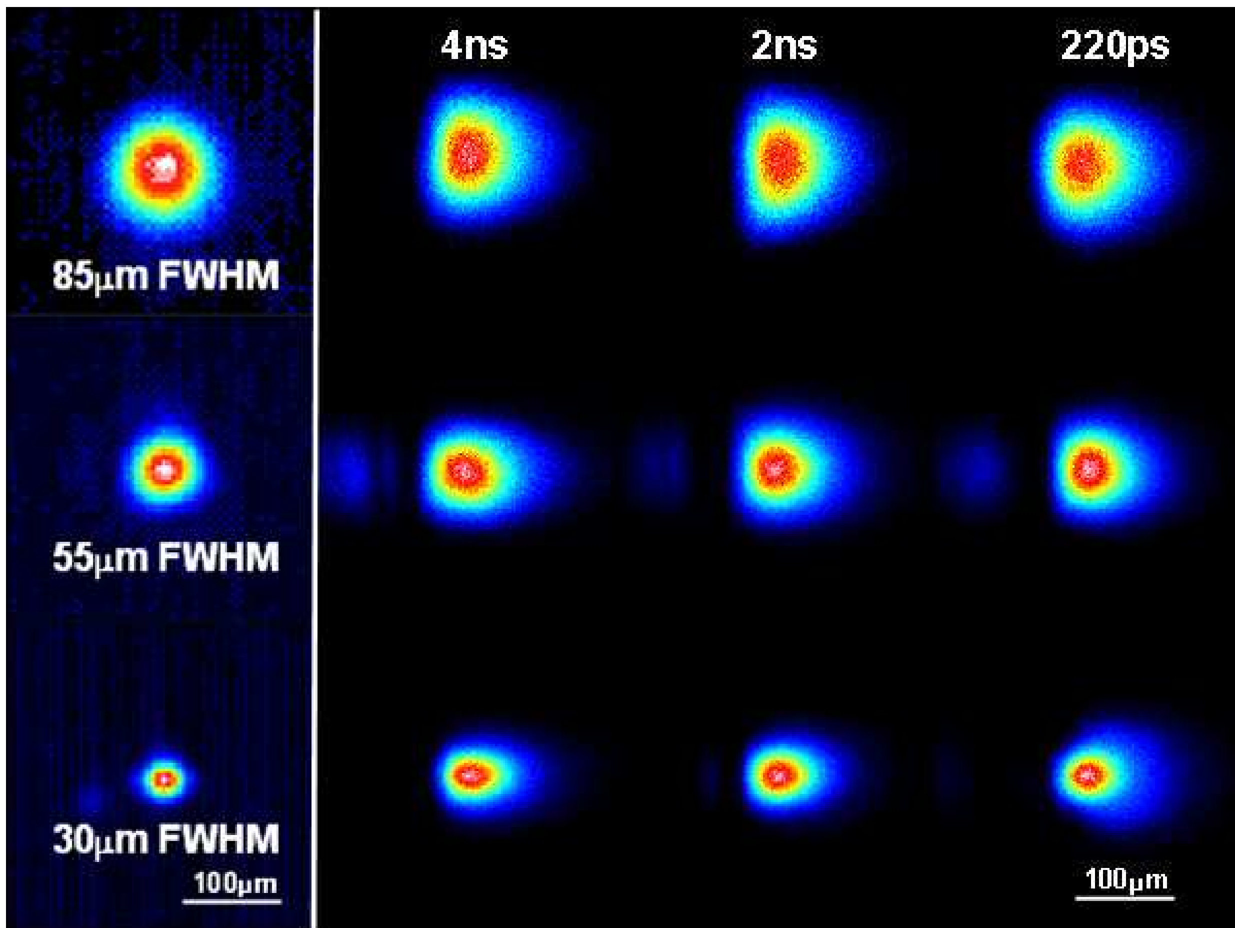

Figure 4-11. Sideview plasma images corresponding to different laser focus spot sizes and pulse durations. The laser was focused into spots with diameters of ~85 µm, ~55 µm and ~30 µm (FWHM). The first column shows the laser spot focus on target. Each row on the right shows sideview plasma images taken with laser pulse durations of 4ns, 2ns and 220ps FWHM (left to right). The pulse energy was 60 mJ for all images. Each image is normalized to its maximum intensity.

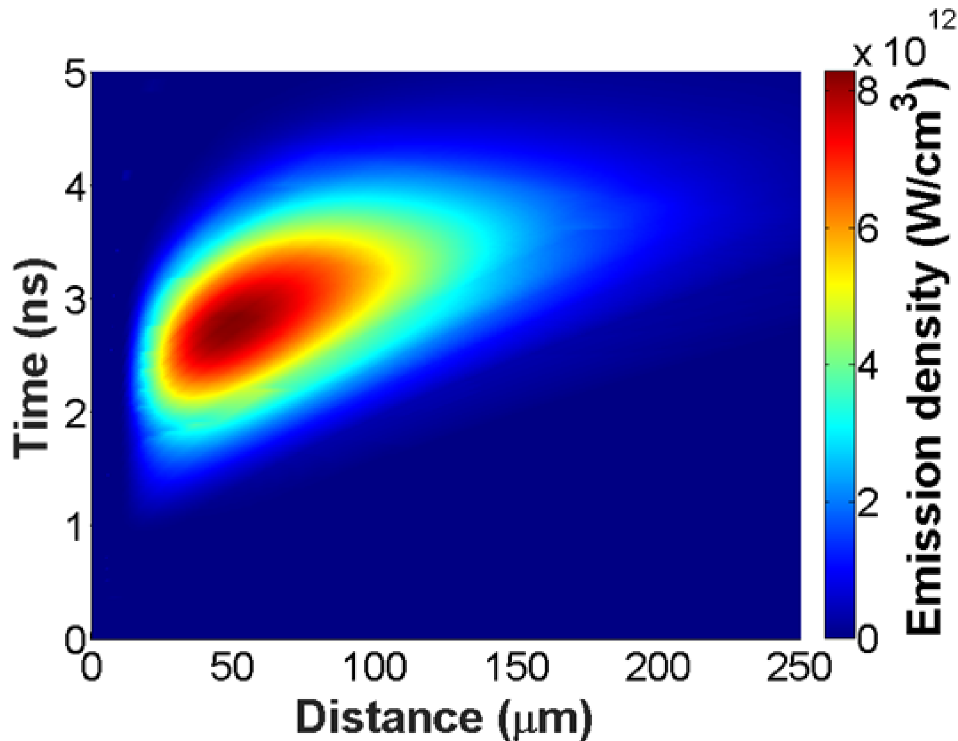

Figure 4-12. Simulated spatial-temporal distribution of the BEUV emission density (W/cm^3) of a Gd plasma created by focusing a 2ns, 60mJ laser pulse into a 55 µm FWHM spot.

The spectral measurements shows that the wavelength of the peak spectral emission shifts from 6.78 nm to longer wavelength and the spectrum becomes broader when the laser pulse duration is reduced from 2-4ns to 120-220ps. The associated increase in irradiation intensity causes the plasma emission to originate from more highly ionized species whose transitions are increasingly mismatched with the responsivity of the energy monitor centered at 6.74 nm, causing a decrease in the amount of BEUV emission collected by the energy monitors. The BEUV emission is measured to decrease as a function of angle from the target normal with the angular distribution of BEUV emission becoming more convex when pulse duration decreases from nanoseconds to hundreds of picoseconds. The conversion efficiency for different irradiation conditions was determined by integrating the measured angular distribution of the BEUV emission. The highest conversion efficiency of 0.47% was obtained for a Gd plasma generated with a laser intensity of

$6.8 \times 10^{11} W/cm^2$ with a pulse duration of 2ns and a laser spot size on target of 55µm FWHM. However, it should be noticed that the optimum laser pulsewidth for maximum CE significantly depends on the center wavelength of the responsivity of the energy monitors that are used. This is because given the rather abrupt spectral profile of the BEUV emission, the laser pulsewidth-dependent overlap between the BEUV emission band and the responsivity of the energy monitors can be a dominant effect in determining CE. A similar maximum conversion efficiency of 0.45% was measured for the Tb plasmas irradiated under similar conditions. The measurement of the plasma emission conducted using a diode array indicates that if the CE would have been estimated using single diode and assuming an isotropic distribution its value would have been overestimated by up to 28%. The results illustrate the importance of performing angularly resolved measurements of the plasma emission to compute CE. For a smaller laser spot size, the lateral expansion of the plasma is stronger, resulting in faster cooling and lower conversion efficiency. The size of the BEUV emitting region is measured to be very similar to the laser spot size and the peak of the BEUV emitting plasma region is found to take place at a distance of about 50 µm from the target surface, in agreement with simulations. The measured CE by no mean represents the maximum that can be obtained near this wavelength since our atomic calculations estimate that much higher values, about 5 percent, could ultimately be obtained in ideally tailored plasmas. Temporal pulse shaping and different target designs could be employed for improvement of conversion efficiency in the future.

References

1. D. C. Brock and G. E. Moore, *Understanding Moore's Law: Four Decades of Innovation* (Chemical Heritage Foundation, 2006).

2. S. Wurm, "EUV lithography: progress, challenges, and outlook," 30th Eur. Mask Lithogr. Conf. **9231**, 923103 (2014).

3. A. Pirati, R. Peeters, D. Smith, S. Lok, A. Minnaert, M. van Noordenburg, J. Mallmann, N. Harned, J. Stoeldraijer, C. Wagner, C. Zoldesi, E. van Setten, J. Finders, K. de Peuter, C. de Ruijter, M. Popadic, R. Huang, M. Lin, F. Chuang, R. van Es, M. Beckers, D. Brandt, N. Farrar, A. Schafgans, D. Brown, H. Boom, H. Meiling, and R. Kool, "Performance overview and outlook of EUV lithography systems," Extrem. Ultrav. Lithogr. VI **9422**, 94221P (2015).

4. S. S. Churilov, R. R. Kildiyarova, A. N. Ryabtsev, and S. V Sadovsky, "EUV spectra of Gd and Tb ions excited in laser-produced and vacuum spark plasmas," Phys. Scr. **80**(4), 2–8 (2009).

5. D. Kilbane and G. O'Sullivan, "Extreme ultraviolet emission spectra of Gd and Tb ions," J. Appl. Phys. **108**(10), 1–6 (2010).

6. N. Mojarad, J. Gobrecht, and Y. Ekinci, "Beyond EUV lithography: A comparative study of efficient photoresists' performance," Sci. Rep. **5**, 1–7 (2015).

7. I. A. Makhotkin, E. Zoethout, E. Louis, A. M. Yakunin, S. Müllender, and F. Bijkerk, "Wavelength selection for multilayer coatings for lithography generation beyond extreme

ultraviolet," J. Micro/Nanolithography, MEMS, MOEMS **11**(4), 040501 (2012).

8. D. S. KUZNETSOV, A. E. YAKSHIN, J. M. STURM, R. W. E. VAN DE KRUIJS, E. LOUIS, and F. BIJKERK, "High-reflectance La / B-based multilayer mirror for 6 . x nm wavelength," Opt. Lett. **40**(16), 3778–3781 (2015).

9. H. Ohashi, T. Higashiguchi, B. Li, Y. Suzuki, M. Kawasaki, T. Kanehara, Y. Aida, S. Torii, T. Makimura, W. Jiang, P. Dunne, G. O'Sullivan, and N. Nakamura, "Tuning extreme ultraviolet emission for optimum coupling with multilayer mirrors for future lithography through control of ionic charge states," J. Appl. Phys. **115**(3), (2014).

10. G. J. Pert and S. A. Ramsden, "Population inversion in plasmas produced by picosecond laser pulses," Opt. Commun. **11**(3), 270–273 (1974).

11. T. Cummins, T. Otsuka, N. Yugami, W. Jiang, A. Endo, B. Li, C. O'Gorman, P. Dunne, E. Sokell, G. O'Sullivan, and T. Higashiguchi, "Optimizing conversion efficiency and reducing ion energy in a laser-produced Gd plasma," Appl. Phys. Lett. **100**(6), (2012).

12. T. Higashiguchi, T. Otsuka, N. Yugami, W. Jiang, A. Endo, B. Li, D. Kilbane, P. Dunne, and G. O'Sullivan, "Extreme ultraviolet source at 6.7 nm based on a low-density plasma," Appl. Phys. Lett. **99**(19), 97–100 (2011).

13. K. Yoshida, S. Fujioka, T. Higashiguchi, T. Ugomori, N. Tanaka, H. Ohashi, M. Kawasaki, Y. Suzuki, C. Suzuki, K. Tomita, R. Hirose, T. Ejima, M. Nishikino, A. Sunahara, E. Scally, B. Li, T. Yanagida, H. Nishimura, H. Azechi, and G. O'Sullivan, "Efficient extreme ultraviolet emission from one-dimensional spherical plasmas produced by multiple lasers," Appl.

Phys. Express **7**(8), (2014).

14. T. Higashiguchi, B. Li, Y. Suzuki, M. Kawasaki, H. Ohashi, S. Torii, D. Nakamura, A. Takahashi, T. Okada, W. Jiang, T. Miura, A. Endo, P. Dunne, G. O'Sullivan, and T. Makimura, "Characteristics of extreme ultraviolet emission from mid-infrared laser-produced rare-earth Gd plasmas," Opt. Express **21**(26), 31837 (2013).

15. C. O'Gorman, T. Otsuka, N. Yugami, W. Jiang, A. Endo, B. Li, T. Cummins, P. Dunne, E. Sokell, G. O'Sullivan, and T. Higashiguchi, "The effect of viewing angle on the spectral behavior of a Gd plasma source near 6.7 nm," Appl. Phys. Lett. **100**(14), 2010–2014 (2012).

16. A. V Vinogradov and V. N. Shlyaptsev, "Amplification of ultraviolet radiation in a laser plasma," Sov. J. Quantum Electron. **13**(11), 1511–1515 (1983).

17. Y. V. Afanas'ev, V. P. Avtonomov, N. G. Basov, G. Korn, G. V. Sklizkov, and V. N. Shlyaptsev, "Radiative transport in a laser plasma," J. Sov. Laser Res. **10**(1), 1–13 (1989).

18. M. C. Marconi, C. H. Moreno, J. J. Rocca, V. N. Shlyaptsev, and A. L. Osterheld, "Dynamics of a microcapillary discharge plasma using a soft x-ray laser backlighter," Phys. Rev. E - Stat. Physics, Plasmas, Fluids, Relat. Interdiscip. Top. **62**(5), 7209–7218 (2000).

19. M. Berrill, Y. Wang, M. A. Larotonda, B. M. Luther, V. N. Shlyaptsev, and J. J. Rocca, "Pump pulse-width dependence of grazing-incidence pumped transient collisional soft-x-ray lasers," Phys. Rev. A - At. Mol. Opt. Phys. **75**(6), 1–7 (2007).

20. M. Klapisch, M. Busquet, and A. Bar-Shalom, "A new and improved version of HULLAC,"

AIP Conf. Proc. **926**(August), 206–215 (2007).

21. L. Yin, H. Wang, B. A. Reagan, C. Baumgarten, E. Gullikson, M. Berrill, V. N. Shlyaptsev, and J. J. Rocca, "6.7-nm Emission from Gd and Tb Plasmas over a Broad Range of Irradiation Parameters Using a Single Laser," Phys. Rev. Appl. **6**(3), 034009 (2016).

22. A. H. Curtis, B. A. Reagan, K. A. Wernsing, F. J. Furch, B. M. Luther, and J. J. Rocca, "Demonstration of a compact 100 Hz, 0.1 J, diode-pumped picosecond laser," Opt. Lett. **36**(11), 2164 (2011).

23. B. A. Reagan, A. H. Curtis, K. A. Wernsing, F. J. Furch, B. M. Luther, and J. J. Rocca, "Development of High Energy Diode-Pumped Thick-Disk Yb:YAG Chirped-Pulse-Amplification Lasers," IEEE J. Quantum Electron. **48**(6), 827–835 (2012).

24. B. A. Reagan, C. Bamgarten, K. Wernsing, H. Bravo, M. Woolston, A. Curtis, F. J. Furch, B. M. Luther, D. Patel, C. S. Menoni, and J. J. Rocca, "1 Joule, 100 Hz Repetition Rate, Picosecond CPA Laser for Driving High Average Power Soft X-Ray Lasers," 2014 Conf. Lasers Electro-Optics - Laser Sci. to Photonic Appl. **1**(c), SM1F.4 (2014).

25. B. A. Reagan, K. A. Wernsing, A. H. Curtis, F. J. Furch, B. M. Luther, D. Patel, C. S. Menoni, and J. J. Rocca, "Demonstration of a 100 Hz repetition rate gain-saturated diode-pumped table-top soft x-ray laser," Opt. Lett. **37**(17), 3624–3626 (2012).

26. D. Kilbane and G. O'Sullivan, "Ground-state configurations and unresolved transition arrays in extreme ultraviolet spectra of lanthanide ions," Phys. Rev. A - At. Mol. Opt. Phys. **82**(6), (2010).

27. O. Morris, F. O'Reilly, P. Dunne, and P. Hayden, "Angular emission and self-absorption studies of a tin laser produced plasma extreme ultraviolet source between 10 and 18 nm," Appl. Phys. Lett. **92**(23), 18–21 (2008).

28. M. Masnavi, J. Szilagyi, H. Parchamy, and M. C. Richardson, "Laser-plasma source parameters for Kr, Gd, and Tb ions at 6.6 nm," Appl. Phys. Lett. **102**(16), 16–19 (2013).

29. T. Sizyuk and A. Hassanein, "Optimizing laser produced plasmas for efficient extreme ultraviolet and soft X-ray light sources," Phys. Plasmas **21**(8), (2014)

Chapter 5 Conclusions

In summary, we have conducted a study of LPPs that emit in the EUV / BEUV and are of interest for advanced lithography, aiming to increase understanding for improved CE. The LPPs were created by focusing a single λ=1.03 μm laser onto slab targets. Experiments were conducted creating the plasmas with a diode-pumped chirped pulse amplification Yb: YAG laser that produces an output pulse energies of up to 100 mJ. This laser can operate over a wide range of pulse duration from 120ps to 4ns, enabling us to investigate the LPPs of interest over a broad range of intensities using only one single laser to avoid inconsistencies.

To characterize the EUV/BEUV emission, a diagnosis suite was built includes an array of energy monitors, a spectrometer, a plasma imaging system and a fast EUV diode. An array of calibrated EUV/BEUV energy monitors was used to simultaneously measure the angular distribution of the in-band emission on every shot. The measurement of the EUV/BEUV emission as a function of angle from near-normal to near-grazing incidence with calibrated detectors allows for accurate CE estimate. The array of energy monitors was used to measure either EUV at λ=13.5 nm or BEUV at λ=6.7 nm by switching between Mo/Si mirror and La/B_4C mirror. The spectral emission was measured using a flat-field grazing incidence spectrometer. We used an imaging system to measure the sizes of in-band Sn /Gd LPPs EUV/BEUV emitting regions. A fast EUV diode combined with a concave Mo/Si mirror was used to measure the time resolved EUV emission from Sn LPP in the normal and tangential direction of target respectively.

A pulse synthesizer based on wave front splitting and pulse stacking was developed to generate laser pulses of arbitrary shapes. An array of liquid crystal phase retarders was used to control the amplitudes of a set of ten individual sub-pulses and the temporal separations among the sub-pulses were adjusted using sliding retroreflectors. By taking advantage of this capability we have studied the pulse shape dependence of the 13.5 nm EUV emission from Sn LPPs. The synthesized square pulses yielded the highest CE (2.7%) among all the pulse shapes studied, which included Q-switched pulses, up-ramp and down-ramp pulses. The synthesized square pulse CE was ~ 35% higher than that corresponding to Q-switched pulse. The CE was also measured to increase with pulse duration up to the maximum pulse length investigated, 4 ns. A long-lasting square pulse has the advantage of maintaining for the longest time the pre-selected optimum irradiation conditions, leading to maximum CE as well as more homogeneous angular distribution of the EUV emission. The peak wavelength of EUV spectral emission from Sn LPP was found to show a 'V' shape dependence on the irradiation intensity. This is the result of the wavelength dependence of the n=4-n=4 transitions on the ion charge state. Time-resolved EUV emission measurements along the target normal show that the lifetime of EUV emission increases with irradiation pulse energy and can outlast the irradiation pulse by several nanoseconds. However, the duration of the EUV emission along the target surface was found to be similar to the irradiation pulse duration and to be almost independent of pulse energy. This newly observed anisotropy of the EUV pulse duration is likely to the result of the competition between the rate of increase of the emitting plasma volume and the decrease of the emittance as the plasma expands and cools after the laser pulse ends. Another possible contributing cause is the creation at late times of a cold

plasma in the periphery of the irradiated spot that can absorb the EUV radiation after the laser pulse ends.

We conducted both experiments and simulations to study the emission of Gd / Tb LPPs at wavelengths near 6.7nm. We measured the spectral emission, the angular distribution of the emission, the conversion efficiency, and the plasma source size of Gd / Tb LPPs by scanning a matrix of irradiation conditions which includes pulse duration, pulse energy and focal spot size. The highest CE of 0.47% was obtained for Gd LPP generated with a laser intensity of $6.8 \times 10^{11} W/cm^2$ with a pulse duration of 2ns and a laser spot size on target of 55μm FWHM. A similar CE of 0.45% was measured for Tb LPP. Model simulations show that in the Gd LPP created at an irradiation intensity of 8.2×10^{11} W/cm^2 using 2ns laser pulses the dominant ions are Rh-like Gd^{19+} and Ru-like Gd^{20+}. The spectroscopic measurements show that the wavelength of the peak spectral emission shifts from 6.78 nm to longer wavelength and the spectrum becomes broader when the laser pulse duration is reduced from 2-4ns to 120-220ps. The shorter laser pulse corresponds to higher intensities leads to higher peak temperatures and results in larger spread of ion charges due to the transient property of ionization. The larger spread of ion charges is confirmed by measuring spatially resolved spectra of the Gd LPP. For a smaller laser spot size, the lateral expansion of the plasma is stronger, resulting in faster cooling and lower conversion efficiency. The size of the BEUV emitting region is measured to be very similar to the laser spot size and the peak of the BEUV emitting plasma region is found to occur at a distance of about 50 μm from the target surface, in agreement with simulations.

Planned future work includes using the pulse synthesizer to generate Joule-level synthesized pulses and sequences composed by short pulses with a duration of ~5 ps and using the synthesized pulse and sequences to pump soft x-ray lasers.